DISSERTATION

# BUOYANCY OF CONVECTIVE VERTICAL MOTIONS IN THE INNER CORE OF INTENSE HURRICANES

Submitted by

Matthew D. Eastin

Department of Atmospheric Science

In partial fulfillment of the requirements

For the Degree of Doctor of Philosophy

Colorado State University

Fort Collins, Colorado

Summer 2003

ProQuest Information and Learning Company
300 North Zeeb Road
P.O. Box 1346
Ann Arbor, MI 48106-1346

COLORADO STATE UNIVERSITY

May 5, 2003

WE HEREBY RECOMMEND THAT THE DISSERTATION PREPARED UNDER OUR SUPERVISION BY MATTHEW D. EASTIN ENTITLED BUOYANCY OF CONVECTIVE VERTICAL MOTIONS IN THE INNER CORE OF INTENSE HURRICANES BE ACCEPTED AS FULFILLING IN PART REQUIREMENTS FOR THE DEGREE OF DOCTOR OF PHILOSOPHY.

Committee on Graduate Work

Committee Member — Wayne H. Schubert

Committee Member — Michael T. Montgomery

Committee Member — Bogusz Bienkiewicz

Committee Member — Peter G. Black

Adviser — William M. Gray

Department Head — Steven A. Rutledge

ABSTRACT OF DISSERTATION

# BUOYANCY OF CONVECTIVE VERTICAL MOTIONS IN THE INNER CORE OF INTENSE HURRICANES

The buoyancy of hurricane inner-core convective vertical motions is studied using extensive aircraft data from 175 radial legs collected in 14 intense hurricanes at four altitudes ranging from 1.5 to 5.5 km. Vertical motion events, called cores, are identified using the criteria that the convective-scale vertical velocity must exceed an absolute value of 1.0 m $s^{-1}$ for at least 0.5 km. A total of 620 updraft cores and 570 downdraft cores are included in the dataset. Core properties are summarized for the eyewall and rainband regions at each altitude.

Populations of core convective vertical velocity and diameter are approximately log-normally distributed. Roughly 70% of cores are superimposed upon mesoscale ascent. Eyewall cores are stronger and wider than rainband cores. Updraft cores in both regions exhibit a slight increase in strength and size with altitude. Downdraft cores tend to be weaker and narrower than updraft cores with less vertical variation. Over 54% of eyewall updraft cores and 63% of rainband updraft cores exhibit positive total buoyancy. Updraft cores with positive total buoyancy occupy less than 5% of the total eyewall and rainband areas, but accomplish ~40% of the total upward mass, heat, and moisture transport.

A one-dimensional updraft model is used to elucidate the relative roles played by buoyancy, water loading, vertical perturbation pressure gradient forces, and entrainment in the vertical acceleration of "typical" updraft cores. The (positive) median total buoyancy values are found to be more than adequate to explain the vertical accelerations in observed median updraft core strength, which implies that typical vertical perturbation pressure

gradient forces are directed downward and largely oppose the positive buoyancy forces. Entrainment and water-loading are also found to limit updraft magnitudes.

Three cases are examined in greater detail. In each, mid-level vertical velocity and radar reflectivity are asymmetric and exhibit a persistent relationship with the direction of the large-scale vertical wind shear. The mesoscale vertical velocities are dominated by a quasi-stationary wavenumber-one asymmetry with maximum ascent downshear left and weaker descent upshear. Mesoscale reflectivity maxima are located left of the shear, and downwind of the mesoscale ascent maxima. Over 70% of buoyant updraft cores and short-lived convective-scale reflectivity cells are located downshear. Over 60% of convective downdraft cores that transport significant mass downward are located upshear with negative buoyancy dominant in upshear-left cores and positive buoyancy dominant in upshear-right cores.

For two cases, buoyant updraft cores encountered in the mid-level eyewall exhibit equivalent potential temperatures ($\theta_e$) much higher than the $\theta_e$ observed in the low-level eyewall, but equivalent to the $\theta_e$ found in the low-level eye. Asymmetric low-wavenumber circulations appear responsible for exporting the high-$\theta_e$ eye air into the relatively low-$\theta_e$ eyewall and generating the locally buoyant updraft cores.

Implications of these results upon conceptual models of hurricane structure and evolution are discussed. Three mechanism are suggested whereby asymmetric buoyant convection could significantly contribute to hurricane evolution.

Matthew D. Eastin
Department of Atmospheric Science
Colorado State University
Fort Collins, Colorado 80523
Summer 2003

## ACKNOWLEDGEMENTS

I wish to thank my advisor Dr. William M. Gray for his tremendous support, encouragement, and guidance throughout the completion of this work. I am grateful for his efforts to send me to the NOAA Hurricane Research Division (HRD) each of the past six summers. I also wish to thank my committee members Drs. Michael Montgomery, Wayne Schubert, Peter Black, and Bogusz Bienkiewicz for many beneficial discussions and comments. In particular, I am grateful to Peter Black for providing me the opportunity to participate in the HRD Hurricane Field Program. This study would not have been possible without the dedicated efforts of the NOAA Aircraft Operations Center (AOC) and HRD over the past two decades. I am indebted to the HRD staff for providing me access to the extensive data used in this study, valuable insight concerning the data, and numerous stimulating discussions. I wish to thank Hugh Willoughby and Ed Rahn for their efforts in developing the processed radial leg database; Frank Marks and Paul Leighton for providing the along-track reflectivity profiles; Mike Black, Steve Feuer, and James Franklin for providing the GPS dropsonde data; Nancy Griffin for creating the radar animations; Neal Dorst for providing the aircraft video imagery; and Mark DeMaria for providing the SHIPS environmental predictor database. Discussions with Ed Zipser, Gary Barnes, Jim Kossin, John Knaff, Ray Zehr, Dave Nolan, Paul Reasor, John Persing have also been helpful. I am grateful to Bill Thorson, Rick Taft, Jason Conner, and Josh Pastrana for valuable computer assistance and Barbara Brumit and Amie Hedstrom for much technical assistance. Finally, I would like to thank my family and friends for their continuous love, support, and encouragement over the years. This research was funded by National Science Foundation Grants ATM-0071369 and ATM-9616818.

TABLE OF CONTENTS

LIST OF FIGURES

LIST OF TABLES

## LIST OF SYMBOLS AND ACRONYMS

| | |
|---|---|
| AOC | Aircraft Operations Center |
| $B$ | total buoyancy |
| $\overline{B}$ | core average total buoyancy |
| CAPE | Convective Available Potential Energy |
| $c_p$ | specific heat of dry air at constant pressure |
| $DB$ | dynamic buoyancy |
| $\overline{DB}$ | core average dynamic buoyancy |
| $DIAM$ | core diameter |
| $FA$ | fractional area occupied by a core |
| $g$ | acceleration due to gravity |
| GPS | Global Positioning System |
| HRD | Hurricane Research Division |
| $\kappa$ | $R_d/c_p$ |
| $L$ | radial leg length |
| $L_v$ | latent heat of vaporization |
| LF | lower fuselage C-band radar |
| $LHT$ | radial leg upward latent heat transport |
| $LHT_c$ | convective core upward latent heat transport |
| $MT$ | radial leg upward mass transport |
| $MT_c$ | convective core upward mass transport |
| M | storm motion vector |
| MPI | Maximum Potential Intensity |
| MSLP | Minimum Sea Level Pressure |

| | |
|---|---|
| N | number of cores |
| NCAR | National Center for Atmospheric Research |
| NOAA | National Oceanographic and Atmospheric Administration |
| $p$ | total pressure |
| $p^{'}$ | perturbation pressure |
| $\overline{p}$ | reference pressure |
| PMS | Particle Measuring Systems |
| $q$ | specific humidity |
| $\overline{q}$ | core average specific humidity |
| $\overline{q}_{leg}$ | radial leg average specific humidity |
| $q_c$ | cloud water content |
| $q_c^{'}$ | perturbation cloud water content |
| $q_r$ | precipitation water content |
| $q_r^{'}$ | perturbation precipitation water content |
| $q_l$ | total water content |
| $\overline{q_l}$ | core average total water content |
| $\rho$ | density of air |
| $r$ | radius in physical space |
| $r_{in}$ | radius of core's inner edge |
| $r_{out}$ | radius of core's outer edge |
| $R_{in}$ | radius of regions' inner edge |
| $R_{out}$ | radius of regions' outer edge |
| $R_d$ | gas constant for dry air |
| $RH$ | relative humidity |
| $\overline{RH}$ | core average relative humidity |
| RMW | radius of maximum wind |
| S | SHIPS 200-850 mb vertical shear vector |
| SHIPS | Statistical Hurricane Intensity Prediction Scheme |

| | |
|---|---|
| $SHT$ | radial leg upward sensible heat transport |
| $SHT_c$ | convective core upward sensible heat transport |
| SST | sea surface temperature |
| TPC | Tropical Prediction Center |
| $TB$ | thermal buoyancy |
| $\overline{TB}$ | core average thermal buoyancy |
| $\theta$ | potential temperature |
| $\overline{\theta}$ | core average potential temperature |
| $\overline{\theta}_{leg}$ | radial leg average potential temperature |
| $\theta_e$ | equivalent potential temperature |
| $\overline{\theta_e}$ | core average equivalent potential temperature |
| $\theta_v$ | virtual potential temperature |
| $\theta_v^{'}$ | perturbation virtual potential temperature |
| $\overline{\theta_v}$ | reference virtual potential temperature |
| $u$ | total radial velocity |
| $v$ | total tangential velocity |
| $VPPGF$ | vertical perturbation pressure gradient force |
| $w$ | total vertical velocity |
| $\overline{w}$ | core average total vertical velocity |
| $w_c$ | convective vertical velocity |
| $w_{c\ max}$ | core maximum convective vertical velocity |
| $\overline{w_c}$ | core average convective vertical velocity |
| $\overline{w}_{leg}$ | radial leg average total upward vertical velocity |
| $w_m$ | mesoscale vertical velocity |
| $\overline{w_m}$ | core average mesoscale vertical velocity |
| $WL$ | water loading |
| $\overline{WL}$ | core average water loading |
| $z$ | altitude in physical space |

| | |
|---|---|
| $Z$ | radar reflectivity |
| $\zeta$ | vertical component of relative voriticity |

# Chapter 1

# INTRODUCTION

An understanding of how hurricane convection behaves, organizes, and influences storm evolution is important. The inner-core convection directly provides the latent heat release and vertical transport of mass and energy required to maintain the warm core. The organization of this convection is influenced by internal dynamics as well as large-scale environmental forcings and ocean-atmosphere interactions. Any organizational change can feedback upon the local environment to influence subsequent inner-core convection and storm evolution. These processes must be better understood before significant advancements in hurricane intensity prediction can be achieved (Elsberry et al. 1992).

Great strides in understanding hurricane internal structure, dynamics, and evolution have been made since instrumented aircraft began routine penetrations. However, our understanding of inner-core cumulus convection remains limited, despite its well-recognized crucial role. Two fundamental properties used to describe the nature of cumulus convection are vertical velocity and buoyancy. Several aircraft studies have documented observed vertical velocity characteristics in hurricanes (e.g., Jorgensen et al. 1985; Black et al. 1994; Black et al. 1996). However, observational estimates of buoyancy within individual vertical motions have been limited by the inability to accurately measure temperatures within convection due to sensor wetting errors (e.g., Eastin et al. 2002a,b).

## 1.1 Background

The first attempt to quantify vertical motion and buoyancy properties of hurricane inner-core (defined here as within 150 km of storm center) convection from aircraft observations was by Gray (1965). Estimates of vertical motion with limited spatial res-

olution were attained in the lower and middle troposphere from the aircraft's Doppler navigation system. Updrafts and downdrafts were found to be weak compared to those in continental thunderstorms (Byers and Braham 1949). The vertical motions were positively correlated with local temperature perturbations; however, little confidence was given to the results due to suspected sensor wetting errors.

Jorgensen et al. (1985, hereafter JZL) used flight-level data from the National Oceanic and Atmospheric Administration (NOAA) WP-3D aircraft with improved instrumentation, navigation equipment, and data collection resolution to document vertical motions at altitudes between 0.5 and 6.1 km in the eyewalls and rainbands of four intense hurricanes. JZL studied "cores" in which the absolute vertical velocity continuously exceeded 1 m $s^{-1}$ for at least 500 m. Cores were typically weak ($< 2$ m $s^{-1}$) with small diameters ($< 2$ km). Mean vertical velocities in the strongest 10% of updraft cores exceeded only 4 m $s^{-1}$, but these few cores accounted for a substantial fraction of the mass transport. Core buoyancy was, again, not estimated due to sensor wetting errors. However, observations from a unique traverse along Hurricane Allen's (1980) eyewall suggested the presence of localized buoyant updrafts; multiple relative updraft maxima $> 10$ m $s^{-1}$ over scales of $< 5$ km were embedded within a sustained (organized) updraft in which upward vertical velocities $> 3$ m $s^{-1}$ were continuously observed over $\sim$40 km.

The radar systems on-board the NOAA WP-3D aircraft have provided much insight into the mesoscale organization of eyewalls (e.g., Jorgensen 1984a,b) and rainbands (e.g., Barnes et al. 1983), as well as their vertical velocity characteristics throughout the troposphere. Marks and Houze (1987) analyzed Doppler radial velocities along vertically incident paths across Hurricane Alicia's (1983) eyewall, and computed vertical air velocities from the difference between Doppler radial velocities and bulk precipitation fallspeeds estimated from radar reflectivities. Each radial cross-section through the eyewall depicted outward-sloping sustained updrafts over 5 km in depth. Superimposed upon the sustained updrafts were small-scale discrete "bubbles" of enhanced rising motion that were strongest above the 0°C isotherm. They argued that such eyewall structure suggested the presence

of positively buoyant updrafts. Black et al. (1996) documented Doppler derived vertical motions within the inner core of several intense hurricanes. At altitudes below 6 km, Doppler updraft and downdraft statistics were similar to those of the flight-level cores described by JZL. Above 6 km, updraft mean vertical velocity exhibited a marked increase with height which was indirectly attributed to positive buoyancy generated by condensate freezing (e.g., Lord et al. 1984).

Studies of hurricane "supercells" (Gentry et al. 1970; Black et al. 1986; Ebert and Holland 1992; Black et al. 1994; Heymsfield et al. 2001) have also implied the presence and importance of localized buoyant updrafts in hurricane evolution. Hurricane supercells are asymmetric convective events characterized by enhanced low-level convergence, absolute vertical velocities $> 10$ m $s^{-1}$, enhanced radar reflectivities, and overshooting cold cloud tops. The supercells typically occurred prior to or during hurricane intensification, implying a link to storm evolution. Buoyancy values within the intense updrafts were not computed, but appreciable positive values were assumed in most cases. For example, Black et al. (1994) used both Doppler velocities and flight-level data to document the extreme vertical motions within an eyewall supercell of Hurricane Emily (1987). They argued that moist symmetric instabilities (i.e., buoyancy forces) produced the unusually strong updrafts and downdrafts.

Several studies have provided estimates of convective available potential energy (CAPE), or the maximum potential buoyancy, in hurricanes from either databases of individual vertical soundings (e.g., Sheets 1969; Frank 1977; Bogner et al. 2002) or vertical soundings constructed from composite flight-level data at multiple altitudes (e.g., Gray and Shea 1973; Jorgensen 1984b). The consensus of these studies suggests that inner-core CAPE is small ($< 1200$ J $kg^{-1}$) and decreases towards neutral stability as one approaches the eyewall due to decreasing surface temperatures and increasing upper-level temperatures associated with the warm core. However, only minimal positive CAPE ($<$ 200 J $kg^{-1}$) would be required to explain even the strongest vertical velocities observed in hurricane supercells.

Theoretical and numerical studies have also provided insight into the organization of hurricane vertical motions and the role of buoyancy in storm evolution. Malkus and Riehl (1960) and Riehl and Malkus (1961) speculated from mass and energy budget analyses that a large fraction of the required vertical mass transport was accomplished rapidly by a few isolated buoyant updrafts, or "hot towers", rather than by a more uniform ring of gradual ascent. Ooyama (1982) theoretically argued that while sustained and organized eyewall updrafts maintain the strength of a hurricane, intensification requires buoyant updrafts that, through entrainment, can import high angular momentum air into the eyewall from above the frictional boundary layer. In contrast, Emanuel (1986) and Rotunno and Emanuel (1987) argue that the hurricane inner core is often close to a state of moist slantwise neutrality, and symmetric hurricane-like vortices can evolve with negligible contributions from buoyant updrafts. Two recent studies (Zhang et al. 2000; Braun 2002) of three-dimensional non-hydrostatic hurricane simulations have furthered the debate. Zhang et al. (2000) found the temporally and azimuthally averaged eyewall to be stable for vertical accelerations but near neutral for slantwise accelerations. They analyzed the vertical momentum budget and attributed small accelerations in the averaged vertical velocity to upward-directed perturbation pressure gradient forces. In contrast, Braun (2002) analyzed the vertical momentum budget along individual eyewall updraft trajectories, and attributed updraft accelerations to positive local buoyancy forces. The contrast between theories and between numerical simulation results raises the question of whether asymmetric buoyant convection is an integral component of inner-core structure and evolution.

Clearly, accurate observational estimates of buoyancy within hurricane inner-core vertical motions are needed. In the mid-1980s short-path radiometric thermometers were installed on the NOAA WP-3D aircraft. Lawson and Cooper (1990) have demonstrated that radiometric thermometers (which measure the radiance emitted from a small volume of air to provide an indirect temperature measurement) can provide accurate flight-level air temperatures in and near convection without the adverse effects of sensor wetting. As a

result, several studies of ordinary oceanic convection (Jorgensen and LeMone 1989; Lucas et al. 1994; Wei et al. 1998; Igau et al. 1999) have used radiometric temperatures to analyze buoyancy within convective updrafts and downdrafts. They found that ordinary oceanic updrafts (and downdrafts) were positively buoyant on average but exhibited values well below expectations from undilute ascent. Vertical velocity characteristics were nearly identical to those in hurricane rainbands (e.g., JZL), and their relative weakness, compared to those of continental thunderstorms, was attributed to buoyancy reduction through the effects of entrainment and water loading.

## 1.2 Objectives

The question of whether hurricane inner-core vertical motions are locally buoyant remains open. Therefore, a large radial leg database and the more reliable radiometric temperatures are employed to provide a statistical summary of buoyancy in inner-core convective vertical motions. Specific questions to be addressed include:

1. What are typical buoyancy values within hurricane inner-core convective updrafts and downdrafts?

2. How do buoyancy values vary as a function of altitude, radius, and azimuth?

3. What role does buoyancy, water-loading, entrainment, and vertical perturbation pressure gradient forces play in vertically accelerating typical convective updrafts?

4. Do buoyant convective updrafts significantly contribute to the total upward mass, heat, and moisture transports?

5. Do all buoyant eyewall convective updrafts originate in the boundary layer outside the eyewall, or can the low-level eye be an important source region as well?

6. Do buoyant convective updrafts play a significant role in hurricane evolution?

Chapter 2 contains a description of the data and methodology used to identify and examine the buoyancy characteristics of convective-scale vertical motions. Chapter 3 presents

summary statistics of the kinematic and buoyancy characteristics, elucidates the relative role of buoyancy in driving vertical accelerations of typical inner-core convective updrafts, and documents the fractional contribution of buoyant updrafts to the total upward mass, heat, and moisture transports. Chapter 4 examines the buoyancy characteristics of three hurricanes in greater detail in order to illustrate typical azimuthal convective organization, demonstrates that the low-level eye can be an important source region of buoyant convective updrafts observed in the eyewall, and provides evidence of three physical links between buoyant convection and storm evolution. Chapter 5 presents a summary of the primary conclusions and ideas for future work.

# Chapter 2

# DATA AND METHODOLOGY

## 2.1 Data

### 2.1.1 Flight-level data

The primary data used in this study was collected by the two National Oceanic and Atmospheric Administration (NOAA) WP-3D aircraft during 25 flights into 11 Atlantic and 3 eastern Pacific intense hurricanes from 1988 to 1998 (see Table 2.1). The basic flight-level instrumentation and radar systems on the aircraft are described in Jorgensen (1984a), and more detailed descriptions of the thermodynamic sensors used are given in Eastin et al. (2002a). The flight-level data were recorded at a 1-Hz rate during each flight and then post-processed at the NOAA Hurricane Research Division (HRD) into radial legs using methods described in Willoughby et al. (1982), Willoughby and Chelmow (1982), and Samsury and Zipser (1995). Each radial leg extends up to 150 km from the storm center and consists of storm-relative observations of the three-dimensional wind field in cylindrical coordinates, temperature, dewpoint, cloud water content, geopotential height, and the aircraft position, partitioned into 0.5 km average bins. A total of 175 radial legs at reference pressure levels of 850, 700, 600, and 500 mb were utilized. In addition, radar reflectivity from the lower-fuselage C-band and tail X-band radars were utilized.

### 2.1.2 Best-track data

Hurricane intensity and motion were determined from the best track database maintained by the Tropical Prediction Center (TPC) for both the Atlantic and eastern North Pacific basins (e.g., Neumann et al. 1999). The Atlantic basin includes the north Atlantic Ocean, Caribbean Sea and Gulf of Mexico. The term "best" refers to a combination of all

Table 2.1: Summary of flight-level data used in this study.

| Storm | Flight Date yr/mo/day | ID | Altitude (km) | Number of legs | Mean leg length (km) | Vertical Velocity Extremes[a] Max $w$ (m s$^{-1}$) | Min $w$ (m s$^{-1}$) | Number of cores[b] Up | Down |
|---|---|---|---|---|---|---|---|---|---|
| Gilbert | 88/09/11 | I | 3.0 | 8 | 90 | 9.8 | -6.5 | 32 | 22 |
| | 88/09/14 | H | 3.0 | 10 | 116 | 9.4 | -5.0 | 33 | 35 |
| | 88/09/15 | I1 | 1.5 | 8 | 132 | 2.1 | -1.4 | 10 | 4 |
| | | I2 | 1.5 | 8 | 127 | 3.4 | -2.3 | 13 | 9 |
| Joan | 88/10/21 | I | 1.5 | 6 | 102 | 6.0 | -1.6 | 17 | 11 |
| Gabrielle | 89/09/03 | H | 3.0 | 2 | 66 | 2.8 | -1.4 | 3 | 4 |
| Hugo | 89/09/15 | I | 5.5 | 4 | 95 | 5.7 | -3.3 | 6 | 7 |
| | 89/09/18 | I | 4.2 | 4 | 93 | 4.8 | -3.7 | 15 | 13 |
| | 89/09/21 | I | 4.2 | 6 | 102 | 6.0 | -3.6 | 26 | 24 |
| Gustav | 90/08/30 | I | 1.5 | 6 | 61 | 5.3 | -3.5 | 17 | 13 |
| Jimena | 91/09/23 | I | 1.5 | 2 | 87 | 9.9 | -11.2 | 4 | 5 |
| | | | 3.0 | 10 | 68 | 10.0 | -12.1 | 33 | 31 |
| | | H | 3.0 | 3 | 65 | 11.8 | -4.9 | 14 | 7 |
| | | | 4.2 | 1 | 59 | 6.9 | -1.5 | 3 | 3 |
| | 91/09/24 | I | 3.0 | 4 | 93 | 6.5 | -2.4 | 14 | 12 |
| Emily | 93/08/31 | I | 5.5 | 4 | 120 | 4.6 | -3.1 | 15 | 14 |
| Olivia | 94/09/24 | I | 4.2 | 5 | 71 | 16.0 | -3.1 | 16 | 12 |
| | 94/09/25 | I | 4.2 | 11 | 75 | 6.6 | -3.9 | 31 | 29 |
| Luis | 95/09/04 | I | 5.5 | 11 | 100 | 8.5 | -5.0 | 40 | 34 |
| | 95/09/07 | I | 4.2 | 4 | 124 | 6.6 | -2.2 | 13 | 17 |
| Opal | 95/10/04 | I | 4.2 | 4 | 126 | 5.5 | -2.7 | 19 | 14 |
| Edouard | 96/08/26 | I | 3.0 | 8 | 117 | 8.2 | -5.6 | 39 | 47 |
| | 96/08/27 | I | 3.0 | 14 | 103 | 9.8 | -5.8 | 64 | 59 |
| Fran | 96/09/05 | I | 1.5 | 4 | 113 | 1.7 | -1.7 | 6 | 10 |
| Guillermo | 97/08/02 | I | 5.5 | 12 | 105 | 12.3 | -4.6 | 49 | 50 |
| | 97/08/03 | I | 5.5 | 12 | 91 | 14.3 | -5.6 | 71 | 64 |
| Georges | 98/09/19 | H | 4.2 | 4 | 75 | 12.6 | -4.8 | 17 | 20 |
| Total | | | | 175 | | | | 620 | 570 |

[a] Determined from 0.5 km total vertical velocity ($w$) data prior to filtering.
[b] Defined from convective-scale vertical velocity ($w_c$) data after filtering. See text for definition.

reliable existing track and intensity observations during post-season analysis to determine the most accurate track and intensities for each storm. Data include the storm center position, minimum sea-level pressure (MSLP), and maximum sustained one minute wind at six hour intervals. Storm motion and intensity change during each flight (see Table 2.2) was determined by linear interpolation over the 12 hour period centered on the inner-core observation period.

### 2.1.3 Large-scale environmental data

Large-scale environmental characteristics of each hurricane were obtained from the Statistical Hurricane Intensity Prediction Scheme (SHIPS) predictor databases (DeMaria and Kaplan 1994b; 1999). The SHIPS parameters used in this study include the 200-850 mb layer vertical wind shear, sea-surface temperature (SST), and the maximum potential intensity (MPI). The vertical wind shears are derived from National Centers for Environmental Prediction (NCEP) global model analyses as the differences in the 200 and 850 mb zonal and meridional wind components averaged over the circular area within 600 km of the storm center once the storm-scale circulation is effectively removed from the model analysis using a Laplacian filter (DeMaria and Kaplan 1999). Point values of SST used by SHIPS are derived from weekly SST fields described in Reynolds and Smith (1993). The MPI estimates are determined from the SSTs following DeMaria and Kaplan (1994a) using the Kraft (1961) wind-pressure relationship. The SHIPS predictors are available at 12 hour intervals for hurricanes after 1988. Estimates of each parameter during each flight (see Table 2.2) were determined by linear interpolation over the 12 hour period centered on the inner-core observation period.

### 2.1.4 Vertical sounding data

Vertical soundings were obtained from Global Positioning Systems (GPS) dropwindsondes deployed from the aircraft. The sondes utilize the GPS satellite navigation to provide improved accuracy and resolution of altitude, winds, pressure, temperature and humidity over previous dropwindsondes. Measurements to the surface are possible with a vertical resolution of $\sim$5 m. Performance specifications, instrument design, and post-processing procedures are discussed in Hock and Franklin (1999). Post-processing and quality control was performed at HRD. GPS sondes were first deployed by the HRD in Hurricane Guillermo during the 1997 season, and over 1600 sondes have been deployed in hurricane environments since. This study utilizes 230 post-processed GPS sondes deployed within the inner-core of 8 intense hurricanes (Table 2.3). Note that concurrent flight-level

Table 2.2: Summary of hurricane intensity, motion, and large-scale environmental characteristics for all cases examined in this study.

| Storm | Flight Date yr/mo/day | Flight ID | MSLP (mb) | Intensity Change[a] (mb 12h$^{-1}$) | Storm Motion[a] (m s$^{-1}$/deg) | 200-850 mb Vertical Shear[b] (m s$^{-1}$/deg) | SST[b,c] (°C) | MPI[d] (mb) |
|---|---|---|---|---|---|---|---|---|
| Gilbert | 88/09/11 | I | 969 | -11 | 6.3 / 110 | N/A | N/A | N/A |
| | 88/09/14 | H | 891 | 18 | 6.6 / 110 | N/A | N/A | N/A |
| | 88/09/15 | I1 | 950 | 0 | 5.5 / 115 | N/A | N/A | N/A |
| | | I2 | 947 | -3 | 5.5 / 120 | N/A | N/A | N/A |
| Joan | 88/10/21 | I | 950 | -25 | 2.9 / 120 | N/A | N/A | N/A |
| Gabrielle | 89/09/03 | H | 932 | -10 | 6.3 / 90 | 3.3 / 355 | 27.7 | 932 |
| Hugo | 89/09/15 | I | 919 | -15 | 7.2 / 105 | 3.5 / 290 | 28.3 | 921 |
| | 89/09/18 | I | 958 | 9 | 4.8 / 145 | 7.8 / 240 | 28.7 | 912 |
| | 89/09/21 | I | 941 | 20 | 10.3 / 140 | 2.4 / 205 | 28.6 | 914 |
| Gustav | 90/08/30 | I | 960 | -9 | 6.1 / 190 | 7.3 / 250 | 28.3 | 921 |
| Jimena | 91/09/23 | I | 948 | -5 | 5.1 / 75 | 3.1 / 90 | 29.3 | 898 |
| | | H | 948 | -5 | 5.1 / 75 | 3.1 / 90 | 29.3 | 898 |
| | 91/09/24 | I | 950 | 5 | 5.4 / 90 | 3.8 / 45 | 28.8 | 910 |
| Emily | 93/08/31 | I | 964 | -2 | 5.3 / 190 | 3.9 / 300 | 26.9 | 943 |
| Olivia | 94/09/24 | I | 952 | -26 | 6.0 / 130 | 3.8 / 35 | 28.4 | 919 |
| | 94/09/25 | I | 930 | 17 | 4.4 / 200 | 7.5 / 260 | 26.6 | 947 |
| Luis | 95/09/04 | I | 940 | -3 | 4.6 / 95 | 4.7 / 280 | 28.5 | 917 |
| | 95/09/07 | I | 937 | -5 | 5.6 / 145 | 7.2 / 250 | 28.7 | 912 |
| Opal | 95/10/04 | I | 937 | 29 | 9.5 / 200 | 6.7 / 235 | 29.8 | 883 |
| Edouard | 96/08/26 | I | 939 | 2 | 6.2 / 115 | 5.5 / 240 | 27.5 | 935 |
| | 96/08/27 | I | 941 | -3 | 5.8 / 115 | 9.0 / 240 | 27.7 | 932 |
| Fran | 96/09/05 | I | 952 | 4 | 7.7 / 165 | 5.7 / 230 | 28.2 | 923 |
| Guillermo | 97/08/02 | I | 950 | -28 | 4.5 / 100 | 8.3 / 355 | 29.9 | 881 |
| | 97/08/03 | I | 923 | -2 | 5.5 / 95 | 5.9 / 360 | 29.9 | 881 |
| Georges | 98/09/19 | H | 939 | -10 | 7.0 / 100 | 6.6 / 310 | 28.9 | 907 |

[a] Determined from best track databases over the 12 h interval centered on the observation period.
[b] Extracted from the SHIPS predictor database (DeMaria and Kaplan 1994b, 1999).
[c] Derived from weekly sea surface temperature fields (Reynolds and Smith 1993).
[d] As defined by DeMaria and Kaplan (1994a) using Kraft (1961) relationship.

data from which vertical velocity buoyancy characteristics could be determined was only available for two of these hurricanes (Guillermo 1997 and Georges 1998).

## 2.2 Treatment of flight-level data

The vertical velocity ($w$) along each radial leg was computed using similar techniques described in JZL. These methods yield an absolute accuracy of $\pm 1$ m s$^{-1}$ for $w$ during straight and level flight. JZL noted that the zero vertical velocity was typically offset 0.1-0.4 m s$^{-1}$ in non-convective regions outside the eyewall and between rainbands due to a known drift in the vertical accelerometer, and such offsets could lead to the anomalous identification of updrafts and downdrafts. Assuming the actual vertical velocity in non-

Table 2.3: Summary of GPS dropwindsonde data used in this study.

| | Flight | | | | Number of GPS sondes | | | |
|---|---|---|---|---|---|---|---|---|
| Storm | Date yr/mo/day | ID | Altitude (km) | MSLP (mb) | Eye Region | Eyewall Region | Rainband Region | Total |
| Guillermo | 97/08/02 | I | 5.5 | 950 | - | - | 9 | 9 |
| | 97/08/03 | H | 3.0 | 923 | 1 | 6 | - | 7 |
| | | I | 5.5 | 923 | 2 | - | 5 | 7 |
| Erika | 97/09/08 | I | 2.5 | 950 | - | 9 | 6 | 15 |
| Bonnie | 98/08/23 | A | 3.0 | 955 | - | 1 | - | 1 |
| | | H | 5.5 | 955 | - | 4 | 7 | 11 |
| | | I | 4.2 | 955 | - | 1 | 4 | 5 |
| | 98/08/24 | A | 3.0 | 962 | - | - | 1 | 1 |
| | | H | 4.2 | 962 | - | 1 | 12 | 13 |
| | 98/08/26 | A | 3.0 | 963 | - | - | 2 | 2 |
| | | H | 4.2 | 963 | - | 5 | 17 | 22 |
| | | I | 2.0 | 963 | - | 2 | 8 | 10 |
| Georges | 98/09/19 | A | 3.0 | 939 | - | 1 | - | 1 |
| | | H | 4.2 | 939 | 2 | 6 | 5 | 13 |
| | | I | 4.2 | 939 | 2 | 7 | 6 | 15 |
| | 98/09/20 | A | 3.0 | 941 | - | 3 | - | 3 |
| | 98/09/21 | A | 3.0 | 965 | - | 1 | - | 1 |
| | 98/09/22 | A | 3.0 | 965 | - | 1 | 4 | 5 |
| Mitch | 98/10/25 | A | 3.0 | 950 | - | 3 | - | 3 |
| | 98/10/26 | A | 3.0 | 916 | - | 5 | - | 5 |
| | 98/10/27 | A | 3.0 | 925 | - | 5 | - | 5 |
| | | I | 3.0 | 928 | - | 20 | 3 | 23 |
| | 98/10/28 | A | 3.0 | 942 | - | 3 | - | 3 |
| Bret | 99/08/22 | A | 3.0 | 949 | - | 3 | - | 3 |
| Floyd | 99/09/12 | A | 3.0 | 955 | - | 8 | - | 8 |
| | 99/09/13 | A | 3.0 | 922 | - | 6 | - | 6 |
| | | I | 3.0 | 923 | - | 4 | 6 | 10 |
| | 99/09/14 | A | 3.0 | 929 | - | 3 | - | 3 |
| | 99/09/15 | A | 3.0 | 940 | - | 5 | - | 5 |
| Lenny | 99/11/16 | A | 3.0 | 962 | - | 4 | - | 4 |
| | 99/11/17 | A | 3.0 | 949 | - | 6 | - | 6 |
| | 99/11/18 | A | 3.0 | 952 | - | 4 | 1 | 5 |
| Total | | | | | 7 | 127 | 96 | 230 |

convective regions is close to zero, the leg average offset was determined from the $|w| < 1.5$ m s$^{-1}$ data and removed. The critical value of 1.5 m s$^{-1}$ was used to isolate non-convective regions with consideration for the absolute accuracy of the computed vertical velocities. The computed offsets were typically less than 0.3 m s$^{-1}$.

The temperature and dewpoint measurements included in the HRD radial leg database were made by Rosemount and General Eastern instruments, respectively, which are susceptible to errors induced by sensor wetting in clouds and precipitation (e.g., LeMone 1980; Lawson and Cooper 1990). During sensor wetting, the temperature ele-

ment behaves more like a wet-bulb thermometer and reports erroneously low values, while the chilled-mirror dewpoint probe measures erroneously high values. In an attempt to reduce such opposing errors the methods of Zipser et al. (1981) were employed during post-processing of the radial legs database. However, Eastin et al. (2002a,b) recently compared concurrent temperatures from a short-path radiometer to the temperatures in the radial leg database and found that the database still contained numerous cases of erroneously low temperatures on the order of 1°C that can significantly affect estimates of buoyancy.

To circumvent these errors, temperatures from the more accurate radiometer were used in combination with the General Eastern dewpoints following the procedures outlined by Eastin et al. (2002). First, a time-dependent bias in the radiometric temperatures was removed to account for a calibration drift. Then, dewpoints that exceeded the corrected radiometric temperature were set to the radiometer value with the assumption of saturation. A few potential sources of error remain. First, the radiometer measures the total radiance emitted in the 15 $\mu$m $CO_2$ spectral band, which contains contributions from both ambient air and any liquid water. The radiance emitted by water does not present a problem to air temperature measurements as long as the water drops are the same temperature. If they are not, the measured temperature will represent a weighted average of the air and water drops. The temperature of growing drops are typically less than 0.05°C warmer than the local air since supersaturations rarely exceed 1% in even the strongest updrafts (Pruppacher and Klett 1997). However, the temperature of evaporating drops approach the wet-bulb temperature of the ambient air, which can be as much as 1-2°C cooler than the air temperature depending upon ambient relative humidity. Thus, the radiometer could measure an erroneously low temperature when high liquid water contents are found in regions of large subsaturation. Eastin et al. (2002a) found that such errors are extremely rare in hurricanes. Second, wetting of the dewpoint sensor in subsaturated air introduces an error. We primarily use dewpoints to calculate virtual potential temperature ($\theta_v$), which is only a weak function of dewpoint temperature. Up-

drafts typically contain copious cloud water and are near saturation, so such errors are likely negligible. Downdrafts, however, may contain erroneously high dewpoints, which will ultimately result in anomalous positive buoyancy (Igau et al. 1999).

The resulting temperatures and dewpoints for each radial leg were then extrapolated along moist-adiabats from their reference pressure levels of 850, 700, 600, and 500 mb to reference altitudes of 1.5, 3.0, 4.2, and 5.5 km, respectively. Pressure ($p$) was then computed at the reference altitude for each radial leg assuming a moist adiabatic lapse rate between the geopotential altitude of the reference pressure level and the reference altitude. This simple procedure was done for consistency with our buoyancy definition (see Section 2.3) and should introduce no appreciable errors in the results presented.

Cloud water content ($q_c$) was measured by the Johnson-Williams "hot-wire" probe, which is designed to be sensitive to drops $< 0.06$ mm in diameter. However, numerous studies (e.g., Spyers-Duran 1968; Feind et al. 2000) have found the probe to undersample drops $> 0.03$ mm in diameter. Merceret and Schricker (1975) also found that the probe did not respond well to $q_c < 0.05$ g m$^{-3}$. As a result, $q_c$ may be underestimated by a factor as large as three depending upon drop concentrations at the large end of the cloud droplet spectrum. We will show in Chapter 3.7.2 that any such underestimations have a negligible effect upon our results due to the definition of buoyancy and reference state used (in which only relative changes are important). Baumgardner (1983) also noted the probe can suffer from out-of-cloud baseline drifting, and only upon drift removal is the absolute accuracy ($\pm$20%) attainable. Any apparent baseline drifting was manually removed after visual inspection of $q_c$ profiles.

Precipitation water content ($q_r$) was estimated from tail radar reflectivity values near the aircraft at flight level. The tail radar completes one rotation every 6 s in the vertical plane normal to the aircraft track. As a result, the radar antenna measures reflectivity along a horizontally incident path (i.e., at flight-level) every 3 s. The range gate length (75, 150, or 300 m) and range delay (0-400 m) vary from flight to flight. Thus, in order to maintain standard objective methods, a mean flight-level reflectivity ($Z$) was determined

from reflectivity values in the ~750 m equivalent range gate of the two horizontally incident pulse volumes. At typical ground speeds of ~125 m $s^{-1}$, values of $Z$ were obtained at intervals of ~0.75 km. The $Z$ values were thus linearly interpolated to the 0.5 km resolution of the radial legs. Finally, the $Z$ were converted to $q_r$ using the empirical relationships:

$$Z = \left\{ \begin{array}{ll} 14630\ {q_r}^{1.4482} & \text{for rain} \\ 670\ {q_r}^{1.79} & \text{for ice} \end{array} \right\} \tag{2.1}$$

where $Z$ is expressed in units of $mm^6\ m^{-3}$ and $q_r$ is in units of g $m^{-3}$. The relationships for rain and snow were obtained from Gamache et al. (1993) and Black (1990), respectively. These relationships were derived from data collected by Particle Measuring System (PMS) probes in hurricanes.[1] Since strong updrafts (> 5 m $s^{-1}$) can carry liquid water several kilometers above the freezing level (Black and Hallett 1986; Black et al. 1994), $q_r$ is computed as a linear combination of the rain and ice empirical formula at temperatures between 0 and -20°C. This procedure may overestimate the absolute values of $q_r$ in weak convection above the freezing-level, but relative differences (which are important here) should be unaffected. Furthermore, this procedures allows for the observed radial variation in freezing level while eliminating step-functions in $q_r$ across 0°C that are not observed (JZL; Black et al. 1996; Cecil et al. 2002) but would result if the relationships were so strictly applied.

### 2.3 Definitions of buoyancy and reference state

The definitions of buoyancy and its reference state are not unique. The key is to effectively separate the appropriate balanced state from any locally unbalanced disturbances. The conventional wisdom for isolated convection is that hydrostatic balance dominates and the reference state can be well represented by the horizontally homogeneous clear air within a few hundred kilometers of the convection. Hurricane inner-core convection, however, is superimposed upon a slowly-evolving secondary circulation and a quasi-symmetric

[1] A reflectivity based $q_r$ was used since data from the PMS 2D-P and 2D-C probes were only available for a few hurricane flights.

vortex near both hydrostatic and gradient wind balance. As a result, the appropriate balanced state for hurricane convection is not readily apparent. Zhang et al. (2000) defined the reference state locally through a running average of four adjacent model grid points (6 km resolution) on constant $\sigma$ surfaces. Braun (2002) found this definition to be inappropriate for 1.3 km grid resolution and defined the reference state on constant height surfaces as the low-wavenumber (zero and one) storm structure after Fourier decomposition.

Here, we define a *local* reference state through application of a running Bartlett filter with a 20 km window to the $\theta_v$, $p$, $q_c$, $q_r$, and $w$ data of each radial leg. The Bartlett filter (Jenkins and Watts 1968) effectively removes oscillations with wavelengths less than 20 km from the radial leg without shifting the phase of significant peaks. The motivation for this definition and its application is as follows. First, Willoughby (1979, 1990b) found through data and scale analysis that hydrostatic and gradient wind balance were good approximations for the slowly-evolving symmetric vortex on spatial scales greater than 15 km (i.e., mesoscales). Montgomery and Franklin (1998) have also shown that slowly-evolving low-wavenumber structures of the hurricane inner core satisfy the criteria for asymmetric balance (Shapiro and Montgomery 1993). Inspection of radar reflectivity fields for each hurricane (Fig. 2.1) reveals that slowly-evolving symmetric and low-wavenumber features with radial scales of $\sim$15 km are prevalent, and in some cases the low-wavenumber features propagate azimuthally. Thus, application of the filter to each radial leg of a typical figure-four pattern (e.g., Fig. 2.1) will act to capture the symmetric and low-wavenumber balanced fields without concern for the orientation of such features with respect to the figure-four pattern. Second, Shapiro and Willoughby (1982) demonstrated that persistent realistic sources (or sinks) of heat and momentum introduced to a balanced vortex will induce a slowly-evolving balanced secondary circulation on mesoscales. We thus applied the filter to the $w$ of each radial leg in order to capture the slowly-evolving mesoscale vertical motion. Third, Zhang et al. (2000) and Braun (2002) found that the symmetric and low-wavenumber components of liquid water content contribute to hydrostatic balance, and thus the filter was also applied to the $q_c$ and $q_r$ fields of each

radial leg. Clearly, our reference state definition was designed to effectively separate the slowly-evolving balanced structure on the mesoscale from the more transient convective-scale features in a manner consistent with both theory and observations.

We follow Braun (2002) and define total buoyancy ($B$) as:

$$\begin{aligned} B &= \left[g\frac{\theta_v'}{\overline{\theta_v}}\right] + \left[g(\kappa-1)\frac{p'}{\overline{p}}\right] + \left[-g(q_c' + q_r')\right] \\ &= TB + DB + WL \end{aligned} \tag{2.2}$$

where $\kappa = 0.286$, $g$ is the gravitational acceleration, overbars represent the mesoscale reference state, and primes denote convective-scale perturbations from the reference state. The three primary contributions to $B$ are referred to here as thermal buoyancy ($TB$), dynamic buoyancy ($DB$), and water-loading ($WL$). As noted by Braun (2002), the definition of total buoyancy is independent of whether air motions are purely vertical or along slantwise paths; non-zero total buoyancy will induce local accelerations in the vertical component.

Smith et al. (2003) recently advocated the inclusion of a radial component in the total buoyancy force of rapidly-rotating vortices. This radial component arises from the fact that inner-core isobaric surfaces slope into the vertical and the total force normal to the isobaric surface acting on a parcel is a combination of the gravitational, centrifugal, and Coriolis forces, or the effective gravity. However, scale analysis reveals that this radial component of buoyancy force, which is some fraction of the total centrifugal and Coriolis forces, is more than an order of magnitude smaller than any of the three vertical components ($TB$, $DB$, and $WL$) in even the most intense hurricane eyewalls. Therefore, we have neglected this radial component in our total buoyancy definition.

Shown on the lhs of Fig. 2.2 are the total and reference state $w$, $\theta_v$, $p$, $q_c$, and $q_r$ fields for a representative radial leg flown from 1843-1900 UTC 27 August 1996 in Hurricane Edouard at an altitude of 3 km along a northerly azimuth (see leg 23 in Fig. 2.1). The filtered profiles capture the mesoscale warm-core structure which is comparable to results presented in observational (Shea and Gray 1973; Barnes et al. 1983; Jorgensen 1984b; Marks et al. 1992; Gamache et al. 1993; Eastin et al. 2002b) and numerical (Ooyama

1969; Rotunno and Emanuel 1987; Liu et al. 1999; Wang 2002) studies of mesoscale inner-core structure. Shown on the rhs of Fig. 2.2 are the perturbation (convective) vertical velocity ($w_c$) and each buoyancy term in Eq. (2.1) calculated from the lhs profiles. A comparison of $w_c$ with $TB$ (or $B$) reveals that the majority of significant convective-scale updraft events (denoted by vertical lines) are locally buoyant along this radial leg. Also, note that $TB$ dominates $B$ with only small contributions from $DB$ and $WL$.

Since the focus of this study is to determine characteristics of the convective-scale vertical velocity events, and these events are defined *after* the reference state (see Section 2.4), our results may be sensitive to the reference state definition. The use of a 20 km filter window was somewhat arbitrary, but was consistent with theory and observations. Use of smaller filter windows (10-18 km) acted to decrease the number of significant convective-scale events since a larger fraction of total vertical velocity was included in the reference state. In contrast, larger filter windows (22-30 km) tended to increase the number of events, but also prevented adequate sampling of eyewall convection during some flights since events could not be defined in the first 11-15 km of each radial leg. Despite differences in numbers, no statistically significant (according to a $t$-test) systematic differences in event magnitude or buoyancy parameter distributions were noted. Braham and Kristovich (1996) also found buoyancy values to be insensitive to reference states defined over the 0.5-30 km range of equivalent window sizes. Therefore, except where noted, the results presented are effectively independent of the Bartlett filter window size used to represent the reference state.

Given that our methodology to determine the background reference state is also effectively a scale separation (e.g., Houze 1993), we will hereafter, for simplicity, refer to the background reference state as the "mesoscale" structure and perturbations from the reference state as the "convective" structure.

### 2.4 Definition of vertical velocity cores

Jorgensen et al. (1985) used the 1-Hz flight-level data with a resolution of ~125 m to define significant convective-scale vertical velocity events, called cores, for which $|w|$

exceeds 1 m $s^{-1}$ over a minimum horizontal extent of 500 m. Note that JZL defined convective cores from the *total* vertical velocity. Here, we wish to remove any slowly-evolving mesoscale vertical velocity signature prior to core identification in order to isolate the more transient convective-scale motions. Therefore, updraft and downdraft cores are defined from the *convective* vertical velocity when $|w_c|$ exceeds 1 m $s^{-1}$ for at least 0.5 km. These definitions are thus analogous to those used by JZL and are designed to separate meaningful convective events from turbulent features. The vertical lines in Fig. 2.2 denote identified updraft cores.

A total of 620 updraft cores and 570 downdraft cores were identified in the database. Several characteristics of each core are summarized. These included the maximum 0.5 km convective vertical velocity ($w_{c\ max}$) within the core; average convective vertical velocity ($\overline{w}_c$); average mesoscale vertical velocity ($\overline{w}_m$); diameter (DIAM, or radial distance along the flight leg); average thermal buoyancy ($\overline{TB}$); average dynamic buoyancy ($\overline{DB}$); average water loading ($\overline{WL}$); and average total buoyancy ($\overline{B}$). Average values were determined as the arithmetic mean of all 0.5 km values within each core. For each core, we also computed values of average relative humidity ($\overline{RH}$), average total vertical velocity ($\overline{w}$) defined as the sum of $\overline{w}_c$ and $\overline{w}_m$, average total liquid water content ($\overline{q}_l$) defined from the sum of convective and mesoscale $q_c$ and $q_r$, and average equivalent potential temperature ($\overline{\theta}_e$) using the Bolton (1980) empirical formulation.

### 2.5 Determination of eyewall and rainband regions

In order to separately determine buoyancy characteristics within eyewall and rainband convection, each radial leg was divided into two parts. Following procedures described by JZL, a cutoff radius was subjectively determined using radar imagery and radial profiles of tangential wind and $w$ to include all eyewall convection inward of this cutoff. The rainband region is located outside the cutoff radius. In general, the cutoff radius was ~15 km outside the radius of maximum wind (RMW). The eyewall was typically identified as the quasi-annular innermost ring of convection. In a few cases, the innermost convection included in the eyewall region was an asymmetric band near the RMW that spiraled

inward. If the innermost convection was composed of numerous convective bands within 15 km of one another, all the bands were included in the eyewall region. Concentric outer eyewalls described by Willoughby et al. (1982) were included in the rainband region if they were > 15 km from a distinct inner eyewall (e.g., Fig. 2.1). These procedures account for the variability of the eyewall radius as well as asymmetries from storm to storm.

## 2.6 Data representativeness

The hurricanes included in this study were required to either possess maximum sustained winds in excess of 50 m $s^{-1}$ or a minimum surface pressure below 965 mb during the flight. No further criteria were used. As a result, the sampled storms are at various stages of intensity change, are experiencing a variety of environmental forcings, and possess unique azimuthal distributions of convection. The different character of each hurricane undoubtedly contributes to variability in the statistics. During each flight, the aircraft typically flew figure-four patterns with headings at approximately right angles to the wind direction (e.g., Fig 2.1). Thus, the radial legs within a given storm are evenly distributed about the storm center, and convection is frequently sampled regardless of azimuthal variability in storm structure. Radial leg lengths were typically 100 km or more, and the eyewall region was always well sampled. During a few flights, specific experiment goals limited radial leg lengths, and thus, sampling of the rainband region. Furthermore, the majority of flights encountered relatively strong convection with 0.5 km vertical velocities in excess of 5 m $s^{-1}$ (see Table 2.1). By combining numerous radial legs from multiple storms, we believe the dataset is representative of convection in the lower and middle troposphere of intense hurricanes, and thus, is adequate for performing a statistical analysis of inner-core convective vertical motions and their buoyancy.

The majority of cores were found within mesoscale features easily identified on radar as either an eyewall or rainband. A typical figure-four pattern prevents adequate temporal sampling of a given convective band by radar to determine the particular stage in the convective life-cycle of an individual core. Thus, the data represents a random sample of growing, mature, and dissipating convection (as well as some strong mechanically

generated turbulence and gravity waves). The large data set and unique character of each storm should prevent a bias toward one particular stage.

A potential source of error could arise if the aircraft does not penetrate the core center. Assuming the cores are circular with maximum vertical velocity at the geometric center, JZL demonstrated that random penetrations of a given core would lead to an average underestimation of core $w_{c\ max}$ and $\overline{w}_c$ by a factor of two, and DIAM would be underestimated by ~20%. Extending this reasoning to $\overline{TB}$, $\overline{DB}$, $\overline{WL}$, and $\overline{B}$, and assuming that each maximizes at the geometric center, buoyancy parameters may also be underestimated by a factor of two. In a few cases, the pilots maneuvered to avoid strong reflectivity regions in the eyewall, which could also introduce a low bias in the vertical velocity and buoyancy statistics.

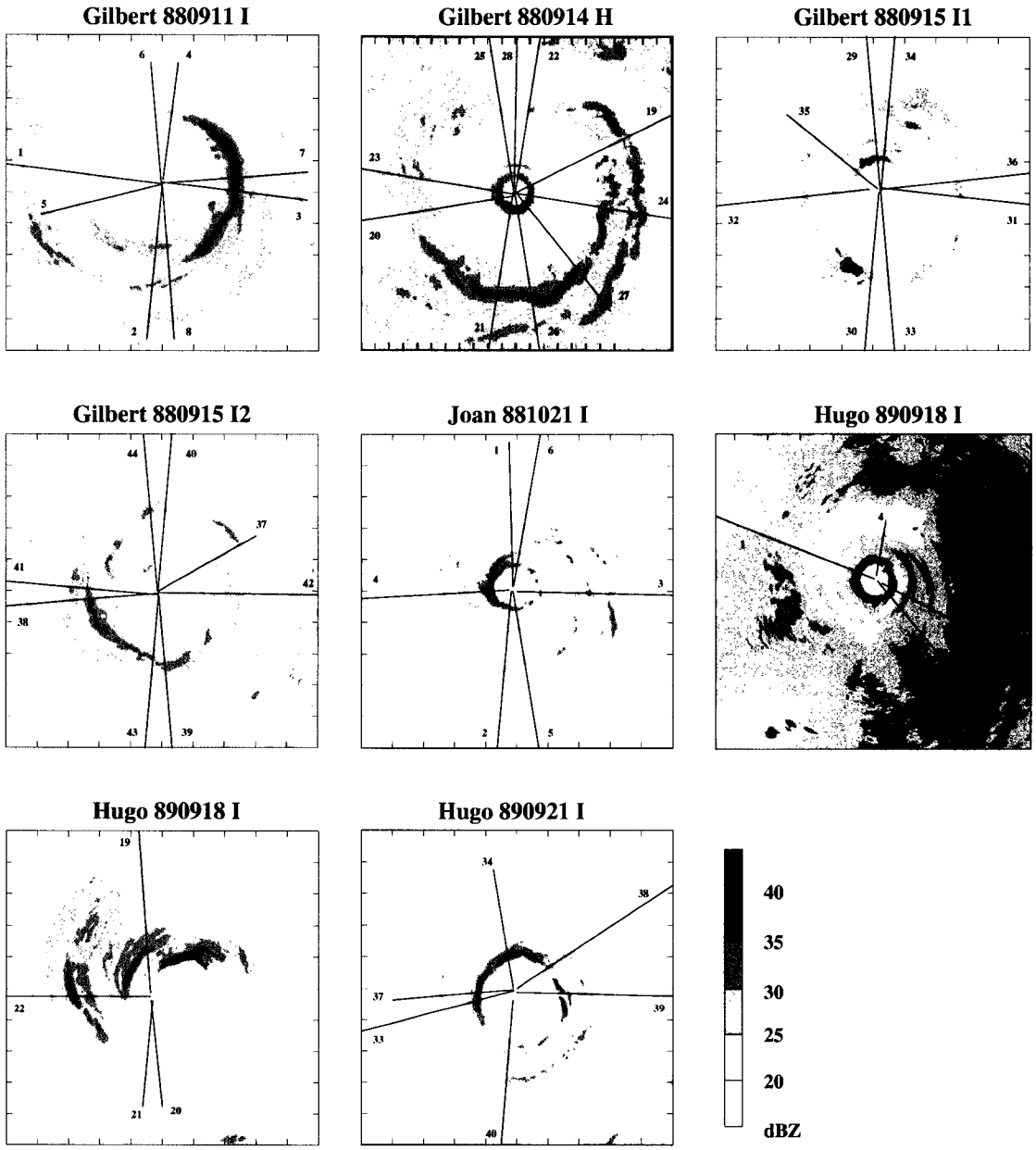


Figure 2.1: Representative lower-fuselage single-scan horizontal radar reflectivity for each hurricane flight. Note that most eyewalls are dominated by wavenumber one or wavenumber two structures of enhanced radar reflectivity. The bold lines denote the radial legs flown during each flight. Note the even azimuthal distribution of radial legs. The domain of each panel is 240 km $\times$ 240 km, tic marks are shown every 24 km, and the radar reflectivity scale is shown at the bottom.

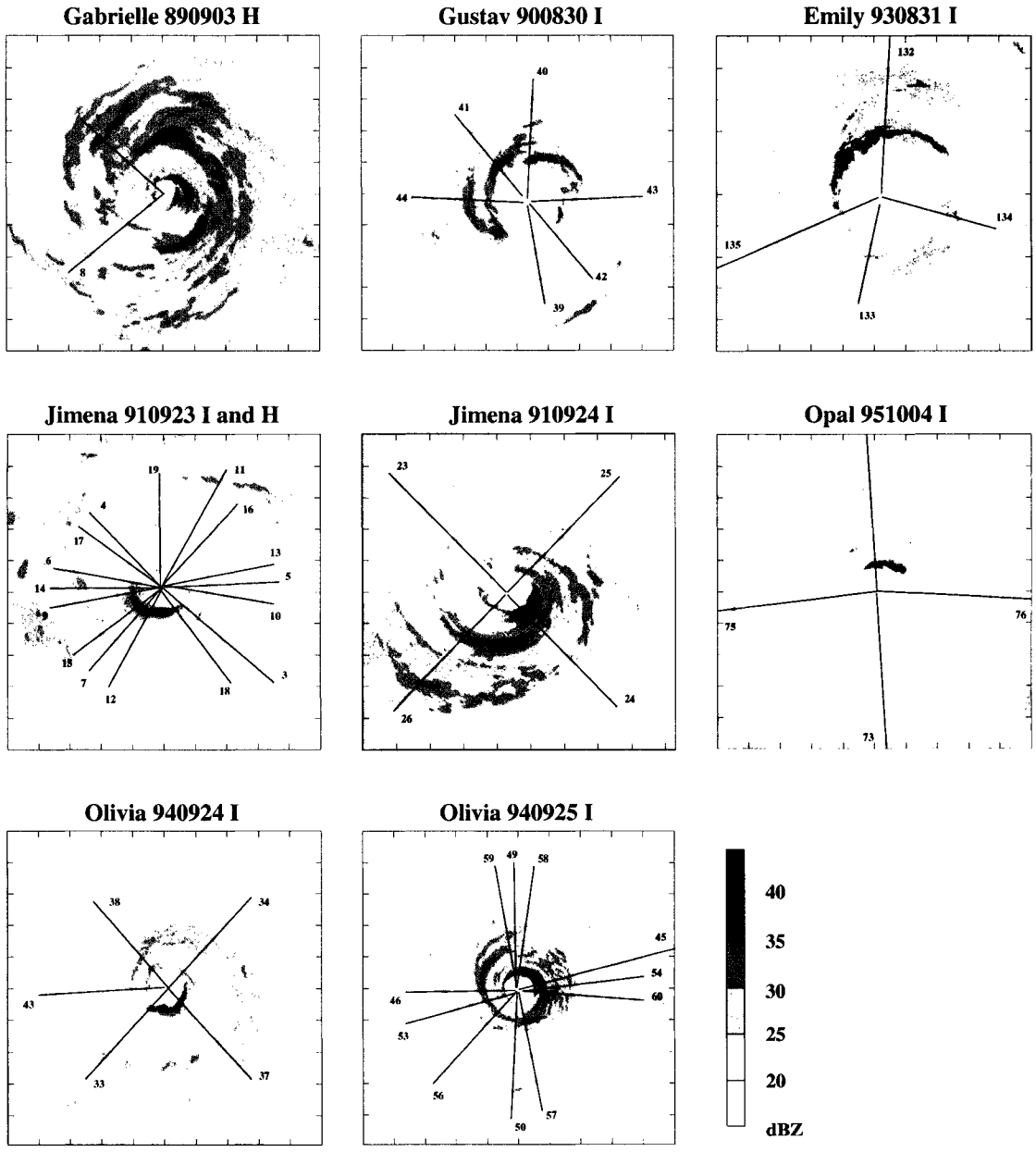


Figure 2.1: Continued.

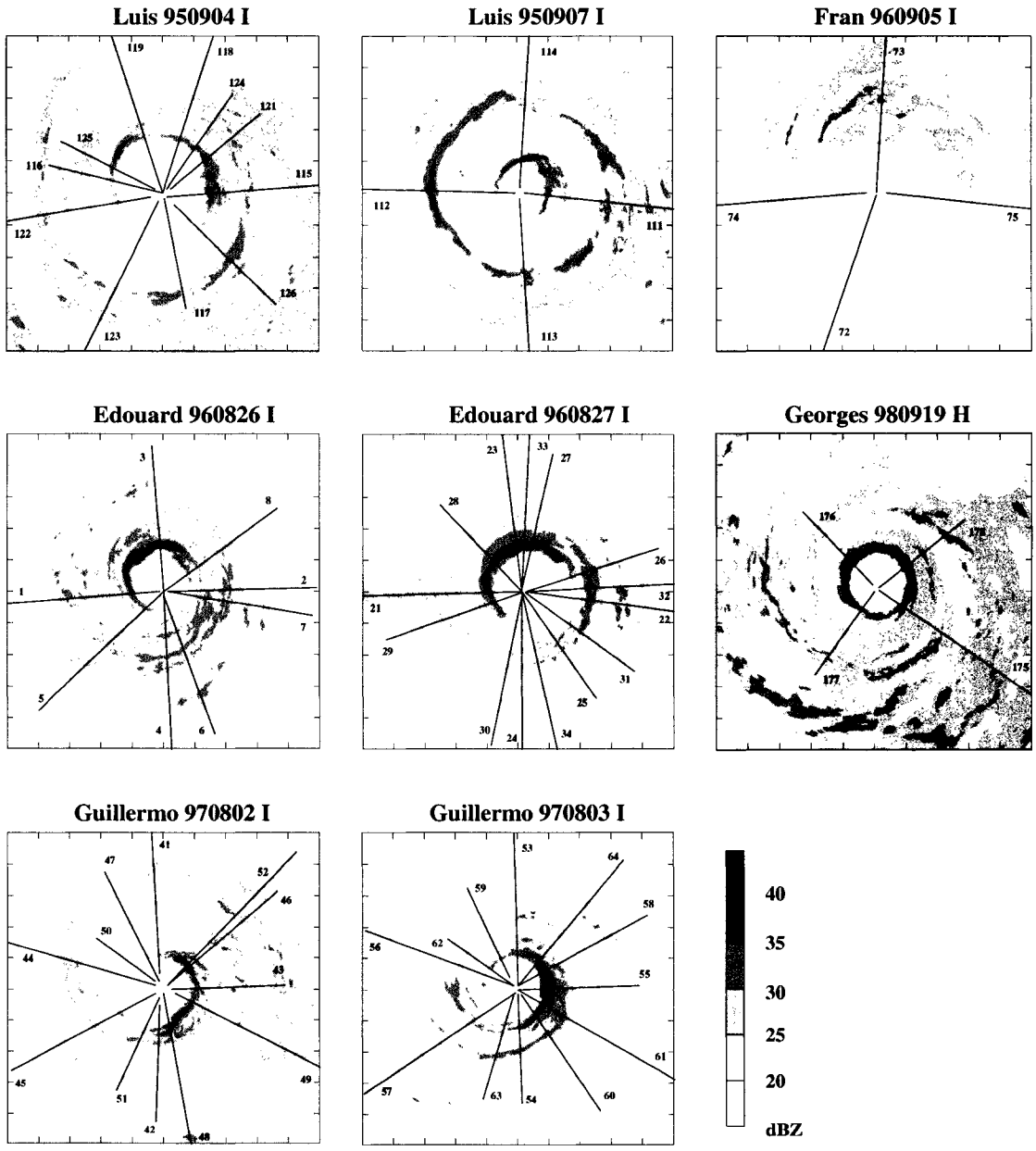


Figure 2.1: Continued.

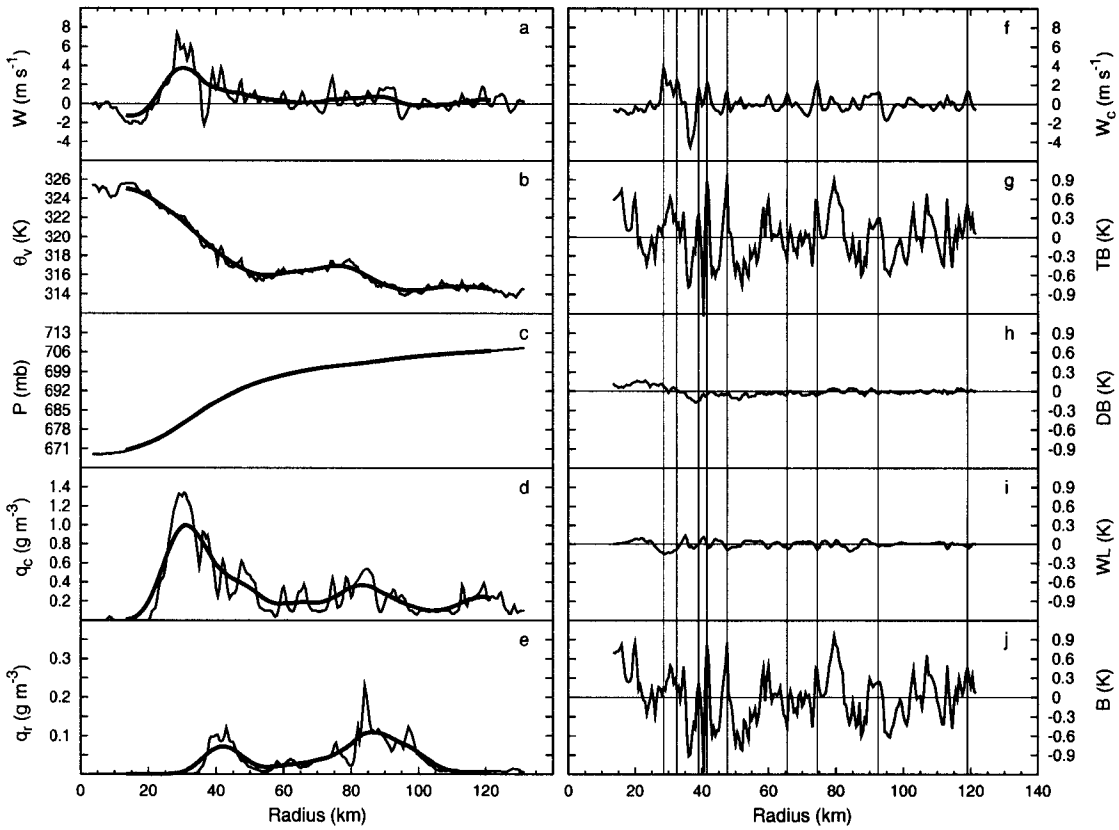


Figure 2.2: Storm-relative radial profiles of (a) total vertical velocity $w$, (b) virtual potential temperature $\theta_v$, (c) pressure $P$, (d) cloud water content $q_c$, (e) precipitation water content $q_r$, (f) convective vertical velocity $w_c$, (g) thermal buoyancy $TB$, (h) dynamic buoyancy $DB$, (i) water loading $WL$, and (j) total buoyancy $B$ for radial leg 23 in Hurricane Edouard at ~3000 m on 27 August 1996 from 1843 to 1900 UTC. Bold lines in (a)-(e) are the mesoscale profiles, or reference state, determined from application of a 20 km running Bartlett filter to the data. Vertical lines in (f)-(j) denoted identified convective updraft cores. Note that many updraft cores are positively buoyant. Further note that values of $TB$, $DB$, $WL$, and $B$ are depicted on the same scale, and that $TB$ is the dominate term in $B$. See text for definitions of $w_c$, $TB$, $DB$, $WL$, and $B$.

# Chapter 3

## STATISTICS OF CONVECTIVE VERTICAL VELOCITY CORES

### 3.1 Cumulative distributions

Distributions of DIAM, $w_{c\ max}$, $\overline{w}_c$, $\overline{w}_m$, $\overline{TB}$, $\overline{DB}$, $\overline{WL}$, and $\overline{B}$ were initially compiled for the updraft and downdraft cores of each flight and each altitude. All $w_{c\ max}$, $\overline{w}_c$, and DIAM distributions were approximately log-normally distributed with many more weak and small cores than strong or large cores. All $\overline{w}_m$, $\overline{TB}$, $\overline{DB}$, $\overline{WL}$, and $\overline{B}$ distributions were approximately normally distributed. As a result of the similarities, the distributions from each flight and altitude were combined and are presented in Figs. 3.1 and 3.2 for updraft and downdraft cores within the hurricane inner core. Section 3.2 discusses altitude variations.

Cumulative distributions of core diameter (Fig. 3.1a) and magnitude (Figs. 3.1b-c) are approximately linear on log-normal plots. Updraft and downdraft DIAM distributions were nearly identical with median (50%) values of ~1.5 km. Median $\overline{w}_c$ of updrafts and downdrafts were also similar with a values of 1.5 m $s^{-1}$ and $-1.4$ m $s^{-1}$, respectively. However, for extreme events, updraft cores tended to be stronger than downdraft cores. Values of $w_{c\ max}$ were ~30% larger than corresponding $\overline{w}_c$ values. The distributions clearly contain few large or strong cores. Less than 5% of cores encountered were > 5 km in diameter or exceeded $\pm 5$ m $s^{-1}$ in average magnitude. The overall weakness of the convective cores is noteworthy. The strongest $w_{c\ max}$ found in the dataset were 11.8 m $s^{-1}$ at 4.2 km altitude in the eyewall of Olivia and $-10.8$ m $s^{-1}$ at 3.0 km altitude in the eyewall of Jimena. If the mesoscale vertical motion is included, maximum and minimum 0.5 km vertical motions rarely exceed $\pm 10$ m $s^{-1}$ during a given flight (see Table 2.1). The strongest 0.5 km total updraft found within the database is 16.0 m $s^{-1}$ in the eyewall of

Olivia. This value is comparable to the strongest updraft observed by JZL (17.2 m $s^{-1}$) and Black et al. (1994; 23.9 m $s^{-1}$) at similar altitudes in other intense hurricanes.

Also shown in Figs. 3.1a-c are the analogous JZL cumulative distributions of updraft and downdraft core diameter and magnitude estimated from *total* vertical velocity data within four intense hurricanes. The differences are largely attributable to differences in data resolution and removal of the mesoscale vertical velocity from the total prior to convective core identification.[1] Of interest here are the distribution shapes and gross magnitudes. In particular, JZL also found that distributions of core diameter and magnitude were approximately log-normal, diameters rarely exceeded 5 km, and magnitudes rarely exceeded $\pm 5$ m $s^{-1}$. The similarities provide strong evidence that the data used here and the data used by JZL are representative of similar populations. Such properties were also found by Black et al. (1996) using Doppler radar velocity data from several intense hurricanes. The log-normal character of core strength and diameter cumulative distributions is also consistent with the character of radar echo area, height, and duration distributions for hurricane convection (Parrish et al. 1984) and ordinary tropical convection (Lopez 1977).

The cumulative distributions of core average mesoscale vertical velocity (Fig. 3.1d) are approximately linear on linear-normal plots. Median $\overline{w}_m$ for updrafts and downdraft cores were 0.6 m $s^{-1}$ and 0.4 m $s^{-1}$, respectively, or ~40% of the median $\overline{w}_c$ magnitudes. The majority of $\overline{w}_m$ range from $-1$ m $s^{-1}$ to 3 m $s^{-1}$. The maximum and minimum $\overline{w}_m$ found in the database were 6.5 m $s^{-1}$ at 5.5 km altitude in the eyewall of Guillermo and $-3.5$ m $s^{-1}$ at 4.2 km altitude in the eyewall of Opal, respectively. These magnitudes are consistent with observational (Gray and Shea 1973; Barnes et al. 1983; Jorgensen 1984b; Marks et al. 1992) and numerical (Rotunno and Emanuel 1987; Liu et al. 1999; Wang 2002) studies of mesoscale inner-core structure. More importantly, they show that some

[1]When cores are defined from the total vertical velocity (as in JZL) and the net effects of data resolution are accounted for in the statistics following the LeMone et al. (1994) guidelines, the overall magnitudes were very similar.

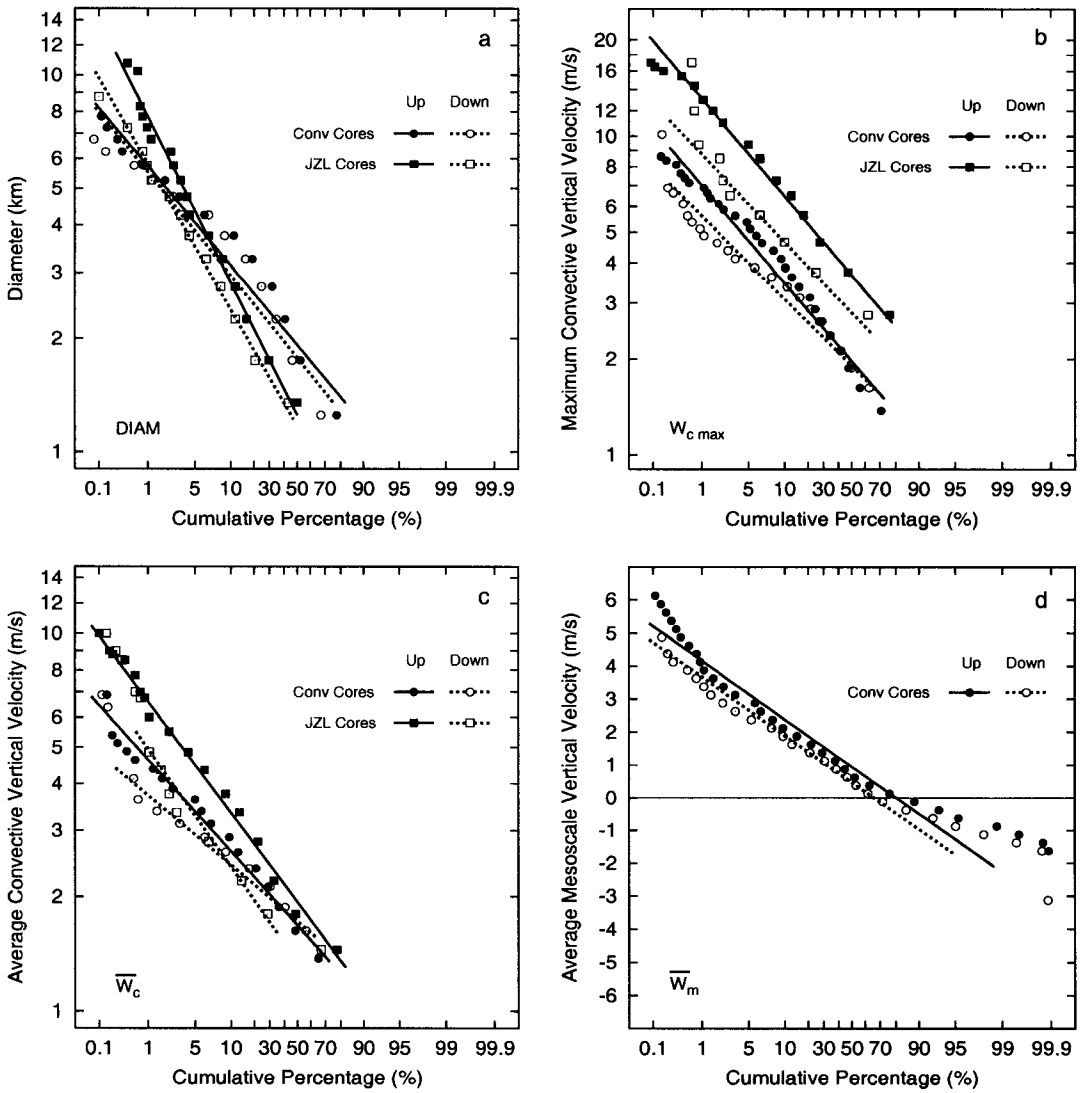


Figure 3.1: Cumulative distributions of core (a) diameter DIAM, (b) maximum convective vertical velocity $w_{c\ max}$, (c) average convective vertical velocity $\overline{w}_c$, and (d) average mesoscale vertical velocity $\overline{w}_m$ for all updrafts and downdrafts. The analogous Jorgensen et al. (1985) core data from their Fig. 1 is also shown. The straight lines represent subjectively determined linear fits to the data.

intense hurricane eyewalls are not quasi-symmetric rings of ascent, but rather have regions of organized mesoscale descent. Also, note that ~60% (~30%) of convective downdrafts (updrafts) were superimposed upon mesoscale ascent (descent). Implications upon core buoyancy regarding this latter point are discussed in Section 3.3.

The cumulative distributions of core average buoyancy (Figs. 3.2a-d) are also approximately linear on linear-normal plots. Magnitudes of $\overline{TB}$, $\overline{DB}$, $\overline{WL}$, and $\overline{B}$ have been adjusted to the common unit of Kelvin for easier comparison with other studies. Updraft and downdraft core $\overline{TB}$ ranged from roughly 1.9 K to $-1.7$ K with median values of 0.21 K and $-0.06$ K, respectively. Values of $\overline{DB}$ and $\overline{WL}$ are much smaller, ranging primarily over $\pm 0.5$ K with absolute median values less than $\pm 0.05$ K for both updrafts and downdrafts. Note that ~30% of updrafts and ~55% of downdrafts have positive $\overline{WL}$ contributions that act to accelerate cores *upward.* Such small and positive contributions arise from defining a *local* reference state in which mesoscale liquid water contents contribute to hydrostatic balance. Updraft and downdraft core $\overline{B}$ distributions were very similar to the $\overline{TB}$ distributions with median values of 0.16 K and $-0.05$ K, respectively. Means of each distribution are nearly identical to the median values.

Recent studies have provided $\overline{TB}$ statistics for convective vertical motions in ordinary oceanic tropical convection (Jorgensen and LeMone 1989; Lucas et al. 1994; Wei et al. 1998) and hurricane rainbands (Eastin et al. 2002). For updraft cores, these studies reported positive median (and mean) $\overline{TB}$ values of ~0.5 K in ordinary tropical convection and ~0.15 K in hurricane rainbands. Despite slightly different core and reference state definitions, our updraft median $\overline{TB}$ (which also include eyewall cores) is in agreement with Eastin et al. (2002), and is consistent with the other studies given that the background CAPE within the hurricane inner core is significantly less that in the general tropics (Sheets 1969; Frank 1977; Bogner et al. 2000). For downdraft cores, the aforementioned studies found *positive* median (and mean) $\overline{TB}$ values on the order of ~0.1-0.2 K. Evidence will be presented in section 3.3 that suggests the negative median $\overline{TB}$ found here is related to the core definition used.

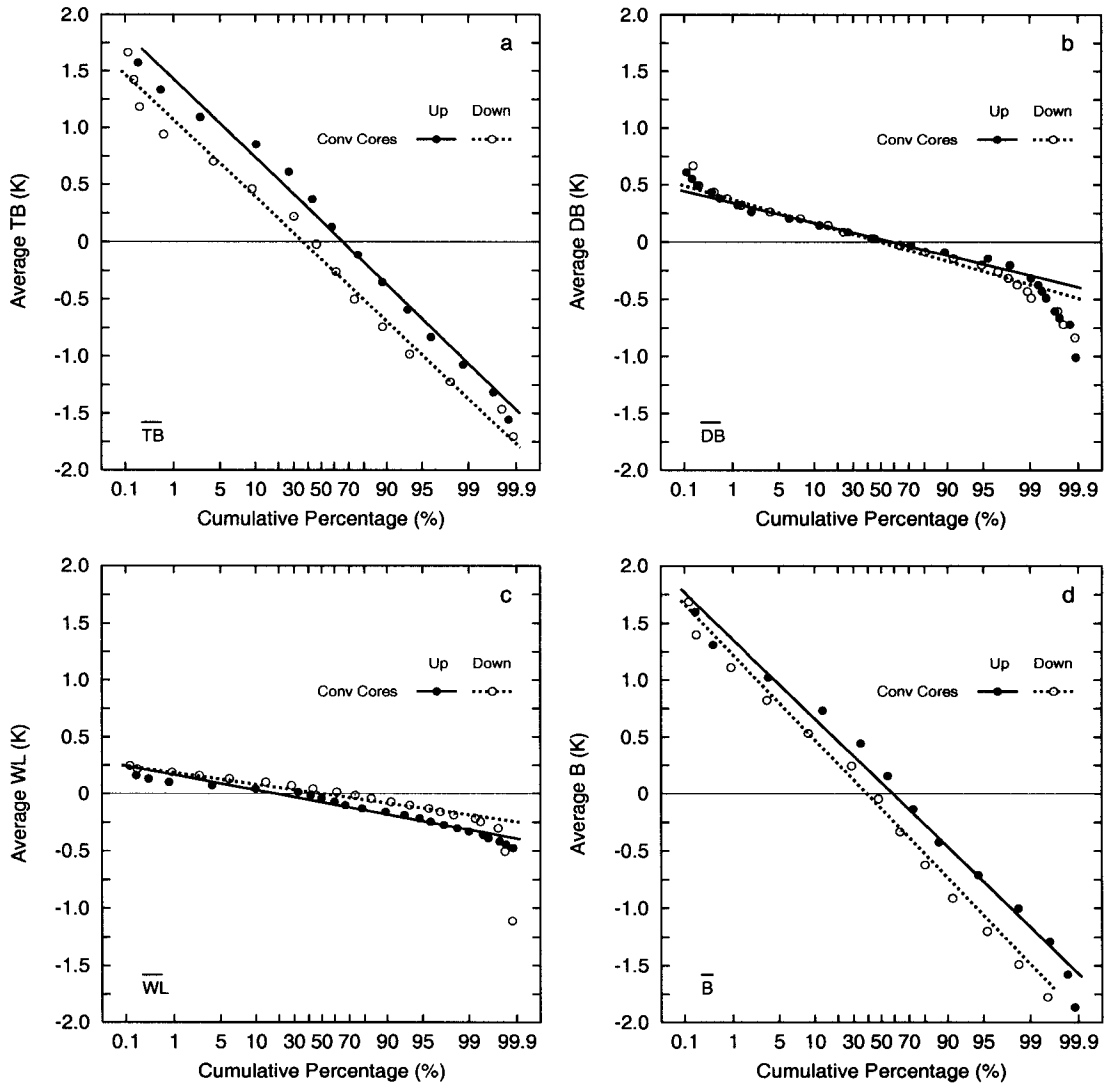


Figure 3.2: Cumulative distributions of core (a) average thermal buoyancy $\overline{TB}$, (b) average dynamic buoyancy $\overline{DB}$, (c) average water loading $\overline{WL}$, and (d) average total buoyancy $\overline{B}$ for all updrafts and downdrafts. The straight lines represent subjectively determined linear fits to the data.

### 3.2 Stratification by eyewall and rainband region

Differences between eyewall and rainband cores are elucidated by extracting the median (50% of the population) and extreme 10% (> 90% and < 10% of the population) values from their respective distributions at each altitude level. The resulting vertical profiles are shown in Figs. 3.3 and 3.4. Note that the lower 10% statistics for DIAM, $w_{c\ max}$, and $\overline{w}_c$ are not displayed since the values were equivalent to the core definition criteria.

The diameters and magnitudes (Figs. 3.3a-f) of both updraft and downdraft cores tended to increase slightly with altitude in both regions. The increases were more pronounced in the eyewall region. Here, the largest core diameters (upper 10%) increased from ~2.5 km at 1.5 km altitude to ~4 km at 5.5 km altitude, while median core DIAM increased ~1 km through the same depth. The strongest eyewall updraft cores increased by ~1.5 m $s^{-1}$ in $\overline{w}_c$ and by ~3 m $s^{-1}$ in $w_{c\ max}$ from 1.5 to 5.5 km. Median eyewall updrafts exhibited a 0.8 and 0.4 m $s^{-1}$ increase in $w_{c\ max}$ and $\overline{w}_c$, respectively, from 1.5 to 4.2 km. Eyewall downdraft cores were ~25% weaker than updraft cores with less consistent increases by altitude. For rainband cores, the DIAM, $w_{c\ max}$, and $\overline{w}_c$ statistics exhibited less increase with altitude than their eyewall counterparts and were ~25% smaller and weaker. Overall, the increases with altitude reflect a tendency for mid-level cores to be larger and stronger entities compared to low-level cores.

JZL presented analogous vertical profiles of core diameter and magnitude upper 10% distrbution levels for each region (see their Figs. 2-5). Despite differences in magnitude primarily related to differences in data resolution and core definition, the gross variations with altitude are in qualitative agreement. In particular, JZL noted that the largest and strongest updraft cores found in both eyewalls and rainbands increased slightly in magnitude and diameter with altitude, while downdrafts cores displayed less consistent altitude variations. Such properties were also noted by Black et al. (1996). In fact, consistent results from similar studies of ordinary convection (LeMone and Zipser 1980;

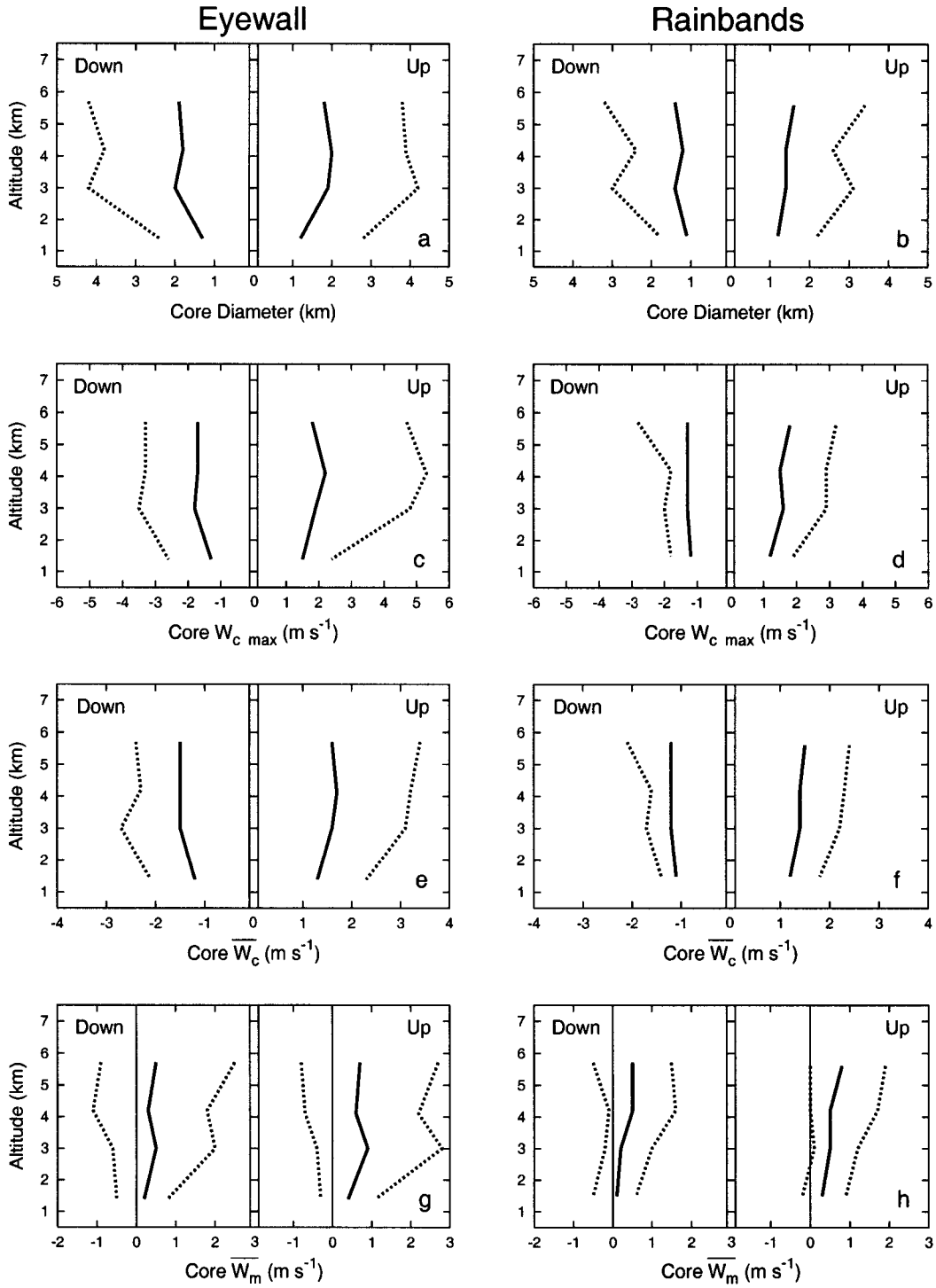


Figure 3.3: Variation with altitude of the median (solid) and extreme 10% (dashed) values of core (a)-(b) diameter, (c)-(d) maximum convective vertical velocity, (e)-(f) average convective vertical velocity, and (g)-(h) average mesoscale vertical velocity for updrafts and downdrafts in the eyewall and rainband regions. The four left-hand (right-hand) panels are for the eyewall (rainband) region. The lhs (rhs) of each panel presents the statistics of downdraft (updraft) cores.

Jorgensen and LeMone 1989; Lucas et al. 1994; Wei et al. 1998; Igau et al. 1999) indicate that these general altitude variations are common to all tropical oceanic convection.

The mesoscale vertical motion (Figs. 3.3g-h), upon which the convective cores are superimposed, also tended to increase slightly in magnitude with altitude in each region. Median $\overline{w}_m$ increased ~0.3 m s$^{-1}$ from 1.5 to 5.5 km, and were positive at all levels. The increase was more evident in the upper 10% profiles of both regions as positive $\overline{w}_m$ increased more than 1 m s$^{-1}$ over the same depth. Rainband $\overline{w}_m$ were ~25% weaker than their respective eyewall values. Of particular note are the lower 10% profiles of each region. In the eyewall, the decrease in $\overline{w}_m$ with altitude (or increase in absolute magnitude) indicates that organized mesoscale downdrafts were more frequent and stronger at mid-levels than at low-levels. For rainbands, the near zero $\overline{w}_m$ suggests that appreciable mesoscale downdrafts ($\overline{w}_m < -0.5$ m s$^{-1}$) were rare outside the eyewall. Overall, such results are consistent with the above-mentioned observational and numerical studies of mesoscale inner-core structure.

Figure 3.4 shows the median and extreme 10% vertical profiles of $\overline{TB}$, $\overline{DB}$, $\overline{WL}$, and $\overline{B}$ for updraft and downdraft cores in eyewalls and rainbands. The majority of altitude and region variability in $\overline{B}$ (Figs. 3.4g-h) was captured by the $\overline{TB}$ (Figs. 3.4a-b) profiles. Both median and extreme values of $\overline{DB}$ and $\overline{WL}$ (Figs. 3.4c-f) were comparatively small and nearly constant with height. Furthermore, altitude variations in the extreme 10% profiles of $\overline{B}$ are fairly similar to those in the respective median profiles, indicating that changes in distribution "shape" with altitude are minimal compared to changes in the median (or mean) values. As a result, only the median $\overline{B}$ profiles are discussed.

For updraft cores, the median $\overline{B}$ in the eyewall were slightly positive (~0.1 K) below 3.0 km and near neutral (~0.0 K) above 3.0 km. In rainbands, the median $\overline{B}$ were positive at all altitudes, increasing with altitude to ~0.25 K at 3.0 and 4.2 km, and then decreasing above. The larger $\overline{B}$ values in rainband cores reflects a reduction of background CAPE upon approach to the eyewall (e.g., Bogner et al. 2000). The decrease in $\overline{B}$ above 3 km suggests that entrainment played a significant role in reducing updraft core buoyancy, in

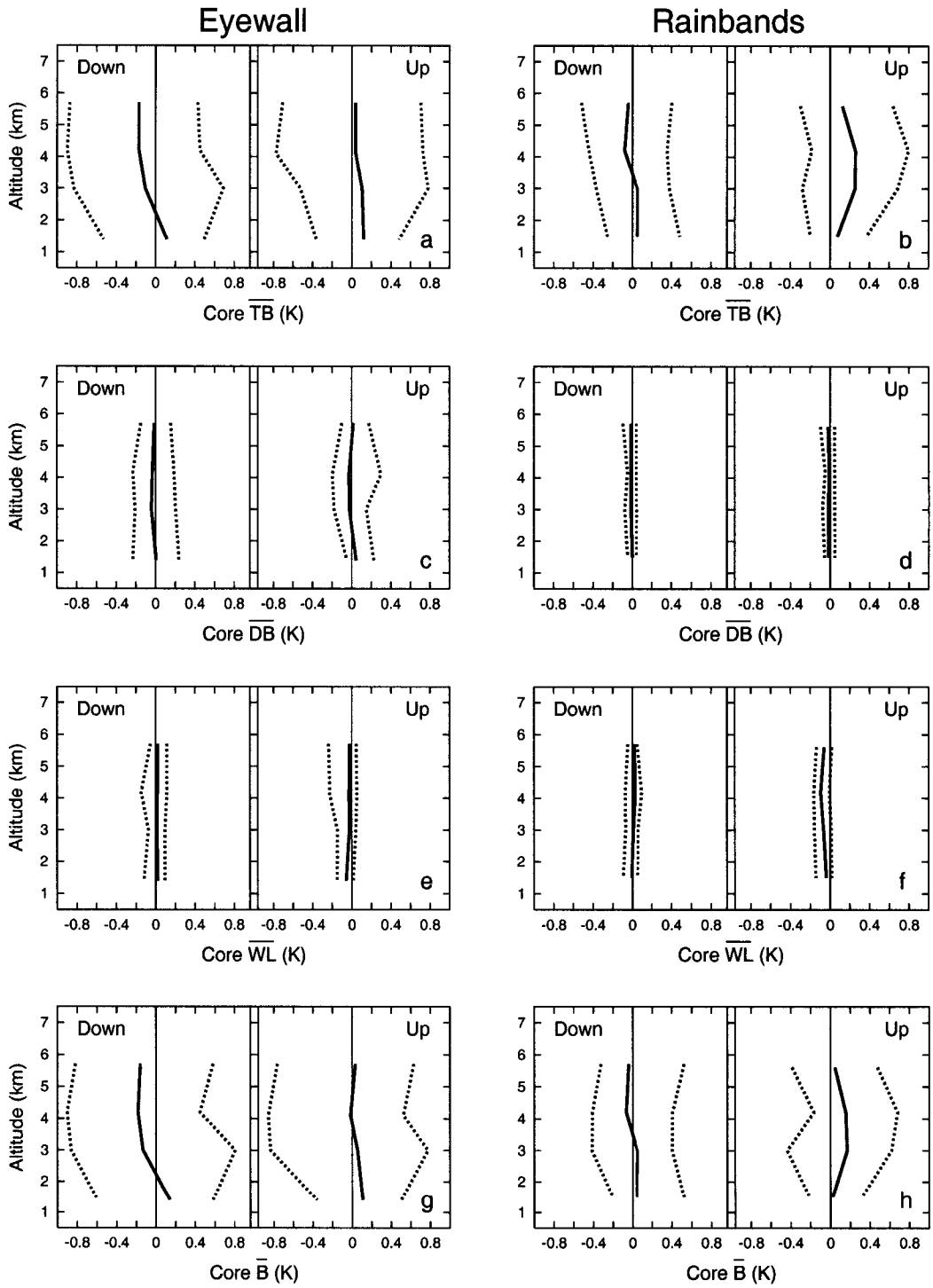


Figure 3.4: As in Fig. 3.3 but for core (a)-(b) average thermal buoyancy, (c)-(d) average dynamic buoyancy, (e)-(f) average water loading, and (g)-(h) average total buoyancy.

agreement with studies of convection outside hurricanes (Jorgensen and LeMone 1989; Lucas et al. 1994; Wei et al 1998). More importantly, the positive $\overline{B}$ should generate vertical accelerations in updraft magnitude, which is consistent with the updraft core median $\overline{w}_c$ profiles (Figs. 3.3e-f). In fact, we shall demonstrate in Section 3.7.2 that such positive median $\overline{B}$, despite being small, are statistically significant and entirely adequate to explain the observed increases in $\overline{w}_c$ with altitude for both regions.

For downdraft cores, the median $\overline{B}$ in the eyewall were slightly negative (−0.2 K) above 3.0 km, but positive (0.2 K) at 1.5 km. Median $\overline{B}$ in rainbands exhibited a similar vertical structure but with ~50% smaller magnitudes. Thus, the profiles suggest that mid-level downdraft cores should accelerate downward while low-levels downdrafts should decelerate, which is qualitatively inconsistent with the median $\overline{w}_c$ profiles (Figs. 3.3e-f). As noted earlier, previous estimates of median (or mean) $\overline{TB}$ for downdrafts cores in ordinary oceanic tropical convection were slightly positive at all levels below 6 km. Such discrepancies are discussed next in Section 3.3.

### 3.3 Additional stratifications

Two additional stratifications are presented. The first was motivated by the possibility that an updraft (downdraft) core was superimposed upon mesoscale descent (ascent) of greater magnitude than the core. Such cores will experience heating/cooling processes opposite to those experienced by their counterparts, which may influence the buoyancy statistics. To elucidate any differences, updraft and downdraft cores were stratified by their average *total* vertical velocity. Updraft cores were split into two groups; cores that accomplished significant upward transport ($\overline{w} > 1$ m s$^{-1}$), and cores that did not ($\overline{w} < 1$ m s$^{-1}$). Downdraft cores were split analogously.

Over 92% of updraft cores (571 of 620) exhibited $\overline{w} > 1$ m s$^{-1}$, and re-computed statistics for these cores (not shown) were nearly identical to those presented in Figs. 3.1-3.4. Downdraft cores, however, were found to be evenly distributed between cores with $\overline{w} < -1$ m s$^{-1}$ (273 of 570, or 48%) and cores with $\overline{w} > -1$ m s$^{-1}$. Statistics were re-computed for both subsets, and significant differences in $\overline{TB}$ and $\overline{B}$ were found (Fig. 3.5a). Median $\overline{B}$

in downdraft cores with $\overline{w} < -1$ m s$^{-1}$ were slightly positive at all levels in agreement with studies of ordinary tropical convection (Jorgensen and LeMone 1989; Lucas et al. 1994; Wei et al. 1998). The positive $\overline{B}$ values reflects a tendency for dry-adiabatic warming to dominate any evaporational cooling or water loading, which will lead to a deceleration of the downdraft. In contrast, downdraft cores with $\overline{w} > -1$ m s$^{-1}$ exhibit negative median $\overline{B}$ at all levels, which would accelerate the downdrafts, in most cases against the opposing mesoscale updraft. Such differences suggest that many hurricane convective downdraft cores may originate as localized regions of negative buoyancy that begin to accelerate against the mesoscale updraft. Upon overcoming the mesoscale updraft, the downdraft cores can continue to accelerate until adiabatic warming dominates evaporational cooling and water-loading (i.e., positive buoyancy is attained), leading to a deceleration and demise of the downdraft.

The second stratification was motivated by the results from the first and the lack of relative humidity and liquid water criteria in the core definition. In particular, are the buoyancy statistics for saturated cores with appreciable liquid water different from subsaturated cores without liquid water? To elucidate any such differences, we separated "moist" cores ($\overline{RH} > 95\%$ and $\overline{q}_l > 0.05$ g m$^{-3}$) from "dry" cores (either $\overline{RH} < 95\%$ or $\overline{q}_l < 0.05$ g m$^{-3}$). The threshold values were chosen to account for instrumental random error. We further limited the stratification to cores with $|\overline{w}| > 1$ m s$^{-1}$ in order to eliminate the heating considerations addressed above.

Roughly 80% (456 of 571) of updraft cores that accomplished significant upward transport were moist. Re-computed statistics for each subset (not shown) revealed no statistically significant differences despite moist updrafts having slightly higher $\overline{w}_c$ and slightly lower $B$ due to larger (more negative) $WL$ values. Therefore, the presence of "dry" convection in the core distribution introduced no bias in the updraft statistics.

In contrast, only ~35% (98 of 273) of downdraft cores that accomplished significant downward transport were moist. Re-computed statistics for each subset revealed statistically significant differences in $\overline{TB}$, $\overline{WL}$, and $\overline{B}$. Figure 3.5b shows the median $\overline{B}$ profiles

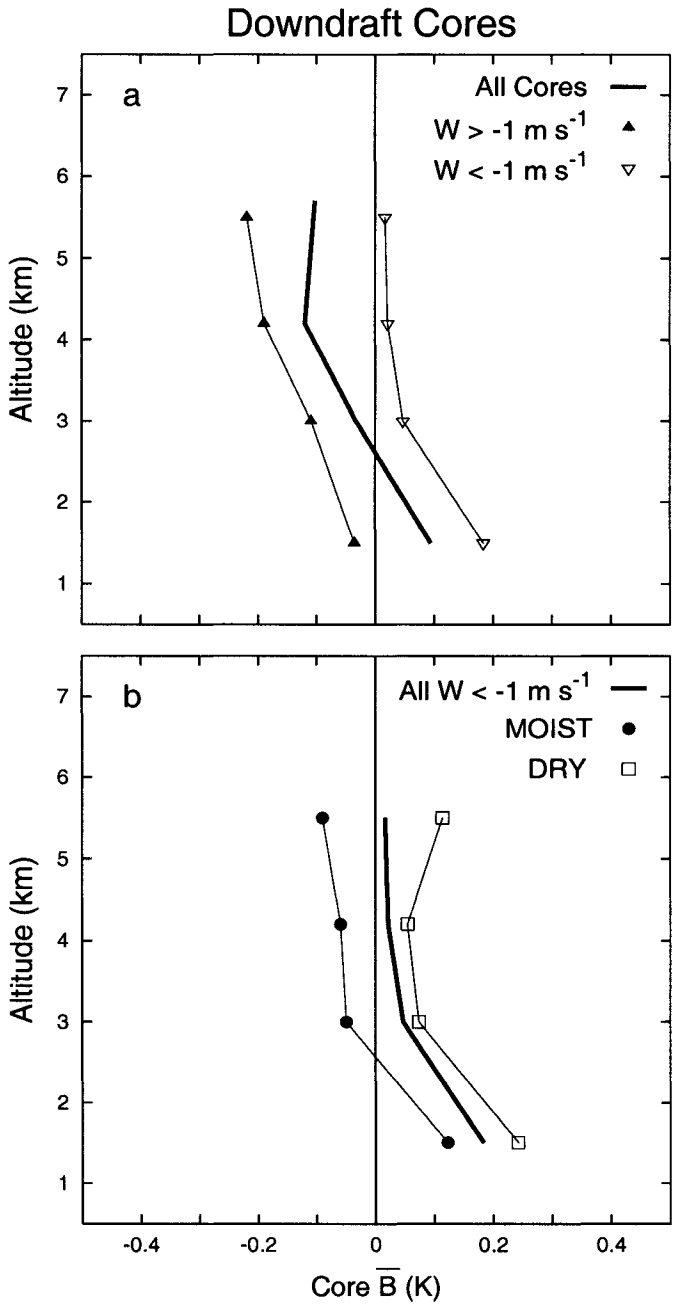


Figure 3.5: Variation with altitude of median average total buoyancy for (a) all downdraft cores (solid), the subset of downdraft cores with an average total vertical velocity $\overline{w} < -1$ m s$^{-1}$ (open triangles), and the subset of downdraft cores with $\overline{w} > -1$ m s$^{-1}$ (closed triangles); and (b) all downdraft cores with $\overline{w} < -1$ m s$^{-1}$ (solid) and the further subsets of moist (closed circles) and dry (open squares) downdraft cores. Moist cores are defined as having an average relative humidity > 95% and total liquid water content > 0.05 g m$^{-3}$. Dry cores do not satisfy both criteria.

for each subset. Moist (dry) downdraft cores tended to exhibit negative (positive) $\overline{B}$ at mid-levels. Roughly 80% of the difference was related $\overline{TB}$ differences, implying that the negative $\overline{B}$ in moist downdraft cores were likely maintained by enhanced evaporative cooling. Srivastava (1987), however, demonstrated that negative $\overline{TB}$ can only be maintained over substantial depths (> 1 km) if $\overline{q}_l$ exceeds ~4 g m$^{-3}$ or the local lapse rate is nearly dry-adiabatic. Since $\overline{q}_l$ rarely exceeds 3 g m$^{-3}$ in hurricanes (Ackerman 1963; Black and Hallett 1986) and inner-core lapse rates are nearly moist-adiabatic (Sheets 1969, Frank 1977), the negative $\overline{TB}$ (and $\overline{B}$) are likely short-lived. Thus, adiabatic warming will quickly dominate evaporational cooling and the downdrafts will become subsaturated (i.e., dry downdrafts) and positively buoyant. As a result, downward accelerations are minimized along with core magnitudes. The relatively few number of moist downdrafts and the overall weak downdraft magnitudes support this assertion.

### 3.4 Correlations between distributions

Parcel theory predicts that buoyant convection will have a positive correlation between $\overline{w}_c$ and $\overline{TB}$. Figure 3.6 shows scatterplots of $\overline{w}_c$ with respect to $\overline{TB}$ for the updraft cores of each region. In rainbands (Fig. 3.6c), a positive correlation is readily apparent and further illustrated when averages of $\overline{TB}$ are taken over $\overline{w}_c$ intervals (Fig. 3.6d); a $\overline{TB}$ of ~0.4 K is representative for the stronger $\overline{w}_c > 2$ m s$^{-1}$ updraft cores. In the eyewall (Fig. 3.6a), a weak positive correlation is only apparent upon averaging $\overline{TB}$ over $\overline{w}_c$ intervals (Fig. 3.6b); a $\overline{TB}$ of ~0.2 K is representative for the stronger eyewall updraft cores. Figure 3.7 shows similar scatterplots for the downdraft cores of each region. No relationship is apparent in either region.

Table 3.1 lists the linear correlation coefficients between $\overline{w}_c$ and $\overline{TB}$, $\overline{w}_c$ and DIAM, and $\overline{TB}$ and DIAM as a function of altitude and region for both updraft and downdraft cores. For updraft cores, the positive correlations exhibit an increase with altitude that become statistically significant (according to a $t$-test) by 5.5 km (4.2 km) in the eyewall (rainband) region. This significant increase suggests that a greater fraction of mid-level updraft cores are larger, stronger, and more buoyant than low-level updrafts. Given the

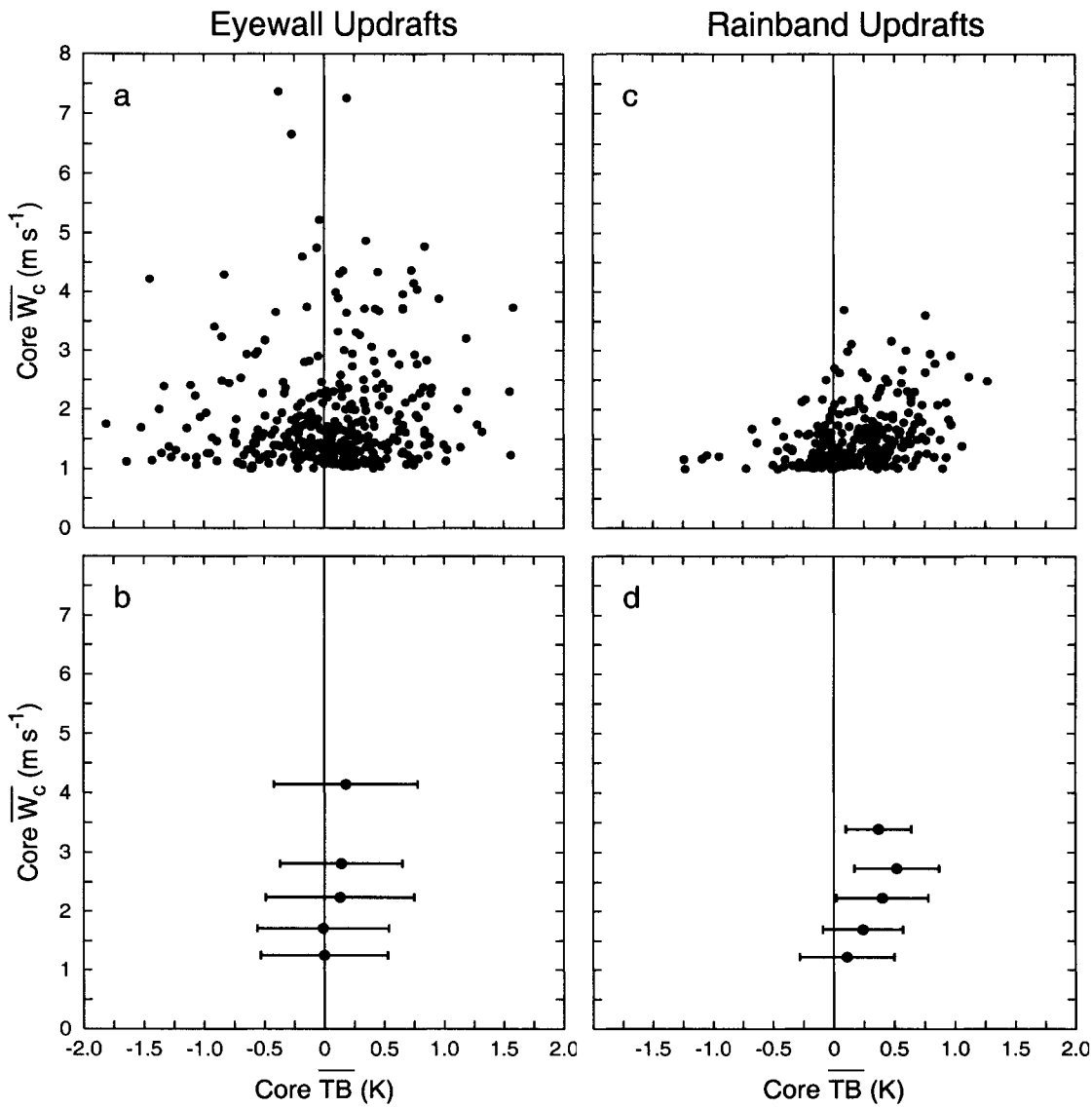


Figure 3.6: Scatterplots of updraft core average convective vertical velocity $\overline{w}_c$ versus average thermal buoyancy $\overline{TB}$ in the (a) eyewall and (c) rainband regions. Averages of $\overline{TB}$ taken over specified $\overline{w}_c$ intervals are shown in the lower panels for the (b) eyewall and (d) rainband cores. The average values in (b) and (d) are depicted by circles and the standard deviations are shown as error bars. The vertical velocity intervals used were 1.0 $< \overline{w}_c <$ 1.5 m s$^{-1}$, 1.5 $< \overline{w}_c <$ 2.0 m s$^{-1}$, 2.0 $< \overline{w}_c <$ 2.5 m s$^{-1}$, 2.5 $< \overline{w}_c <$ 3.0 m s$^{-1}$, and $\overline{w}_c >$ 3.0 m s$^{-1}$.

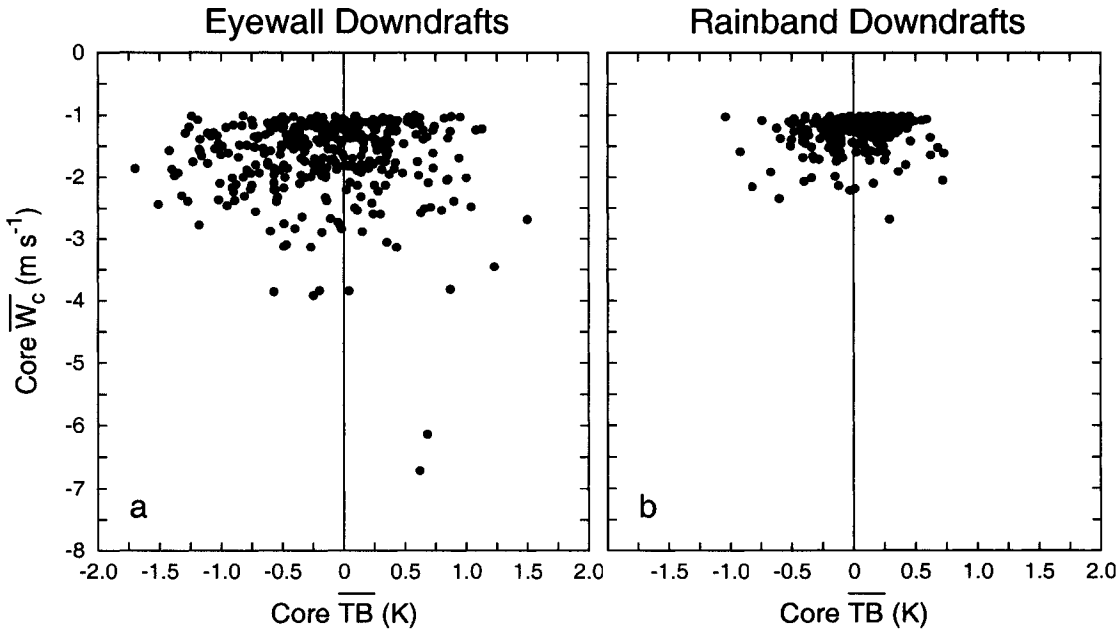


Figure 3.7: Scatterplots of downdraft core average convective vertical velocity $\overline{w}_c$ versus average thermal buoyancy $\overline{TB}$ in the (a) eyewall and (b) rainband regions.

strong positive correlation between updraft core magnitude and mass transport noted by JZL, the correlation increases also reflect a tendency for buoyant updrafts to accomplish a greater fraction of upward mass transport at mid-levels than at lower levels. Downdraft cores exhibit no significant or systematic relationship between $\overline{TB}$ and either $\overline{w}_c$ or DIAM at any level. Further stratification of the downdrafts, as discussed above, also revealed no significant relationships.

### 3.5 Percent area occupied by cores

Since the azimuthal distribution of legs was fairly uniform and independent of a given storm's azimuthal convective structure, the fractional area covered by convective cores can be estimated from the fraction of radial legs occupied by cores. Following JZL, we first compute the fractional area of each core as

$$FA = \pi \frac{r_{out}^2 - r_{in}^2}{R_{out}^2 - R_{in}^2} \tag{3.1}$$

Table 3.1: Linear correlation coefficients between core average convective vertical velocity ($\overline{w}_c$), average thermal buoyancy ($\overline{TB}$), and diameter (DIAM) for updraft and downdraft cores in the eyewall and rainband regions. Downdraft core values are shown in parentheses. Bold values are statistically significant at the 95% confidence level.

| Region | Altitude (km) | Number of cores | Linear correlation coefficients | | |
|---|---|---|---|---|---|
| | | | $\overline{w}_c$-$\overline{TB}$ | DIAM-$\overline{TB}$ | $\overline{w}_c$-DIAM |
| Eyewall | 5.5 | 115 (119) | **0.33** ( -0.20) | **0.26** (-0.18) | **0.57** (**-0.51**) |
| | 4.2 | 72 ( 85) | 0.08 ( -0.01) | 0.07 (-0.01) | **0.54** (**-0.57**) |
| | 3.0 | 127 (131) | 0.01 ( 0.11) | -0.07 (-0.09) | **0.57** (**-0.55**) |
| | 1.5 | 37 ( 34) | 0.02 ( 0.20) | 0.03 ( 0.04) | 0.24 (**-0.35**) |
| Rainband | 5.5 | 66 (50) | **0.46** ( -0.20) | 0.16 (-0.14) | **0.53** (**-0.77**) |
| | 4.2 | 68 (47) | **0.59** ( 0.19) | **0.39** ( 0.13) | **0.70** (**-0.64**) |
| | 3.0 | 105 (86) | **0.19** ( -0.10) | 0.09 (-0.03) | **0.65** (**-0.62**) |
| | 1.5 | 30 (18) | 0.03 ( -0.21) | 0.30 (-0.16) | **0.47** (**-0.58**) |

where $r_{in}$ and $r_{out}$ are the radii of the core's inner and outer edges, and $R_{in}$ and $R_{out}$ are the inner and outer radial extents of the desired region (eyewall, rainband, or entire leg). The percent area coverage was computed by summing the $FA$ of each core encountered during a given leg and then averaging over all legs. The mean radial leg extends from ~15 km to ~115 km with a mean radial cutoff between the eyewall and rainband region at ~45 km, which corresponds to the average areas of ~4.1 $\times$ $10^4$ km$^2$, ~0.6 $\times$ $10^4$ km$^2$, and ~3.5 $\times$ $10^4$ km$^2$ for the inner core, eyewall, and rainband regions, respectively.

Updraft and downdraft cores were found to occupy 4.1% and 2.9% of the total area inside 115 km, respectively. Updrafts exhibited an increase in percent area from 1.3% at 1.5 km to 4.9% at 5.5 km, while downdrafts displayed little variation with altitude. JZL estimated that updraft and downdraft cores occupied 9% and 4% of the total area inside 137 km, and noted similar variability with altitude. Black et al. (1996) estimated that updrafts and downdrafts, derived from Doppler radar data, covered 13% and 4% of the total area inside 100 km. The differences in percent area between studies are largely attributable to differences in data resolution and core definition. Despite such differences,

the consistent results suggest that a relatively small area of an intense hurricane's inner core is covered by significant convective-scale vertical motions.

Figure 3.8 shows the percent area of the eyewall and rainband regions occupied by updraft and downdraft cores with $\overline{w}_c$ and $\overline{B}$ greater than the values indicated. For example, updraft cores occupied 9.9% of the total eyewall area, but updrafts with either $\overline{w}_c > 2$ m s$^{-1}$ or $\overline{B} > 0$ K occupied only ~5% of the same area. Such results indicate that updraft cores, despite greater concentration in the eyewall, still occupy only a small fraction of the eyewall area; buoyant updrafts occupied an even smaller fraction. In the rainband region, updraft cores covered only 2.9% of the total area, with ~2.5% of the area occupied by buoyant ($\overline{B} > 0$ K) updrafts. Downdraft cores occupied only 9.2% of the eyewall area and only 2.3% of the the rainband area.

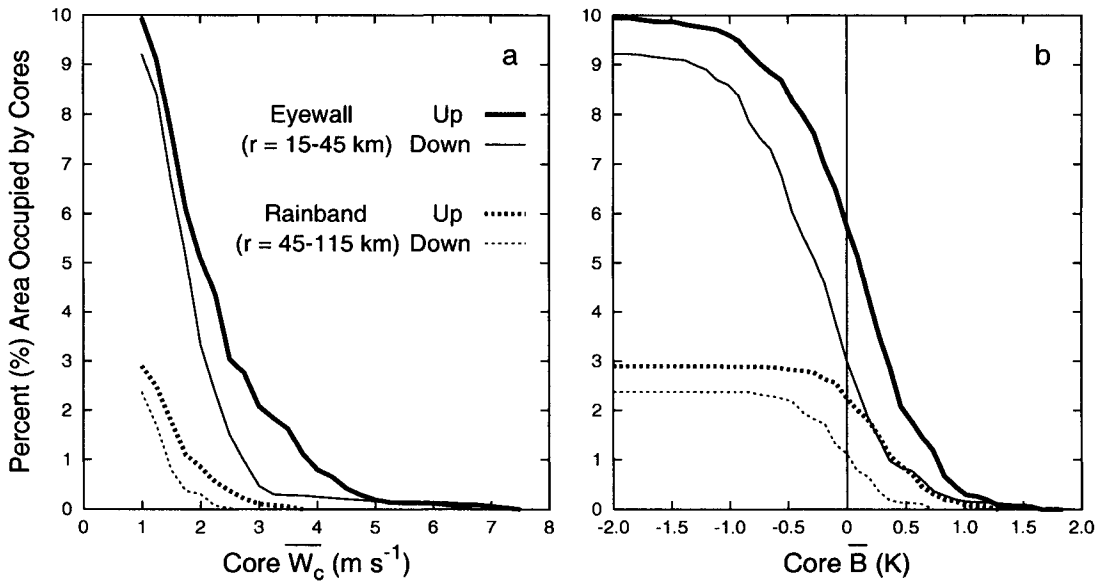


Figure 3.8: Percent area of the eyewall (solid) and rainband (dashed) regions occupied by updraft (thick) and downdraft (thin) cores with (a) average convective vertical velocities $\overline{w}_c$ and (b) average total buoyancies $\overline{B}$ greater than the magnitude given on the abscissa.

### 3.6 Typical convective core radial structure

The typical radial structure of a convective updraft and downdraft core was determined for each region using a combination of superposed epochs described by Panofsky and Brier (1968) and one-point correlation methods outlined by Wallace et al. (1988).

The $w_{c\ max}$ of each core were sequentially ordered to define the "epoch series". Radial profiles of $w_c$ through each core were then sequentially placed in a coordinate system centered on the epochs with the storm center to the left. One-point correlations were then calculated between the epoch series and the series of $w_c$ at each 0.5 km radii within 5 km of the epochs. The result is a radial profile of correlation coefficients that describes the typical continuity of $w_c$ about the $w_{c\ max}$ of each core. Next, a Monte Carlo method described by Neumann et al. (1977) was used to determine the significance of each correlation coefficient. The $w_c$ series surrounding each epoch was randomly ordered, and correlation coefficients were computed for 100 different randomizations of the series. The significance levels of the observed correlations were then estimated from the distribution of correlation coefficients of the randomly order series. The one-point correlation process was then repeated for profiles of $TB$, $DB$, $B$, $q_c'$, and $q_r'$ through each core using the same epoch series. Each resulting radial profile describes the typical relationship between the given parameter and $w_c$ at the epoch, as well as the continuity of that relationship about the epoch. This correlation method was chosen over compositing in order to prevent a few anomalous large magnitude events from biasing statistically significant structure derived from many smaller magnitude events. It should be noted, however, that the composited radial structure (not shown) highlights much of the same significant structure captured by the correlation analysis.

Figure 3.9 shows the resulting correlation profiles across updrafts and downdrafts in the eyewall and rainband regions. The bold horizontal lines delineate the correlation coefficient magnitudes for which all parameters at each radii are statistically significant at the 95% level. Updraft and downdraft cores of each region exhibit similar statistically significant correlations of $w_c$ that are symmetric about $w_{c\ max}$ and extend $\sim$1.5 km to each side. [Note that, by definition, $w_c$ is perfectly correlated with itself at the epoch.] This symmetric, quasi-linear, decrease in correlations illustrates that the typical radial structure of $w_c$ through convective updraft and downdraft cores resembles a "triangle". JZL also noted a triangular structure. Furthermore, the significant negative correlations

of $w_c$ located 3-4 km primarily outside (inside) updraft (downdraft) cores of each region reflect the organizational tendency within hurricanes for convective downdrafts to reside at radii just beyond convective updrafts (e.g., JZL; Black and Hallet 1986).

Considerable variability in the radial structure of liquid water content and buoyancy within convective updrafts was found between eyewall and rainband cores. For eyewall updrafts (Fig. 3.9a), $q_c^{'}$ is highly correlated with $w_{c\ max}$ across the entire core, but $q_r^{'}$ correlations are significant only in the outer half of the core. Furthermore, both $TB$ and $B$ exhibit significant positive correlations within the core inside $w_{c\ max}$, but exhibit significant negative correlations along the outer edge of the core. In contrast, rainband updrafts (Fig. 3.9c) exhibit significant nearly symmetric $q_c^{'}$, $TB$, and $B$ structure about the epoch, but no dominant $q_r^{'}$ structure. No significant $DB$ structure is found in either eyewall or rainband updrafts. High positive correlations between cloud water and updraft velocity within hurricanes are well established (Doster and Willis 1976; Jorgensen 1984a). The contrasting $q_r^{'}$ structure reflects the organizational tendency for eyewall updrafts, compared to rainband updrafts, to consistently slope outwards with raindrops falling out of the updrafts at larger radius (Jorgensen 1984a). A possible explanation for the contrasting $TB$ and $B$ structure is differential effects of entrainment due to the contrasting radial profiles of background equivalent potential temperature. The eyewall region typically contains a strong radial gradient of $\theta_e$ in which values decrease with radius, but in the rainband region $\theta_e$ gradients are much weaker (Eastin et al. 2002). Thus, given a buoyant eyewall updraft (i.e., a positive $\theta_e$ anomaly), entrainment mixing along the inner (outer) edge advects higher (lower) $\theta_e$ into the core and helps maintain (erode) the local buoyancy. In contrast, entrainment mixing on either side of a buoyant rainband updraft will act to erode the local buoyancy.

In general, the radial structures of $q_c^{'}$, $q_r^{'}$, $TB$, $DB$, and $B$ within either eyewall or rainband downdraft cores were not statistically significant. Only eyewall downdrafts (Fig. 3.9b) exhibited a significant $q_c^{'}$ ($q_r^{'}$) maximum towards the inner (outer) edge that supports the tendency for eyewall downdrafts to be located just outside updraft cores

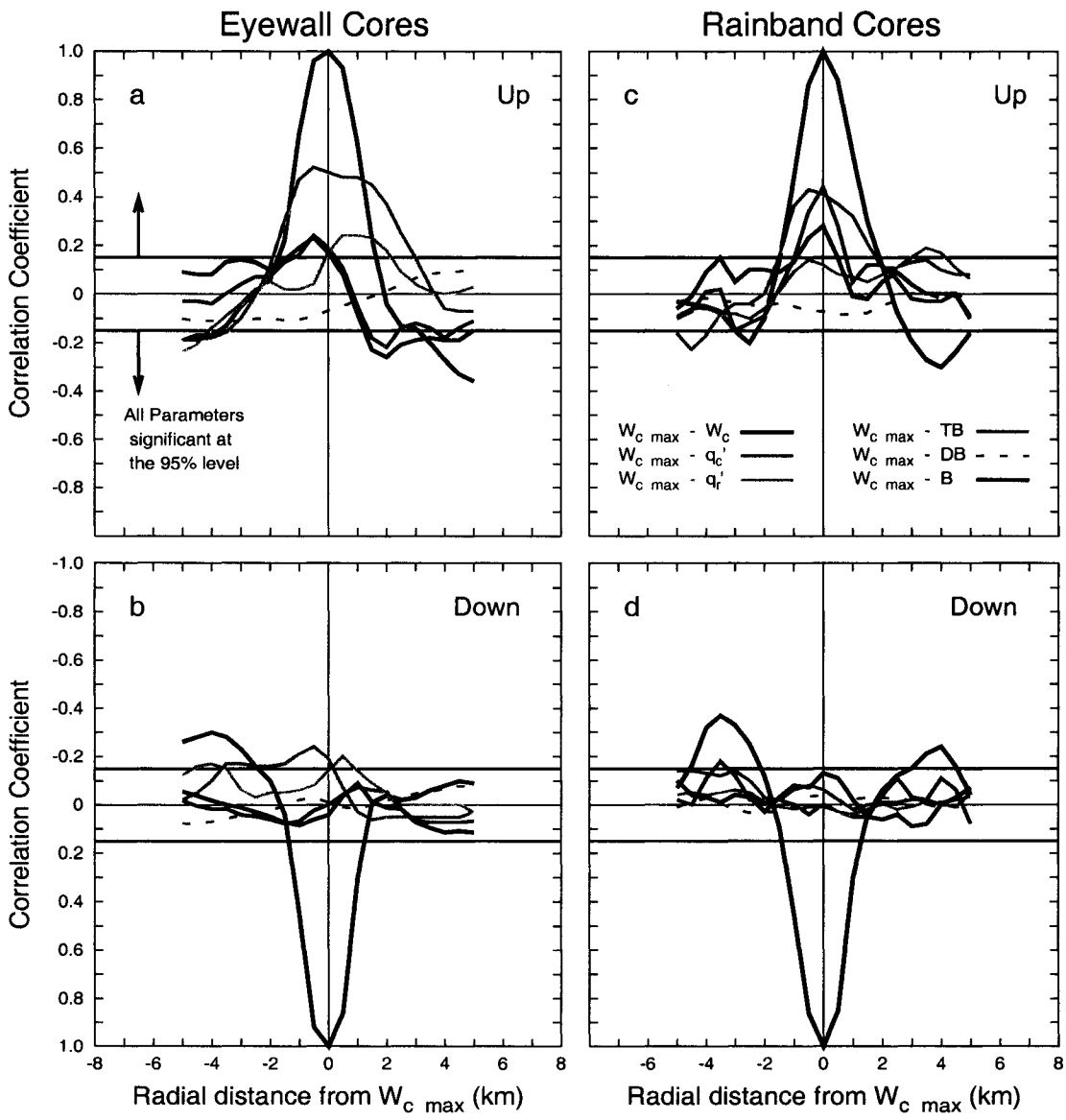


Figure 3.9: Correlations between the core convective vertical velocity maxima $w_{c\ max}$ and local radial profiles of $w_c$ (thick black), thermal buoyancy $TB$ (red), dynamic buoyancy $TB$ (dashed black), total buoyancy $B$ (dark blue), perturbation cloud water content $q_c$' (green), perturbation precipitation water content $q_r$' (light blue), and convective radial velocity $V_r$' in the eyewall region for (a) updraft and (b) downdrafts and in the rainband region for (c) updrafts and (d) downdrafts. The horizontal axes are oriented such that the storm center is to the lhs of the figure. Solid horizontal lines at $\pm 0.15$ indicate the minimum correlations for which all parameters at each radii are significant at the 95% level. Note that ordinate labeling of (b) and (d) is opposite that of (a) and (c).

and to contain some liquid water. The overall lack of consistent radial structure in $TB$ or $B$ reflects the substantial impact that total vertical velocity and variable liquid water content (and likely drop-size distribution) can have upon buoyancy due to the opposing effects of latent heating (cooling) and adiabatic cooling (warming), as discussed previously in Section 3.3.

## 3.7 Discussion

### 3.7.1 Vertical acceleration of typical convective updraft cores

Emanuel (1986) has argued that the hurricane inner core is close to a state of moist neutrality in which equivalent potential temperature and absolute angular momentum surfaces are parallel. As a result, eyewall updrafts are neutrally buoyant with minimal vertical acceleration above the boundary layer. Rotunno and Emanuel (1987) used the temporally averaged (over 20 h) fields from a non-hydrostatic axisymmetric hurricane simulation with 15 km horizontal grid spacing to qualitatively support this claim. Zhang et al. (2000) examined the inner-core vertical momentum budget using azimuthally and temporally (over 1 h) averaged budget terms from an explicit three-dimensional simulation of Hurricane Andrew (1992) with 6 km horizontal grid spacing. The mean eyewall was moist neutral to a first approximation in agreement with Rotunno and Emanuel (1987). Small vertical accelerations of the mean eyewall updraft above the boundary layer were attributed to upward-directed perturbation pressure gradient forces. Braun (2002) examined the vertical momentum budget along individual eyewall updraft trajectories using 2-min output from an explicit three-dimensional simulation of Hurricane Bob (1991) with 1.3 km horizontal grid spacing. In contrast to Zhang et al. (2000), perturbation pressure gradient forces were directed downward and positive total buoyancy forces were argued to drive the modest updraft accelerations found above the boundary layer. Therefore, these numerical model results suggest that while the azimuthally-averaged mesoscale eyewall may be neutral or negatively buoyant with minimal updraft acceleration, individual convective updrafts may exhibit appreciable positive buoyancy and upward acceleration. What do the observations of "typical" eyewall and rainband convective updraft cores suggest?

The median $\overline{w}_c$ statistics for eyewall and rainband updraft cores depict a slight increase in strength with altitude (i.e., an acceleration) above the boundary layer. Updraft core median $\overline{B}$ statistics are also slightly positive below ~4 km in eyewalls and below ~6 km in rainbands. Given the large variability in $\overline{w}_c$ and $\overline{B}$ at each level, the median profiles were tested to determine if such vertical structure was statistically significant and representative of typical hurricane convective updraft cores. Figure 3.10 shows the median and mean profiles of $\overline{w}_c$ and $\overline{B}$ for eyewall and rainband updraft cores. The means exhibit good agreement with the median statistics in magnitude and vertical structure. In both regions, differences in $\overline{w}_c$ means between successive altitudes were not systematically statistically significant, but differences between means at 1.5 km and means at either 4.2 or 5.5 km were significant at the 95% level. Mean eyewall (rainband) $\overline{B}$ at 1.5 and 3.0 km altitude (3.0 and 4.2 km) were also significantly greater than zero at the 95% level. Two additional tests were made to check the robustness of such $\overline{w}_c$ and $\overline{B}$ vertical structure. First, updraft cores at each level were randomly divided into two halves, and median statistics were re-computed for each half. Second, updraft cores were re-identified using reference states defined by 10 and 15 km filter windows (rather than 20 km), and median statistics were re-computed. All resulting median $\overline{w}_c$ and $\overline{B}$ profiles were in good agreement (see Fig. 3.10), which further implies that the vertical structure is not an artifact of the database or reference state used. Therefore, the statistically significant median vertical structure of $\overline{w}_c$ and $\overline{B}$ suggests that typical hurricane updraft core accelerations may be a result of appreciable positive buoyancy forces.

We can elucidate the relative roles played by total buoyancy and the perturbation pressure gradient force in vertically accelerating eyewall and rainband convective updraft cores through a rough calculation with a one-dimensional updraft model. In the absence of lateral forcing or entrainment mixing, the convective vertical momentum equation can be written as:

$$\frac{dw_c}{dz} = \frac{1}{w_c}\left[\frac{1}{\rho}\frac{dp'}{dz} + B\right] \tag{3.2}$$

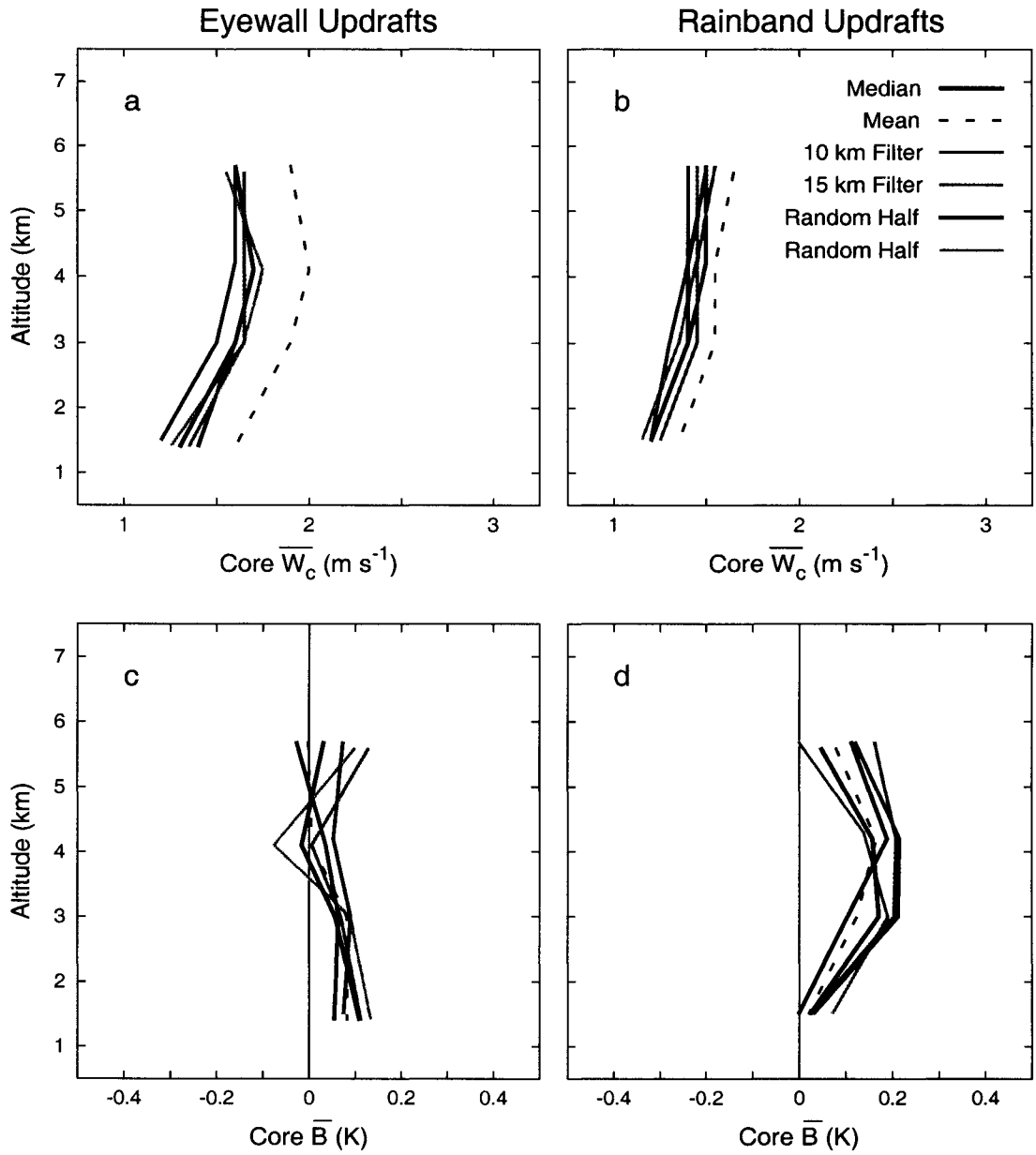


Figure 3.10: Variation with altitude of median (solid black) and average (dashed black) updraft core average convective vertical velocity $\overline{w}_c$ in (a) eyewalls and (b) rainbands, and average total buoyancy $\overline{B}$ in (c) eyewalls and (d) rainbands. Also shown are median values when the reference state is redefined using a 10 km (red) and 15 km (green) running Barlett filter, and median values when the present distributions are randomly divided into two halves (dark and light blue).

where $\overline{w}_c$, $p'$, and $B$ are defined as before, $\rho$ is the density of air, and the first term inside the bracket is the vertical perturbation pressure gradient force ($VPPGF$). We apply to Eq. (3.2) the median statistics from each region in order to capture the behavior of a typical updraft core. In other words, we assume the buoyancy properties of a typical updraft evolve with altitude as the median $\overline{B}$ profile evolves. Unfortunately, observational estimates of the $VPPGF$ are beyond the capabilities of current instrumentation. Therefore, we use Eq. (3.2) to derive profiles of expected updraft core $\overline{w}_c$ forced from total buoyancy alone, and then infer the relative $VPPGF$ contribution from the difference between the expected and observed $\overline{w}_c$ profiles. To determine the expected $\overline{w}_c$ profiles, Eq. (3.2) is integrated upward from 1.5 km, using the median $\overline{w}_c$ at 1.5 km as the lower boundary condition. Clearly this simple model has shortcomings, but a more sophisticated treatment is not justified without detailed observational knowledge of the local three-dimensional kinematic and thermodynamic environment in which the updraft cores rise.

Figure 3.11 shows the profiles of observed and expected median $\overline{w}_c$ for eyewall and rainband updraft cores. In both regions, the expected $\overline{w}_c$ from $\overline{B}$ alone exhibit substantially more vertical acceleration than observed, resulting in 5-6 m $s^{-1}$ stronger updrafts at 5.5 km. Note that the expected eyewall $\overline{w}_c$ also exhibits a weak deceleration above 4.2 km (due to negative $\overline{B}$ at 4.2 km) in agreement with the observed profile. Inferring the $VPPGF$ contribution as the residual, the profiles suggest that a typical $VPPGF$ acting on an updraft core is directed downward and largely opposes the positive buoyancy force. The results further imply that buoyancy is the primary force vertically accelerating typical hurricane eyewall and rainband updraft cores above the boundary layer. Such findings are consistent with the results of Braun (2002), but contrast the results of Zhang et al. (2000).

Figure 3.11 also shows the expected $\overline{w}_c$ profiles from integrating Eq. (3.2) with the median $\overline{TB}$ statistics of each region. Differences between the $\overline{B}$ and $\overline{TB}$ expected profiles are small, but illustrate that $\overline{WL}$ (and to a lesser degree $\overline{DB}$) acts to decelerate updrafts, as expected. To crudely account for the possible underestimation of total $q_c$ discussed in Chapter 2.2, expected $\overline{w}_c$ profiles were re-computed from the median $\overline{B}$ statistics with an

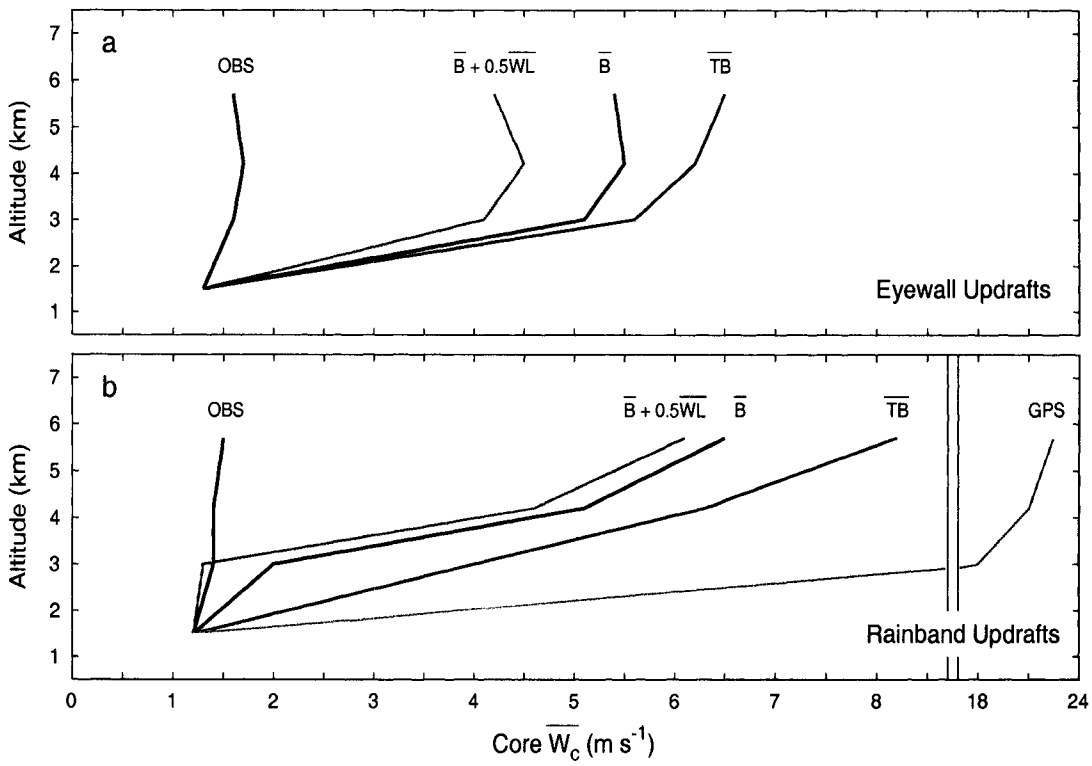


Figure 3.11: Variation with altitude of the observed (a) eyewall and (b) rainband updraft core median average convective vertical velocity $\overline{w}_c$ (OBS, solid black) and the $\overline{w}_c$ values expected from parcel theory (Eq. 3.2) using the median values of core average thermal buoyancy ($\overline{TB}$, red), core average total buoyancy ($\overline{B}$, dark blue), core average total buoyancy with 50% additional water loading ($\overline{B} + 0.5\overline{WL}$, green), and thermal buoyancy derived from GPS dropsondes assuming moist-adiabatic ascent of the lowest 500 m ($GPS$, light blue).

additional 50% median $\overline{WL}$. Again, differences in expected profiles are small and do not alter the overall conclusions.

Figure 3.11 clearly suggests that the *net* $VPPGF$ plays a significant role in decelerating typical updrafts. However, note that the median $\overline{w}_c$ for rainband updraft cores depict less vertical acceleration than their eyewall counterparts despite larger positive $\overline{B}$ values. Such discrepancy may be related to differing roles played by the dynamic and buoyant contributions that comprise the net $VPPGF$. Following Rotunno and Klemp (1982), the buoyancy contribution arises solely from the vertical perturbation pressure gradients induced by the local buoyancy anomaly, and thus, is directly proportional to and largely opposes the local buoyancy. The dynamic contribution arises from pressure perturbations induced by local three-dimensional wind shear and stretching, and thus, can provide either positive or negative forcing upon a buoyant updraft. Diagnosis of each contribution is beyond the scope of this study, but results from Zhang et al. (2000) suggest that the dynamic contribution arises primarily from vertical gradients in radial shear of the tangential wind. Given that radial gradients of tangential wind are typically greatest near the outward-sloping RMW, one might expect the magnitudes of the dynamic contribution to be much larger for eyewall updrafts than for rainbands updrafts. Therefore, it seems plausible that the typical net $VPPGF$ for rainband updrafts is largely comprised of a downward-directed buoyancy contribution with a minimal dynamic contribution. In contrast, the typical net $VPPGF$ for eyewall updrafts may contain an appreciable upward-directed dynamic contribution that partially opposes the downward-directed buoyancy contribution (or assists in updraft acceleration).

For simplicity, our updraft model neglected the effects of entrainment mixing. We can assume, however, that the net thermodynamic effects of entrainment are implicit within the median $\overline{TB}$ statistics at each level. Therefore, the thermodynamic effects of entrainment on typical updraft accelerations can be inferred through comparison of expected $\overline{w}_c$ derived from representative median $TB$ statistics for *undilute* moist ascent with expected $\overline{w}_c$ derived from the observed median $\overline{TB}$ profile for the updraft cores.

Estimates of undilute $TB$ were obtained from 223 GPS dropwindsonde soundings collected in the inner core of 8 intense hurricanes.[2] Quality-controlled soundings were acquired from the NOAA HRD data archive and further scrutinized following the methods of Bogner et al. (2002) to correct for any mixed-layer humidity sensor wetting errors.[3] Next, the sondes were subjectively stratified into eyewall (127 sondes) and rainband (96 sondes) regions using methods consistent with the convective core stratification. Vertical profiles of undilute $TB$ were then calculated for each sounding as the difference in $\theta_v$ between a parcel lifted pseudo-adiabatically from the boundary layer and the observed sounding. The lifted parcel was characterized by the mean thermodynamic conditions in the lowest 500 m. Finally, undilute $TB$ values were extracted from the profiles at each available reference altitude (1.5, 3.0, 4.2, and 5.5 km) and tabulated.

Figure 3.12 shows the vertical profiles of updraft core median $\overline{TB}$ and undilute parcel median $TB$ for eyewalls and rainbands. Also shown for comparison is the undilute $TB$ profile computed from the Frank (1977) composite typhoon sounding at ~80 km radius. In the rainband region (Fig. 3.12b), both undilute profiles indicate that typical updraft cores should exhibit $\overline{TB} > 1$ K at 4.2 km altitude, rather than the 0.24 K observed. Clearly entrainment was acting to reduce the core $\overline{TB}$ values. The substantial net effect upon updraft acceleration is illustrated in Fig. 3.11b through comparison of expected $\overline{w}_c$ assuming undilute ascent (GPS) with the expected $\overline{w}_c$ derived from the median $\overline{TB}$ profile. Entrainment effectively reduced $\overline{w}_c$ at 5.5 km by ~14 m s$^{-1}$, which was a larger net contribution than either $WL$ (~2 m s$^{-1}$) or the $VPPGF$ (~5 m s$^{-1}$). In the eyewall region (Fig. 3.12a), undilute median $TB$ are near neutral (~0.02 K) and *less* than the statistically

---

[2]GPS soundings and adequate flight-level data to analyze convective core buoyancy characteristics were only concurrently obtained during the Guillermo 970803I and Georges 980919H flights. As a result, most updraft core $\overline{TB}$ are not directly comparable to individual undilute $TB$ values. However, profiles of median undilute $TB$ from each region should be representative given the small variability in gross thermodynamic vertical structure that is consistently observed from storm to storm (e.g., Bogner et al. 2000).

[3]Humidity sensor wetting errors may still exist above the mixed layer. Any such errors will result in an over-estimate of relative humidity, and thus an under-estimate of undilute $TB$.

significant updraft core $\overline{TB}$ values. How might such results be interpreted? Given that the GPS soundings collectively provide a mesoscale representation of the quasi-vertical structure, the results support the idea that several locally buoyant convective updrafts are embedded within a near-neutral mesoscale eyewall. [Potential source regions of these buoyant updrafts are discussed in Chapter 4.5.2.] Evidence of detrimental entrainment is limited to the slight decrease in core $\overline{TB}$ with height. Given the large Rossby numbers typically found in the eyewall region (Shapiro and Montgomery 1993), such a limited effect from entrainment is not surprising. Helfrich (1994) and Ayotte and Fernando (1994) have demonstrated experimentally that thermals (or buoyant updraft cores) ascending in rapidly-rotating environments (i.e., the eyewall region) experience less lateral entrainment than their counterparts in nonrotational environments.

The fact that condensate freezing can invigorate an updraft that ascends above the 0°C level is well known (e.g., Riehl 1979; Williams and Renno 1993; Zipser 2003). Note that above ~4 km the updraft core median $\overline{B}$ profiles (Figs. 3.4 and 3.10) exhibit either neutral conditions or a marked trend towards negative buoyancy, which would limit further core ascent in the absence of mesoscale forcing. However, if a near-neutral updraft core contained ~0.5 g $m^{-3}$ of liquid water upon reaching the freezing level (typical for hurricane updrafts; JZL), total condensate freezing would reinvigorate the updraft with ~0.3 K of $\overline{TB}$ and buoyant ascent could continue. Microphysical observations in hurricane updrafts near the freezing level (~5.5 km in the inner core) suggest that total condensate freezing occurs by −5°C or ~6.5 km altitude (Black and Hallet 1986). Of the updraft cores at 5.5 km, roughly 35% were encountered at temperatures < 0°C. The mean $\overline{TB}$ for these cores was slightly larger (more positive) than the mean $\overline{TB}$ of warmer cores at 5.5 km, but the difference in means was not statistically significant. Nevertheless, hurricane updrafts are observed to be stronger above the freezing level (Marks and Houze 1987; Black et al. 1996), suggesting that condensate freezing plays a significant role in maintaining positive buoyancy and upward accelerations against entrainment, water loading, and downward-

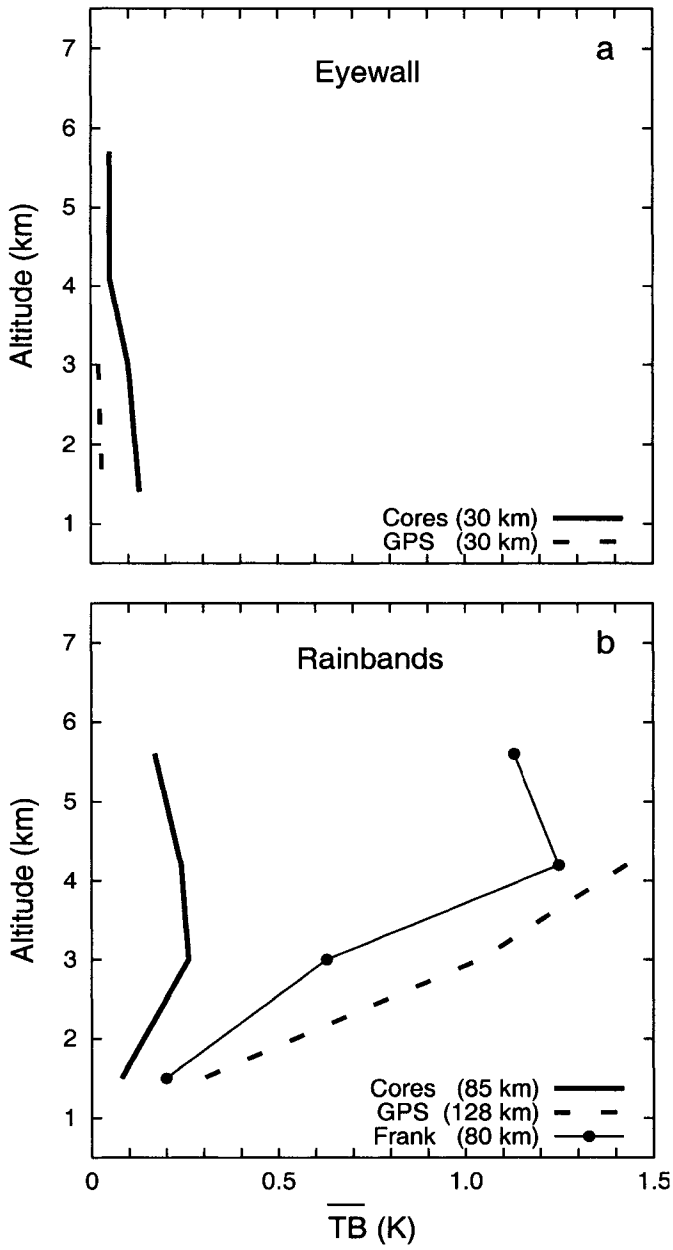


Figure 3.12: Variation with altitude of the observed (a) eyewall and (b) rainband updraft core median average thermal buoyancy $\overline{TB}$ (solid line) and the median thermal buoyancy derived from GPS dropsondes (dashed line) deployed in each region (127 eyewall; 96 rainband) assuming moist-adiabatic ascent of the lowest 500 m. Shown for comparison in the rainband region are the thermal buoyancy values derived from the Frank (1977) composite typhoon sounding at r = 80 km assuming moist-adiabatic ascent of the lowest 50 mb (closed circles joined by solid line). Values in parentheses are the average radii of the cores or soundings used to determine the median values in each region. GPS-derived median values are only shown at levels with at least 30 individual estimates in order to ensure an adequate statistical sample.

directed pressure gradient forces. Such arguments are consistent with the modeling results of Lord et al. (1984).

On a final note concerning updraft accelerations, Emanuel (1986) contends that any small updraft accelerations are the result of slantwise instabilities in which air parcels are accelerated both upward by local buoyancy forces and outward by local inertial forces. The results of this study clearly demonstrate that the majority of inner-core updraft cores exhibit appreciable positive buoyancy which can support significant upward accelerations. The majority of cores were also associated with positive (outward) radial velocities indicative of slantwise ascent. However, the question of whether updraft cores also experience significant radial accelerations remains to be answered and is left for future work.

### 3.7.2 Vertical transport by convective updraft cores

Malkus and Riehl (1960) argued that a large fraction of the mass required to reach upper levels ascended rapidly in a few isolated buoyant "hot towers" rather than in a more uniform ring of gradual mesoscale ascent. We have shown that convective updraft cores occupy less than 10% of the eyewall and rainband areas. However, the question remains as to how much of the total upward mass, heat, and moisture transports are accomplished by these convective cores, particularly the buoyant cores.

To elucidate the convective core contribution to the total transports in a typical intense hurricane, we first follow JZL and compute the convective mass, sensible heat, and latent heat transports per unit length normal to the flight track for each updraft core as

$$MT_c = \rho \overline{w}_c \mathrm{DIAM} \tag{3.3}$$

$$SHT_c = \rho c_p \overline{\theta} \overline{w}_c \mathrm{DIAM} \tag{3.4}$$

$$LHT_c = \rho L_v \overline{q w}_c \mathrm{DIAM} \tag{3.5}$$

where $\rho$, $\overline{w}_c$, and DIAM are defined as before, $\overline{\theta}$ is the core average potential temperature, $\overline{q}$ is the core average specific humidity, $c_p$ is the specific heat of air at constant pressure, and $L_v$ is the latent heat of vaporization. The respective net convective contributions were then estimated by summing the $MT_c$, $SHT_c$, and $LHT_c$ of each updraft core encountered over all legs. Only updraft cores with $\overline{w} > 1.0$ m s$^{-1}$ were included. Next, the total upward mass, sensible heat, and latent heat transports per unit length normal to the flight track along each leg were computed as

$$MT = \rho \overline{w}_{leg} \mathrm{L} \tag{3.6}$$

$$SHT = \rho c_p \overline{\theta}_{leg} \overline{w}_{leg} \mathrm{L} \tag{3.7}$$

$$LHT = \rho L_v \overline{q}_{leg} \overline{w}_{leg} \mathrm{L} \tag{3.8}$$

where L is the leg length, and $\overline{w}_{leg}$, $\overline{\theta}_{leg}$, and $\overline{q}_{leg}$ are the arithmetic mean total upward vertical velocity, potential temperature, and specific humidity, respectively, along the leg. The respective net total contributions were then computed by summing the leg $MT$, $SHT$, and $LHT$ over all legs. Finally, the percent total upward transports by the updraft cores were estimated by dividing each of the $MT_c$, $SHT_c$, and $LHT_c$ net contributions by their respective $MT$, $SHT$, and $LHT$ net contributions.

Figure 3.13 shows the percents of total upward mass transport accomplished by convective updraft cores as a function of $\overline{w}_c$ and $\overline{B}$ greater than the values indicated. Updraft cores were found to accomplish ~64% and ~51% of the total upward mass transport in the eyewall and rainband regions, respectively. The percentage increased with altitude (not shown) from 57% at 1.5 km to 66% at 5.5 km in the eyewall region, but exhibited no systematic altitude variation in rainbands. Such percentages are consistent with Black et al. (1996) and Braun (2002) despite different data sources, data resolution, updraft core definitions, and average region areas. More importantly, comparison of Figs. 3.8 and 3.13 reveals that while eyewall updraft cores with either $\overline{w}_c > 2$ m s$^{-1}$ or $\overline{B} > 0$ K occupied <

5% of the total area, they accomplished ~40% of the total upward mass transport. Such cores in the rainband region occupied < 3% of the area but accomplished ~30% of the total upward mass transport.

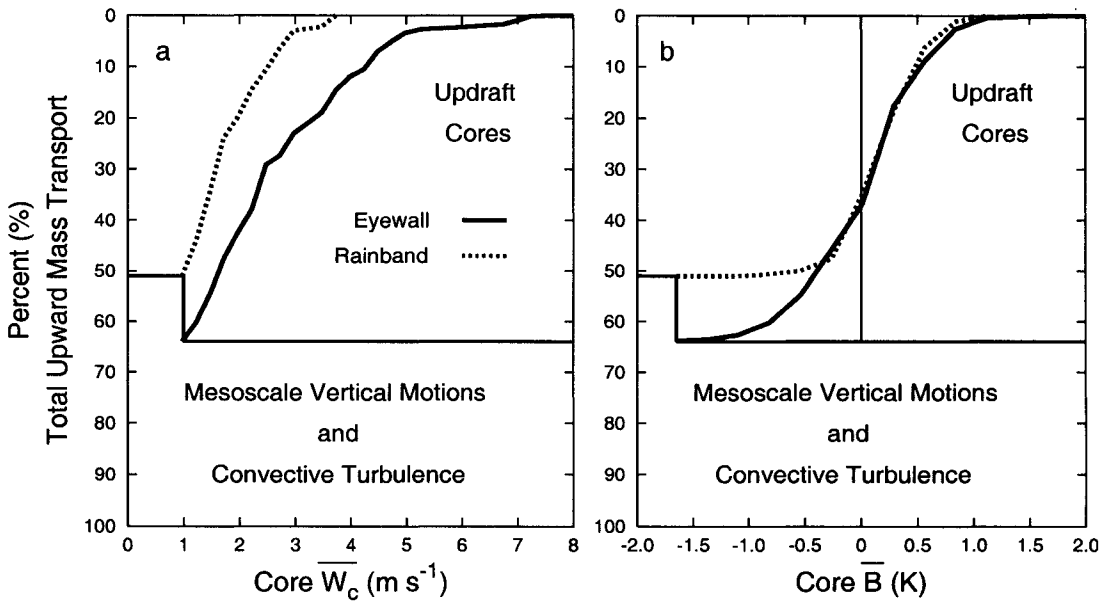


Figure 3.13: Percent of the total upward mass transport accomplished by eyewall (solid) and rainband (dashed) updraft cores with (a) average convective vertical velocities $\overline{w}_c$ and (b) average total buoyancies $\overline{B}$ greater than the magnitude given on the abscissa. The percent total upward mass transport accomplished by mesoscale updrafts and convective turbulence in each region lies below the horizontal lines.

Figures 3.14 and 3.15 show the percents of total upward sensible and latent heat transports accomplished by convective updraft cores as a function of $\overline{w}_c$ and $\overline{B}$ greater than the values indicated. Percentages are nearly identical to those for the mass transport. Clearly, buoyant updraft cores make a significant contribution to the total upward mass, heat, and moisture transports in the hurricane inner core.

The percent core contribution to the total upward transport, as defined, is a weak function of the reference state. Sensitivity tests were conducted by re-identifying cores and re-computing the percent core contributions using filter windows that ranged from 10-30 km. As expected, smaller (larger) filter windows decreased (increased) the percent core contributions, but never by more than ±10% from the values shown in Figs. 3.13-3.15

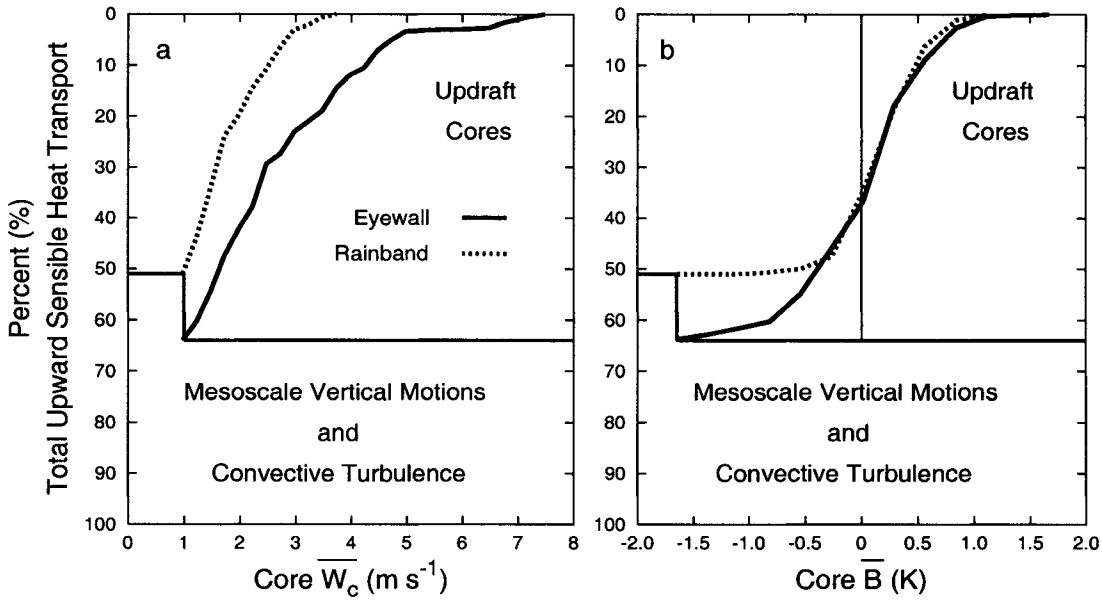


Figure 3.14: As in Fig. 3.13 but for the total upward sensible heat transport.

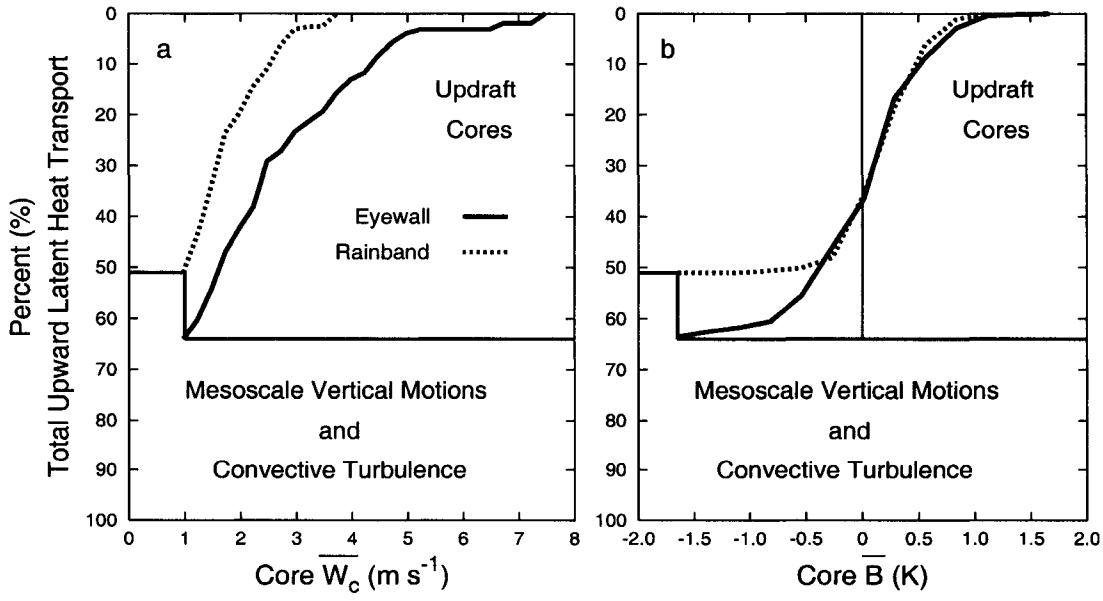


Figure 3.15: As in Fig. 3.13 but for the total upward latent heat transport.

for a 20 km filter window. Therefore, the overall conclusion that buoyant updraft cores transport a considerable fraction of the total mass, heat, and moisture remains unchanged.

# Chapter 4

# CASE STUDIES

The case studies examined here in greater detail are eastern Pacific Hurricane Guillermo on 2 and 3 August 1997, Atlantic Hurricane Edouard on 27 August 1996, and Atlantic Hurricane Georges on 19 September 1998. The intensity, motion, and large-scale environment characteristics for each hurricane during the inner-core observation periods are listed in Table 2.2. These cases will be utilized to illustrate typical azimuthal convective organization, to demonstrate that the low-level eye can be an important source region of buoyant convective updrafts observed in the eyewall, and to provide evidence of three physical links between buoyant convection and storm evolution. Despite significant differences in intensity change and environmental conditions between cases, many of our presented findings are markedly robust (see Appendix) and may be representative of a larger group of hurricanes.

## 4.1 Hurricane Guillermo on 02 August 1997

The inner core of Hurricane Guillermo was observed by the two NOAA WP-3D aircraft between 1800 UTC on 2 August and 0100 UTC on 3 August 1997. Lawrence (1999) gives a detailed account of the history of Guillermo. During this inner-core observation period, Guillermo was located 850 km south-southwest of Puerto Vallarta, Mexico, and was moving at 4.5 m $s^{-1}$ toward the west. Maximum observed flight-level winds were 61 m $s^{-1}$ at 3.0 km altitude, and the average MSLP was 950 mb. Sea surface temperatures were above 29°C, and moderate vertical shear was oriented from north to south. Guillermo was rapidly deepening, according to the criteria established for typhoons by Holliday and Thompson (1979), with an average drop in MSLP of 2.4 mb $hr^{-1}$. The lower

aircraft (NOAA-42 or H) made 10 eye penetrations (20 radial legs) at 3.0 km altitude and the upper aircraft (NOAA-43 or I) made 6 eye penetrations at 5.5 km altitude. All quadrants were well sampled by each aircraft. Radiometric temperature data was only available from the upper aircraft, and thus further analysis in regards to convective core buoyancy characteristics was limited to the 12 radial legs at 5.5 km.

Figure 4.1 shows horizontal single-scans of radar reflectivity obtained from the upper aircraft lower-fuselage (LF) C-band (5.5-cm wavelength) radar antenna during each eye penetration. The radar data was mapped into a storm-relative coordinate system using an objectively constructed track from flight-level winds (Willoughby and Chelmow 1982). Superimposed upon the reflectivity fields are the radial legs that comprise each penetration. Initially at 1859 UTC (Fig. 4.1a), the eyewall, located at a radius of 20-40 km, was elliptical and asymmetric with enhanced convection (> 30 dBZ) on the east side. By 1935 UTC (Fig. 4.1b) the primary eyewall band had rotated cyclonically to the northeast and propagated radially outward. Furthermore, several isolated convective cells had developed in each quadrant of the eyewall as the reflectivity interface between the eye and eyewall acquired a higher wavenumber appearance. Recent studies (e.g., Montgomery and Kallenbach 1997; Schubert et al. 1999; Reasor et al. 2000; Kossin and Schubert 2001) have suggested that such reflectivity structure and evolution is evidence of vortex Rossby waves and mesovorticies embedded within the eyewall. Upon the third eye penetration at 2115 UTC (Fig. 4.1c), the eyewall consisted of an asymmetric inward spiraling band with enhanced convection on the eastern side. The eyewall maintained this semicircular structure and general orientation throughout the remaining 3 hrs of inner-core observation. Surrounding the eyewall at radii between 50-120 km were several developing convective and stratiform rainbands.

Inspection of animated radar imagery revealed that the eyewall contained multiple convective cells (> 30 dBZ with diameters < 10 km) that predominantly formed on the southern side and advected cyclonically around to the eastern and northern sides. Likewise, most rainbands were comprised of many isolated convective cells embedded within

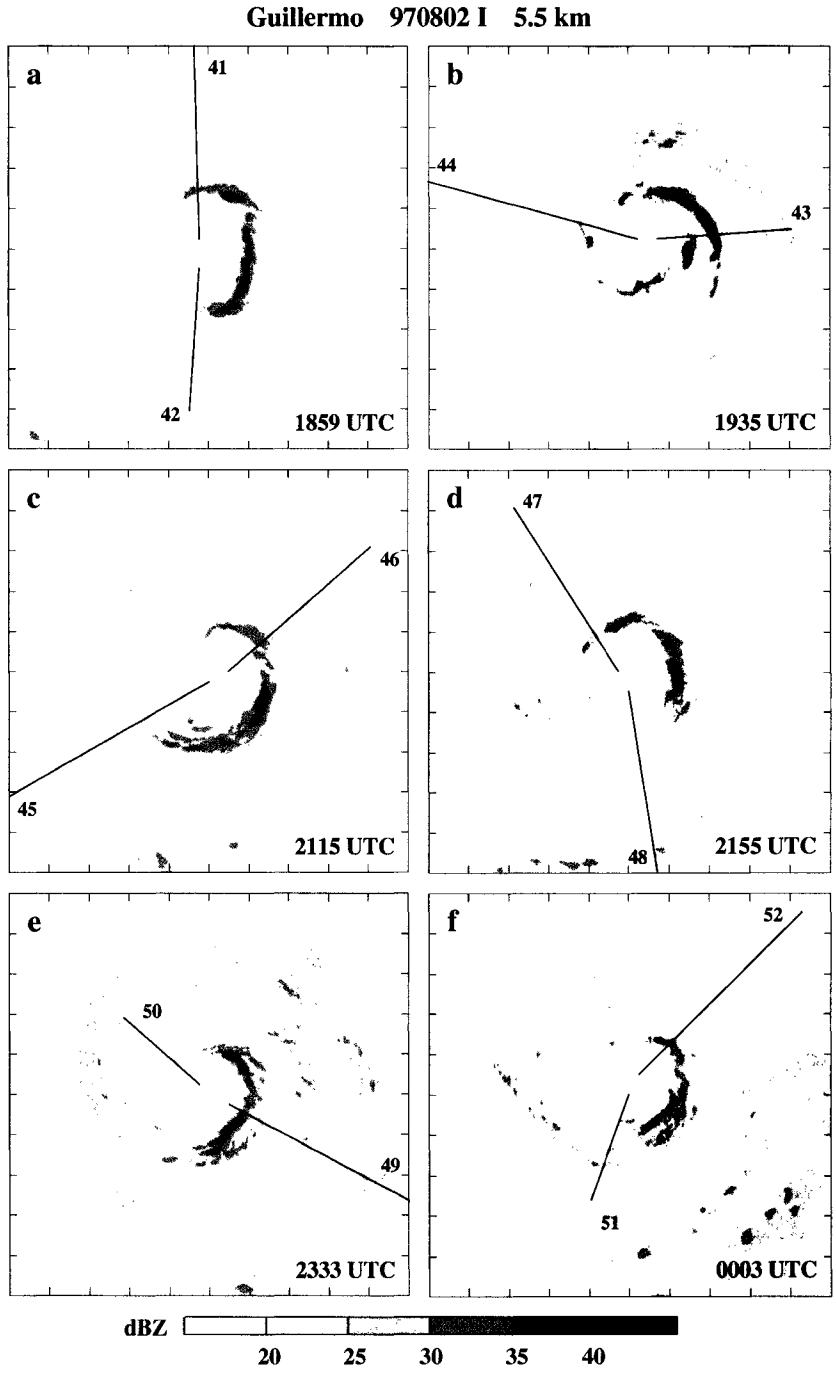


Figure 4.1: Storm-relative radar reflectivity at ~5.5 km altitude for Hurricane Guillermo on 2 August 1997 during each eye penetration at (a) 1859 UTC, (b) 1935 UTC, (c) 2115 UTC, (d) 2155 UTC, (e) 2333 UTC, and (f) 0003 UTC on 3 August. The domain of each panel is 240 km × 240 km and tic marks are shown every 24 km. The solid lines denote the radial legs flown during each eye penetration. Leg number increments denote aircraft heading during each penetration. Note that throughout much of the flight the eyewall was comprised of a persistent wavenumber-one reflectivity field and many transient smaller-scale features.

a stratiform rain area (e.g., the rainband located ~60 km east of the center in Fig. 4.1f). Numerous convective cells were tracked to provide a description of their life cycle. Most eyewall cells (Fig. 4.2) were trackable for ~120° from formation in the southern quadrant to dissipation in the eastern and northern quadrants. Cell lifetimes were typically 10-20 min, which translates to orbital velocities of ~47 m $s^{-1}$ (at 25 km) or ~85% of the azimuthal mean horizontal wind in the 3.0-5.5 km layer. Rainband cells (Fig. 4.3) were trackable for ~30-60° over 20-30 min, and roughly moved with the local azimuthal mean layer wind (25-35 m $s^{-1}$). These cell characteristics are consistent with earlier observations made in Hurricane Frederic (Parrish et al. 1984). While individual convective cells can not be uniquely associated with individual updraft cores, the spatial similarity between convective cells and updrafts cores (core diameters never exceeded 10 km) suggests that such cells may be manifestations of the cores.

It is interesting to note that during the first three eye penetrations a few reflectivity cells > 10 km in diameter were trackable in the eyewall for ~270° over 30-60 min (red cores in Fig. 4.2). These larger cells moved much slower, at ~65% of the azimuthal mean layer wind, which is consistent with expectations for convectively excited vortex Rossby waves (Montgomery and Kallenbach 1997).

Figure 4.4 shows representative flight-level data from the fifth eye penetration between 2316 and 2339 UTC (see Fig. 4.1e). The vertical lines denote convective-scale updraft cores. On the southeast side of the eyewall, the aircraft encountered a ~1.5 m $s^{-1}$ mesoscale updraft upon which two updraft cores and one downdraft core were superimposed. The innermost updraft core exhibited $\overline{w}_c > 3$ m $s^{-1}$ and $\overline{B} > 0.5$ K, which exceed the respective upper 10% values of each distribution discussed in Chapter 3. The outer updraft core was weaker ($\overline{w}_c < 1.5$ m $s^{-1}$) and negatively buoyant ($\overline{B} \sim -0.70$ K), as was the downdraft core ($\overline{B} \sim -0.15$ K). In contrast, the aircraft encountered minimal mesoscale vertical motion, no convective-scale cores, minimal buoyancy (positive or negative), and little cloud or precipitation water content on the northwest side of the eyewall. Interestingly, the equivalent potential temperature ($\theta_e$) and relative vertical vor-

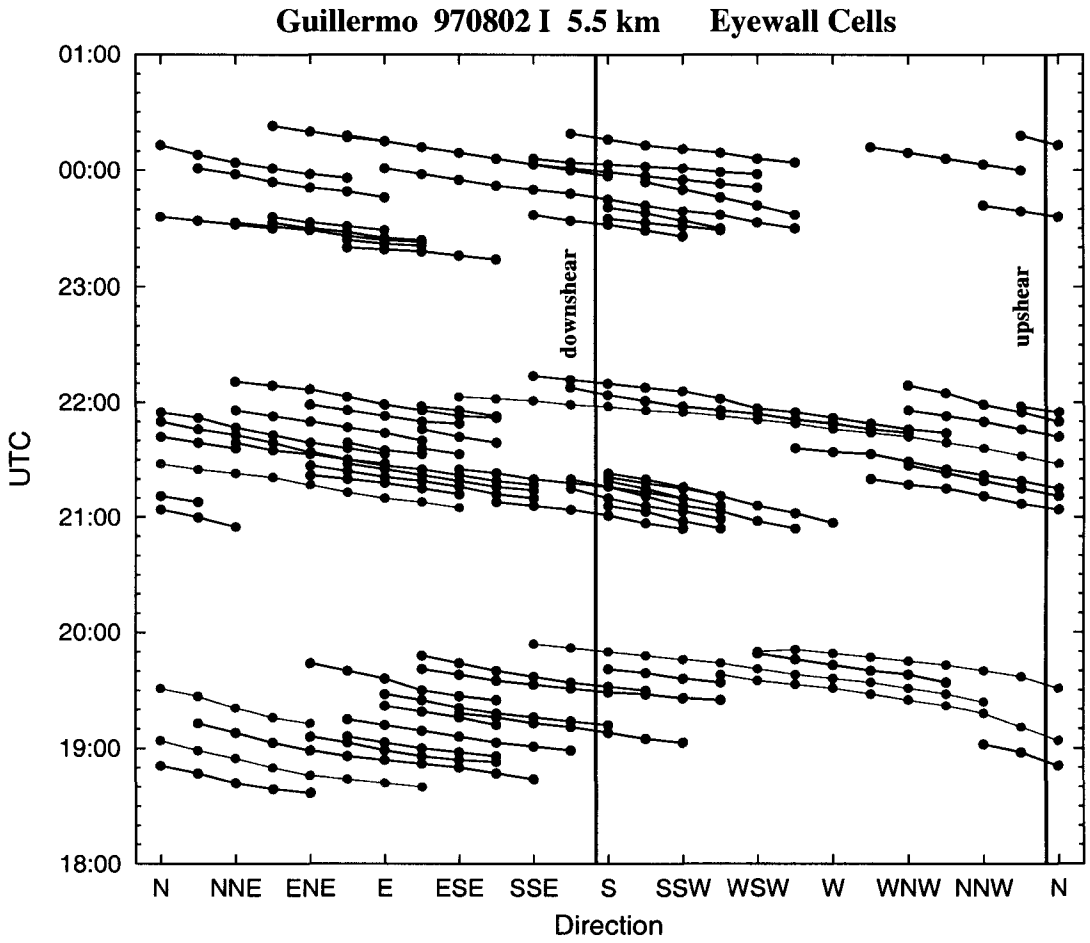


Figure 4.2: Time-azimuth plots of individual radar convective cell locations in Guillermo's eyewall based upon animated LF single-scan radar imagery between 1830 UTC on 2 August and 0030 UTC on 3 August 1997. Time increases upward and cells move from right to left, as they would appear to do from inside the eye. Cells positions shown in red denote the larger, longer-lasting cells. Bold lines denote the upshear and downshear directions.

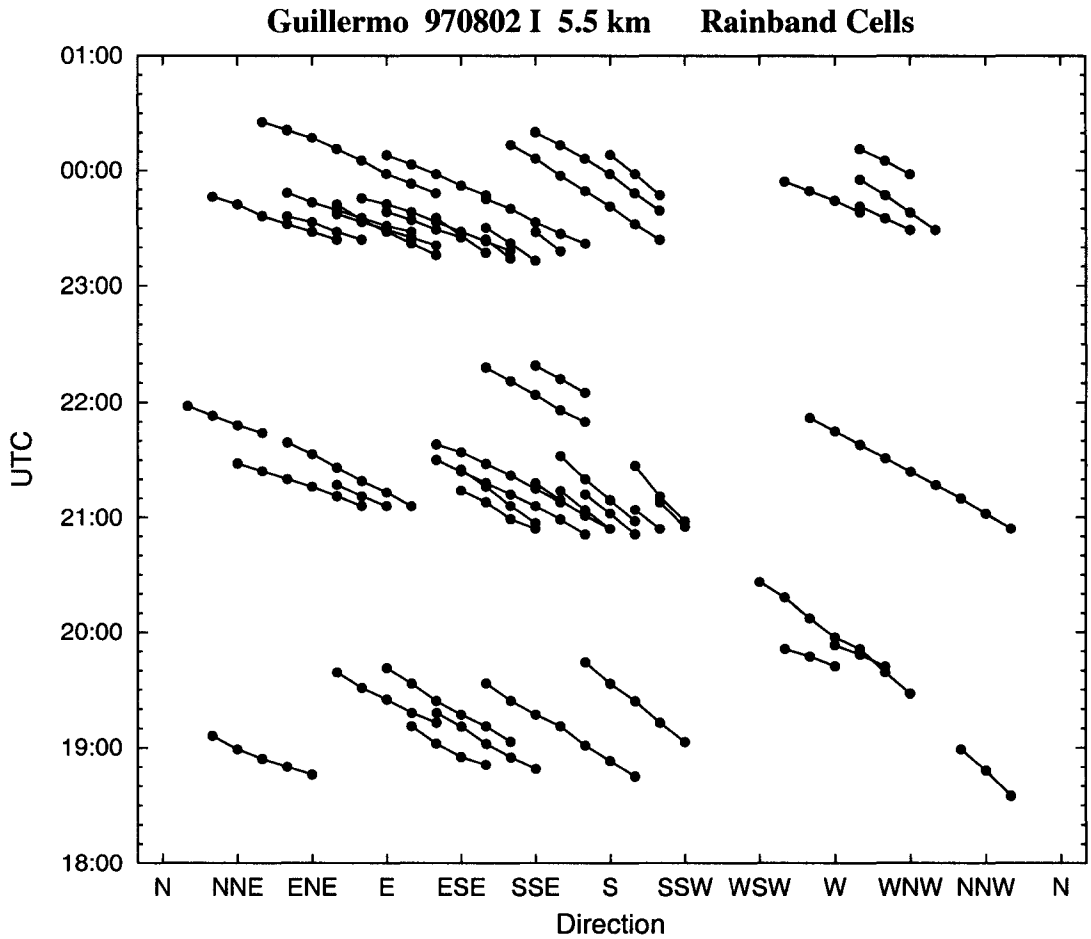


Figure 4.3: As in Fig. 4.2 but for convective cells embedded in rainbands.

ticity ($\zeta$)[1] were much less asymmetric. Both radial legs exhibited $\theta_e$ and $\zeta$ maxima in the eyewall region with depressed values inside the eye. Note that the strong buoyant updraft in the southeast eyewall is collocated with both $\theta_e$ and $\zeta$ maxima. Kossin and Eastin (2001) found that such $\theta_e$ and $\zeta$ radial structure was frequently observed at mid-levels in intensifying hurricanes.

The rainband encountered 90-110 km southeast of the storm center (Fig. 4.4) contained a $\sim$2 m s$^{-1}$ mesoscale updraft upon which three updraft cores and two downdraft cores were superimposed. Each rainband updraft core was positively buoyant ($\overline{B} \sim$ 0.25-0.35 K), and the downdraft cores were negatively buoyant ($\overline{B} \sim -0.10$ K). Elevated values of $\theta_e$ and $\zeta$ were also located within the rainband. Similar characteristics were observed during other rainband penetrations.

Figure 4.5 summarizes the vertical velocity and core buoyancy characteristics along all 12 radial legs flown at 5.5 km. The figure's construction and utility are described here in some detail because similar summary figures are presented for each case study. In each panel, radial leg data were superimposed upon a single-scan horizontal reflectivity field from a representative eye penetration. The upper panel highlights sections of each radial leg in which the mesoscale vertical velocity ($w_m$) exceeded certain appreciable magnitudes (3, 1, and $-1$ m s$^{-1}$). The middle panel depicts the locations of all identified updraft cores stratified by their $\overline{w}_c$ and $\overline{B}$ characteristics. The stratification criteria ($\overline{w}_c > 2$ m s$^{-1}$ and $\overline{B} > 0.25$ K) were designed to isolate updraft cores with appreciable vertical motion or positive buoyancy. Within the context of the statistical distributions presented in Chapter 3, the criteria isolate cores from the upper $\sim$33% of each distribution. The lower panel denotes the locations of downdraft cores with average total vertical velocity ($\overline{w}$) $< -1$ m s$^{-1}$ stratified by their $\overline{B}$ characteristics (either positive or negative). Downdraft cores with $\overline{w} > -1$ m s$^{-1}$ were excluded since they do not contribute significantly to downward

[1]Equivalent potential temperatures were computed following Bolton (1980) and relative vertical vorticity was estimated using a simple difference formula of $\zeta(r) = \partial(rv)/(r\partial r)$ where $v$ is the tangential wind.

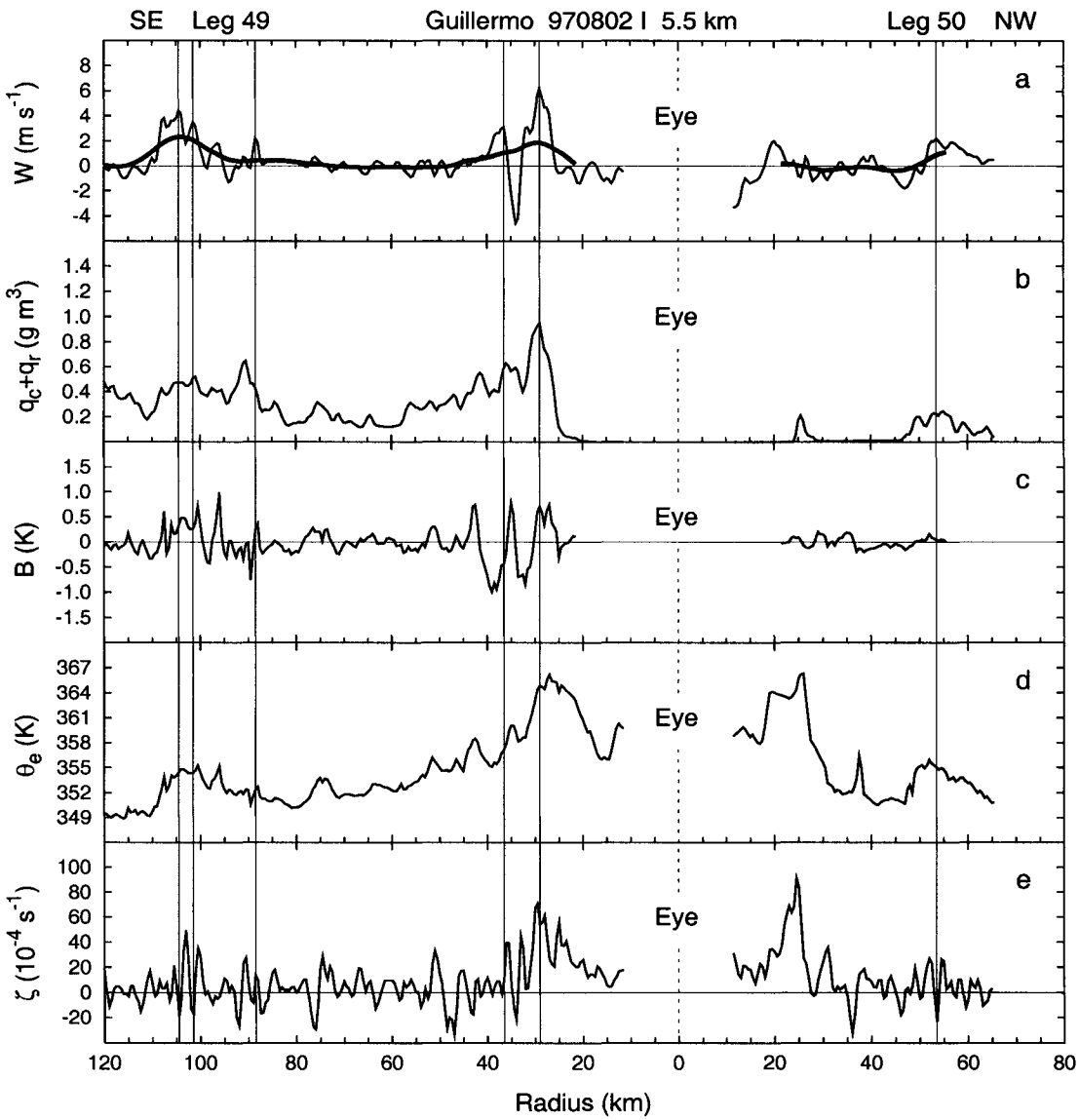


Figure 4.4: Storm-relative radial profiles of (a) total vertical velocity $w$, (b) total liquid water content $q_c$+$q_r$, (c) total buoyancy $B$, (d) equivalent potential temperature $\theta_e$, and (e) relative vertical vorticity $\zeta$ for Hurricane Guillermo during the fifth eye penetration at ~5.5 km altitude between 2316 and 2339 UTC on 2 August 1997. The bold line in (a) denotes the mesoscale vertical velocity $w_m$ estimated through application of a 20 km running Bartlett filter to the $w$ data. Differences between $w$ and $w_m$ define the convective vertical velocity $w_c$ from which updraft and downdraft cores were defined ($|w_c| > 1$ m s$^{-1}$ for at least 0.5 km). Vertical lines denoted identified convective updraft cores.

mass transport (see Chapter 3.3 for further discussion of such cores). The figures are utilized to depict *gross* azimuthal relationships between vertical velocity, buoyancy, and radar reflectivity. Convective-scale features are not directly comparable since the radial leg data was collected over the course of several hours. However, the quasi-steadiness in the mesoscale convective structure during each inner-core observation period should permit comparison of gross features.

Mesoscale updrafts (Fig. 4.5a) in excess of 1 m $s^{-1}$ dominated the eyewall region of each radial leg flown in the western, southern, and eastern quadrants. Mesoscale descent $< -1$ m $s^{-1}$ was found in the northern eyewall. The semi-circular eyewall reflectivity signature was rotated ~60-90° downwind of the mesoscale updraft band, with the mesoscale descent downwind of the reflectivity maximum. Several previous studies (Marks et al. 1992; Franklin et al. 1993; Reasor et al. 2000; Black et al. 2002) have noted similar azimuthal offsets that are consistent with the cyclonic advection of hydrometeors generated by the mesoscale (and convective-scale) updrafts. Appreciable mesoscale ascent was also encountered during several rainband penetrations.

A total of 49 updraft cores (Fig. 4.5b) were encountered at 5.5 km altitude within 120 km of the storm center. The 32 updraft cores in the eyewall region (16-50 km radius annular ring) were evenly distributed about the center with 2-5 cores found along each leg. However, the 6 stronger and more buoyant updraft cores (both $\overline{w}_c > 2$ m $s^{-1}$ and $\overline{B} > 0.25$ K) were superimposed upon mesoscale ascent and collocated with the higher radar reflectivities in the southern and eastern quadrants. Roughly half of the rainband updraft cores (8 of 17) exhibited $\overline{B} > 0.25$ K. All such cores were encountered within rainband segments containing isolated convective cells with reflectivities > 30 dBZ. Clearly, the azimuthal distribution of buoyant updraft cores was highly asymmetric, yet well correlated with regions of enhanced convection.

Table 4.1 summarizes eyewall updraft core percent area occupied and percent total (convective and mesoscale) upward mass transport accomplished as a function of core characteristics. Updraft cores covered ~10% of the eyewall area and accomplished ~50%

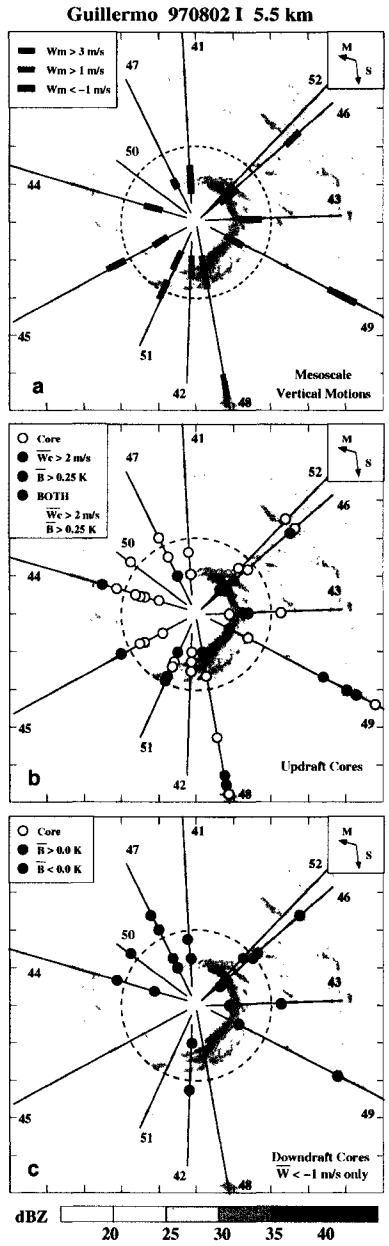


Figure 4.5: Summary of flight-level vertical velocity and core buoyancy for Hurricane Guillermo between 1800 UTC on 2 August and 0100 UTC on 3 August 1997 at ~5.5 km altitude. (a) Sections of each radial leg in which the mesoscale vertical velocity $w_m$ exceeded certain magnitudes. (b) Locations of convective updraft cores stratified by their average convective vertical velocity $\overline{w}_c$ and average total buoyancy $\overline{B}$ characteristics. (c) Locations of convective downdraft cores with average total vertical velocity $\overline{w} < -1$ m s$^{-1}$ stratified by their $\overline{B}$ characteristics. The radial leg data in each panel is superimposed upon a representative storm-relative radar reflectivity field observed at 2333 UTC during the fifth eye penetration. The domain of each panel is 240 km × 240 km and tic marks are shown every 24 km. The storm motion (M, blue) and vertical wind shear (S, red) vectors are shown in the upper right corner. Dashed circles denote the approximate separation radius between the eyewall and rainband regions.

of the upward mass transport. However, the six strong and more buoyant cores occupied ~2% of the same area and accomplished ~25% of the total mass transport. The more buoyant rainband updraft cores (Table 4.2) occupied ~3% of the rainband region (51-120 km radius annular ring) but accomplished ~30% of the upward mass transport. Therefore, such few cores significantly contribute to the total upward mass transport despite minimal areal coverage.

Table 4.1: Summary of eyewall updraft core statistics for each hurricane case study and all hurricanes examined. Updraft cores are stratified by average convective vertical velocity ($\overline{w}_c$), and average total buoyancy ($\overline{B}$). Core statistics include number (N), percent of total area occupied, and percent of total upward mass transport accomplished. The eyewall region was located between r = 15-45 km on average.

| | Flight | | | | | Eyewall Region | | |
|---|---|---|---|---|---|---|---|---|
| Storm | Date yr/mo/day | ID | Altitude (km) | Number of Legs | Updraft Cores | N | % of Area | % of Total Up MT |
| Guillermo | 97/08/02 | I | 5.5 | 12 | All | 32 | 10.4 | 49 |
| | | | | | $\overline{B} > 0.25$ K | 9 | 4.0 | 31 |
| | | | | | $\overline{w}_c > 2$ m s$^{-1}$ | 9 | 4.9 | 33 |
| | | | | | Both $\overline{B} > 0.25$ K $\overline{w}_c > 2$ m s$^{-1}$ | 6 | 2.3 | 24 |
| | 97/08/03 | I | 5.5 | 12 | All | 41 | 18.3 | 62 |
| | | | | | $\overline{B} > 0.25$ K | 17 | 9.8 | 42 |
| | | | | | $\overline{w}_c > 2$ m s$^{-1}$ | 15 | 9.2 | 45 |
| | | | | | Both $\overline{B} > 0.25$ K $\overline{w}_c > 2$ m s$^{-1}$ | 10 | 6.1 | 36 |
| Edouard | 96/08/27 | I | 3.0 | 14 | All | 33 | 11.8 | 56 |
| | | | | | $\overline{B} > 0.25$ K | 17 | 6.3 | 24 |
| | | | | | $\overline{w}_c > 2$ m s$^{-1}$ | 14 | 5.7 | 42 |
| | | | | | Both $\overline{B} > 0.25$ K $\overline{w}_c > 2$ m s$^{-1}$ | 6 | 2.7 | 21 |
| Georges | 98/09/19 | H | 4.2 | 4 | All | 6 | 10.0 | 54 |
| | | | | | $\overline{B} > 0.25$ K | 2 | 3.1 | 22 |
| | | | | | $\overline{w}_c > 2$ m s$^{-1}$ | 5 | 9.8 | 53 |
| | | | | | Both $\overline{B} > 0.25$ K $\overline{w}_c > 2$ m s$^{-1}$ | 2 | 3.1 | 22 |
| All Intense Hurricane Cases | | | | 175 | All | 351 | 9.9 | 64 |
| | | | | | $\overline{B} > 0.25$ K | 120 | 3.7 | 25 |
| | | | | | $\overline{w}_c > 2$ m s$^{-1}$ | 107 | 5.1 | 42 |
| | | | | | Both $\overline{B} > 0.25$ K $\overline{w}_c > 2$ m s$^{-1}$ | 51 | 2.1 | 20 |

Table 4.2: As in Table 4.1 but for rainband updraft cores. The rainband region was located between r = 45-115 km on average.

| | Flight | | | | | Rainband Region | | |
|---|---|---|---|---|---|---|---|---|
| Storm | Date yr/mo/day | ID | Altitude (km) | Number of Legs | Updraft Cores | N | % of Area | % of Total Up MT |
| Guillermo | 97/08/02 | I | 5.5 | 12 | All | 17 | 5.3 | 40 |
| | | | | | $\overline{B} > 0.25$ K | 8 | 3.2 | 28 |
| | | | | | $\overline{w}_c > 2$ m s$^{-1}$ | 2 | 1.0 | 14 |
| | | | | | Both $\overline{B} > 0.25$ K $\overline{w}_c > 2$ m s$^{-1}$ | 2 | 1.0 | 14 |
| | 97/08/03 | I | 5.5 | 12 | All | 30 | 5.9 | 46 |
| | | | | | $\overline{B} > 0.25$ K | 13 | 2.6 | 28 |
| | | | | | $\overline{w}_c > 2$ m s$^{-1}$ | 6 | 2.0 | 22 |
| | | | | | Both $\overline{B} > 0.25$ K $\overline{w}_c > 2$ m s$^{-1}$ | 5 | 1.8 | 18 |
| Edouard | 96/08/27 | I | 3.0 | 14 | All | 31 | 4.3 | 65 |
| | | | | | $\overline{B} > 0.25$ K | 17 | 2.2 | 38 |
| | | | | | $\overline{w}_c > 2$ m s$^{-1}$ | 4 | 0.4 | 22 |
| | | | | | Both $\overline{B} > 0.25$ K $\overline{w}_c > 2$ m s$^{-1}$ | 3 | 0.3 | 16 |
| Georges | 98/09/19 | H | 4.2 | 4 | All | 11 | 6.7 | 41 |
| | | | | | $\overline{B} > 0.25$ K | 6 | 5.8 | 30 |
| | | | | | $\overline{w}_c > 2$ m s$^{-1}$ | 2 | 0.8 | 13 |
| | | | | | Both $\overline{B} > 0.25$ K $\overline{w}_c > 2$ m s$^{-1}$ | 2 | 0.8 | 13 |
| All Intense Hurricane Cases | | | | 175 | All | 269 | 2.9 | 51 |
| | | | | | $\overline{B} > 0.25$ K | 125 | 1.6 | 27 |
| | | | | | $\overline{w}_c > 2$ m s$^{-1}$ | 40 | 0.9 | 20 |
| | | | | | Both $\overline{B} > 0.25$ K $\overline{w}_c > 2$ m s$^{-1}$ | 27 | 0.6 | 15 |

A total of 21 downdraft cores with $\overline{w} < -1$ m s$^{-1}$ were encountered within 120 km of the storm center (Fig. 4.5c). The majority of such eyewall downdraft cores (10 of 12) were found in the eastern and northern quadrants either collocated with or downwind of reflectivity maxima. Eyewall cores in the eastern (northern) quadrant tended to exhibit positive (negative) total buoyancy, while most rainband downdraft cores (7 of 9) were negatively buoyant. Of all the downdrafts with $\overline{B} < 0.0$ K, the majority (8 of 12) exhibited $\overline{TB} < -0.25$ K and $\overline{WL} > -0.10$ K in the presence of liquid water, suggesting that the negative $\overline{B}$ were supported primarily by hydrometeor evaporation.

### 4.2 Hurricane Guillermo on 03 August 1997

The two NOAA WP-3D aircraft returned to Hurricane Guillermo on the following day and observed the inner core between 1900 on 3 August and 0100 UTC on 4 August 1997. Guillermo continued to move westward at 5.5 m s$^{-1}$ over SSTs > 29°C and under the influence of moderate northerly vertical shear. The storm's intensity was relatively steady-state during the inner-core observation period, but intensification from the day before was evident as maximum observed flight-level winds at 3.0 km altitude had increased to 71 m s$^{-1}$ and the MSLP had dropped to 923 mb. All quadrants were well sampled by each aircraft as the lower aircraft (H) made 10 eye penetrations at 3.0 km altitude, and the upper aircraft (I) made 6 eye penetrations at 5.5 km altitude. Analysis of convective core buoyancy characteristics was again limited to the 12 radial legs at 5.5 km.

Guillermo's radar reflectivity structure on 3 August was strikingly similar to the structure observed on 2 August. The single-scan LF radar reflectivity fields obtained during each eye penetration at 5.5 km (Fig. 4.6) depict an asymmetric eyewall at 25 km radius with enhanced convection in the southern and eastern quadrants. This wavenumber-one pattern of high reflectivity remained relatively fixed with respect to the storm center during the 6 hr observation period. The convective-scale reflectivity structure, however, exhibited much variability from penetration to penetration. Surrounding the eyewall at radii between 45-120 km were several inward spiraling rainbands. Isolated convective

cells tended to dominate the upwind portion of each rainband, while downwind portions exhibited more stratiform precipitation.

Convective cell tracking in the animated radar imagery yielded results similar to those of the day before. The wavenumber-one eyewall structure contained multiple convective-scale cells that repeatedly formed in the southern quadrant and rotated 90-120° around the eyewall to the eastern and northern quadrants before dissipation (Fig. 4.7). Cell lifetimes were again 10-20 min, resulting in orbital velocities of ~50 m $s^{-1}$ that are equivalent to ~83% of the local azimuthal mean horizontal wind in the 3.0-5.5 km layer. A few larger cells were trackable for 30-40 min, or over 180° around the eyewall. These longer-lived cells moved at ~60% of the azimuthal mean layer wind. Rainband convective cells (Fig. 4.8) were trackable for 10-20 min and moved approximately with the local azimuthal mean layer wind.

Figure 4.9 shows flight-level data from the first eye penetration between 1855 and 1923 UTC (see Fig 4.6a). On the southern side of the eyewall, the aircraft encountered a strong mesoscale updraft > 3 m $s^{-1}$ and two convective-scale updraft cores. The innermost updraft core exhibited $\overline{w}_c > 4$ m $s^{-1}$, $\overline{B} > 0.4$ K, and was superimposed upon the mesoscale updraft maximum. The outer eyewall updraft core (at 36 km radius) was weaker ($\overline{w}_c <$ 1.5 m $s^{-1}$) but equally buoyant ($\overline{B} \sim 0.5$ K). On the northern side of the eyewall, the aircraft encountered minimal mesoscale vertical motion, little cloud or precipitation water content, two strong downdraft cores ($\overline{w}_c < -2$ m $s^{-1}$), and four weak updraft cores ($\overline{w}_c$ < 2 m $s^{-1}$). The inner downdraft core (at 25 km radius) contained ~0.15 g $m^{-3}$ of liquid water and was negatively buoyant, while the outer downdraft core (at 38 km) contained < 0.05 g $m^{-3}$ of liquid water and was positively buoyant. Of the four updraft cores, only the inner two exhibited positive buoyancy ($\overline{B} < 0.3$ K). The $\theta_e$ and $\zeta$ structures were, again, much less asymmetric with maxima in the eyewall and depressed values inside the eye. Thus, the north-south radial structure observed during the first eye penetration was qualitatively similar to the northwest-southeast structure observed ~20 hr prior on 2 August at the same altitude (Fig. 4.4).

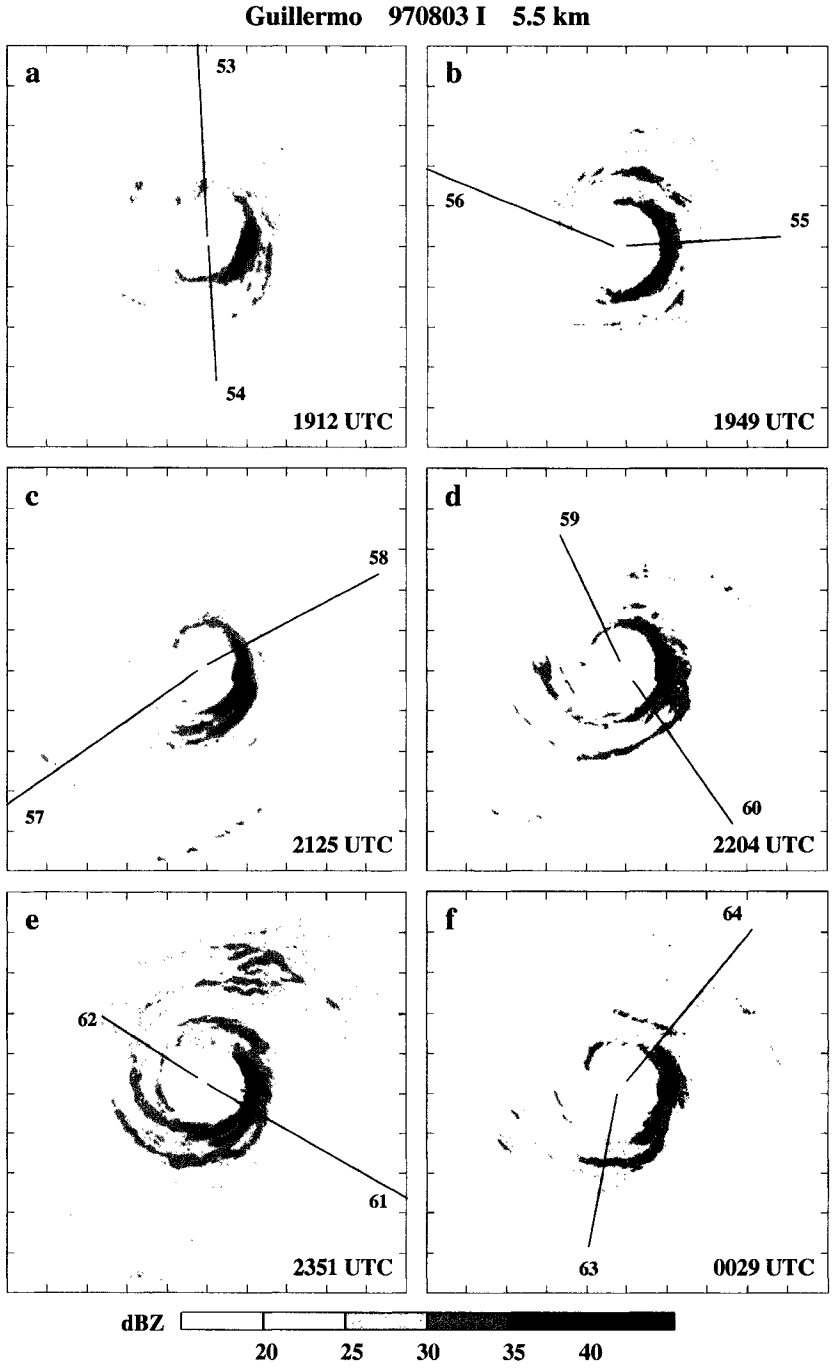


Figure 4.6: As in Fig. 4.1 but on 3 August at (a) 1912 UTC, (b) 1949 UTC, (c) 2125 UTC, (d) 2204 UTC, (e) 2351 UTC, and (f) 0029 UTC on 4 August.

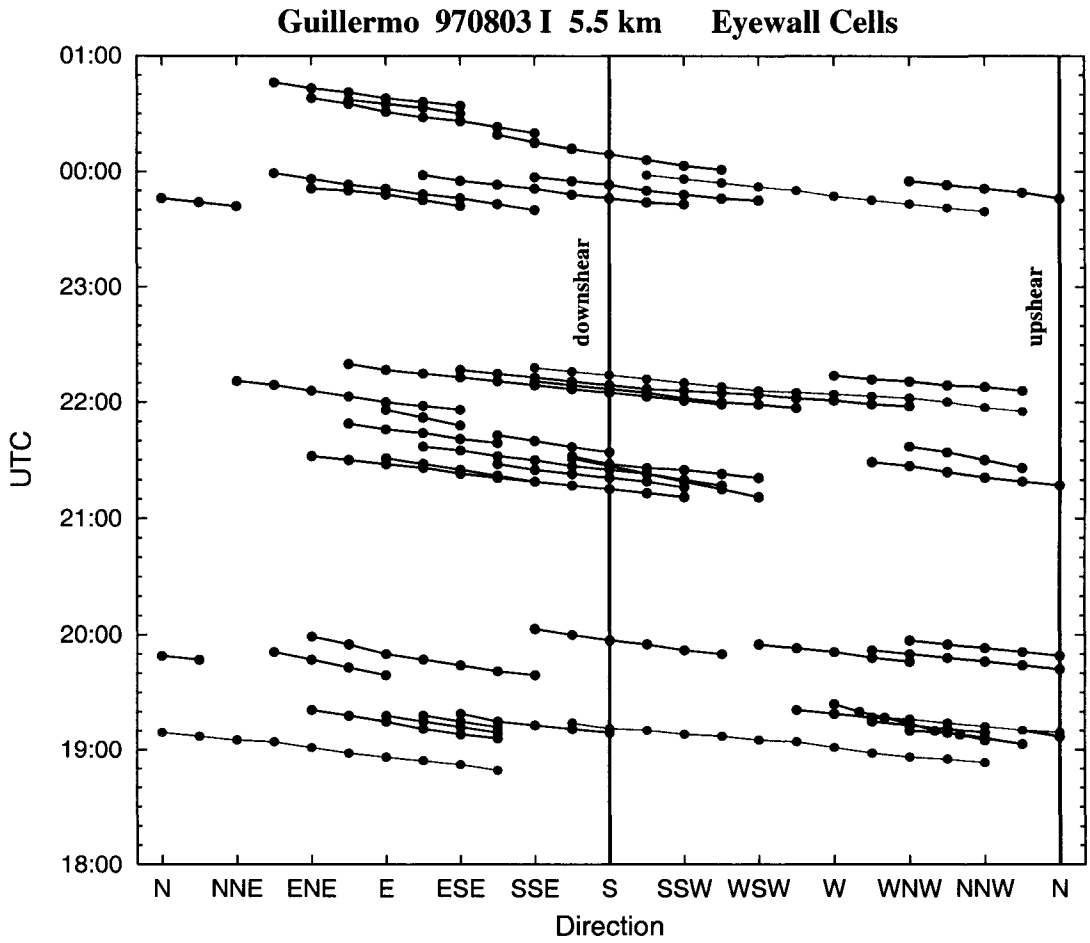


Figure 4.7: As in Figure 4.2 but between 1830 UTC on 3 August and 0100 UTC on 4 August 1997.

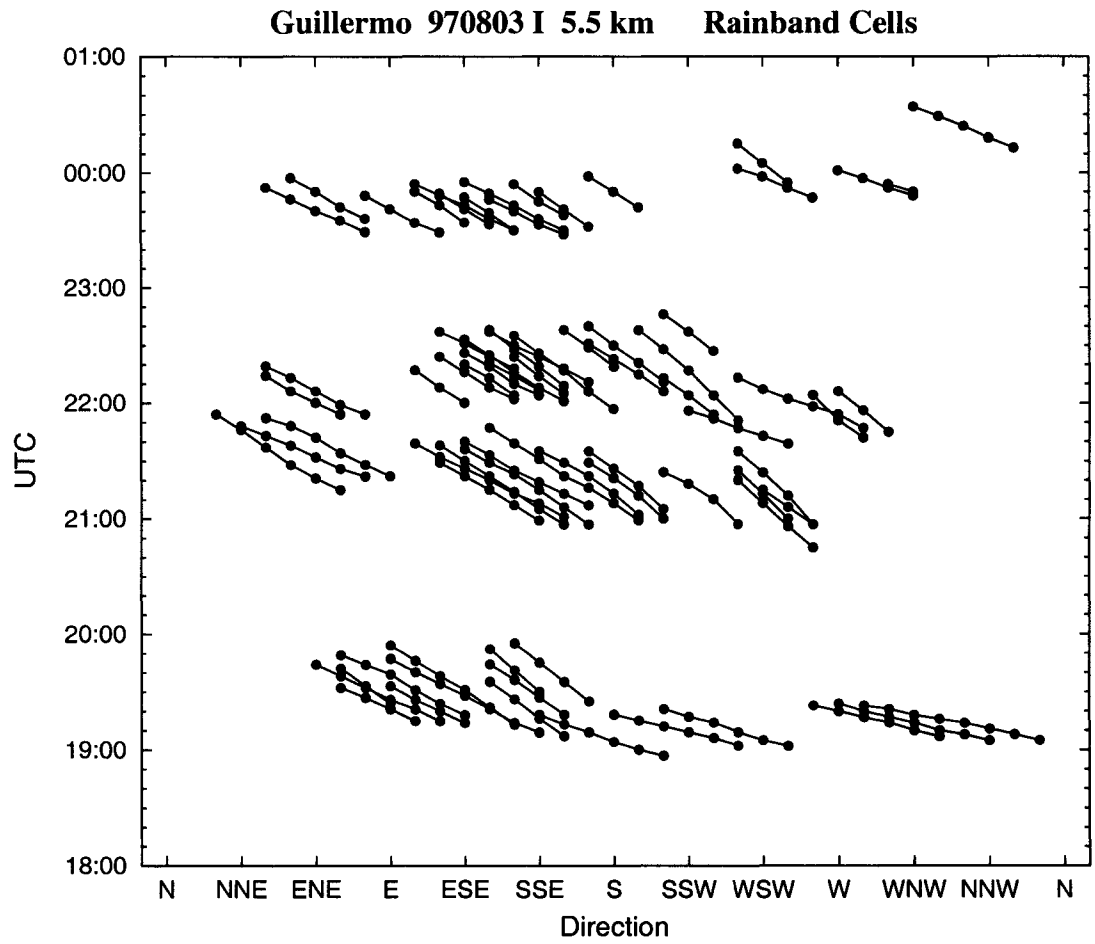


Figure 4.8: As in Fig. 4.2 but for convective cells embedded in rainbands between 1830 UTC on 3 August and 0100 UTC on 4 August 1997.

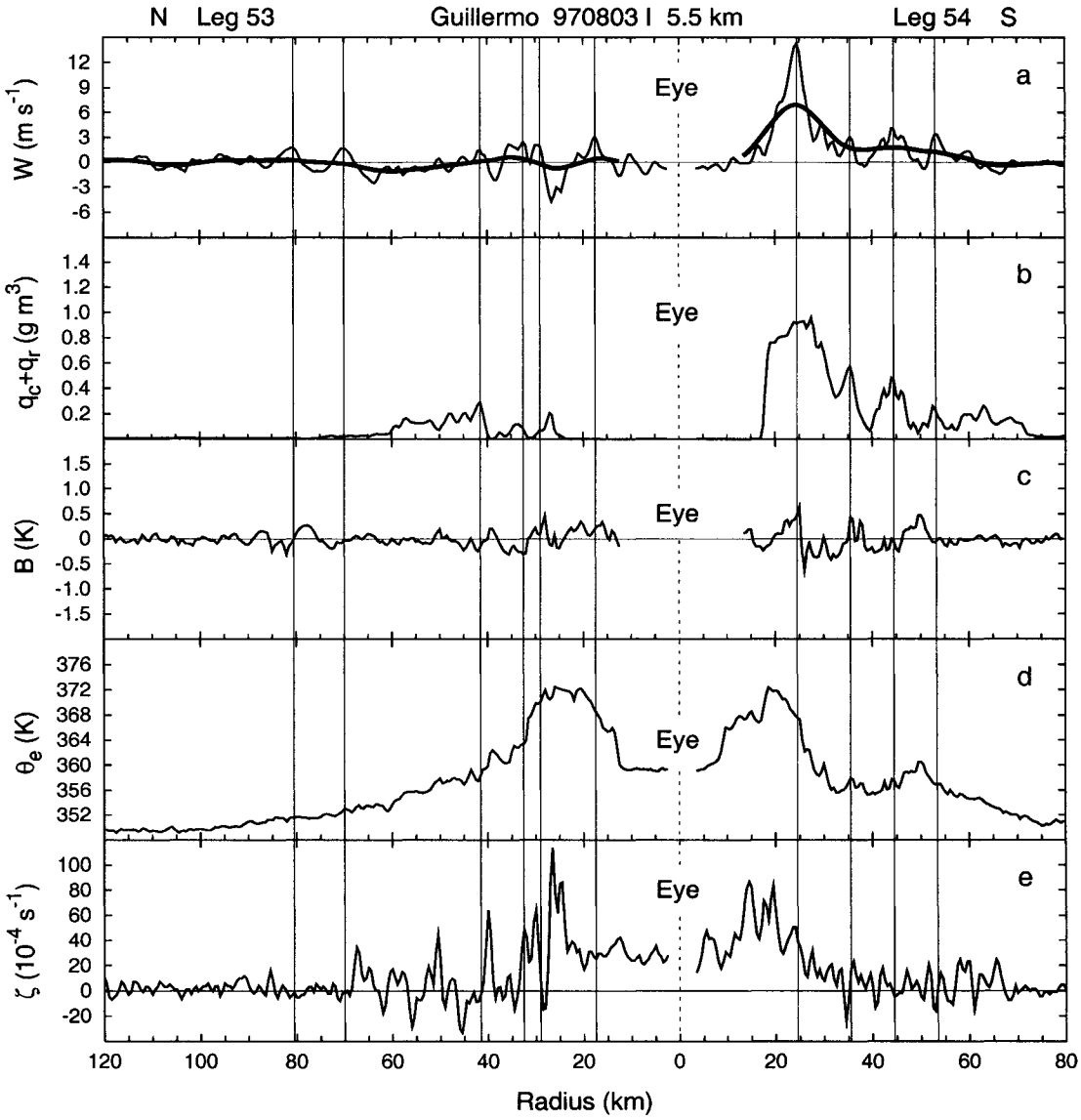


Figure 4.9: As in Fig. 4.4 but during the first eye penetration between 1855 and 1923 UTC on 3 August.

This general wavenumber-one pattern in reflectivity and vertical velocity characteristics persisted during the 6 hr observation period, but the $\theta_e$ and $\zeta$ radial profiles underwent significant structural changes. Figure 4.10 shows the flight-level data from the fifth eye penetration between 2333 and 2359 UTC (see Fig 4.6e). As before, the aircraft encountered a strong mesoscale updraft and two buoyant updraft cores on the southeast side of the eyewall, while a mesoscale downdraft and several relatively weak and near-neutral ($|\overline{B}|$ $< 0.1$ K) convective cores were encountered on the northwest side. However, in contrast to the first eye penetration, the $\theta_e$ and $\zeta$ profiles exhibited pronounced mesoscale maxima in the eye, rather than in the eyewall. Kossin and Eastin (2001) found that such dramatic transitions in the $\theta_e$ and $\zeta$ radial structure, which they attributed to horizontal mixing associated with vortex-Rossby waves and mesovorticies, frequently occurred at maximum intensity (i.e., soon after a period of intensification). The timing of the dramatic structural changes is consistent; rapid intensification ceased just prior to the 3 August inner core observation period.

A total of 9 updraft cores and 5 downdraft cores were encountered in the rainband region during the first and fifth eye penetrations (beyond 45 km radius in Figs. 4.9 and 4.10). The cores located south and east of the storm center (along legs 54 and 61) were superimposed upon mesoscale updrafts $> 1$ m s$^{-1}$ and embedded within rainbands containing local $\theta_e$ and $\zeta$ maxima. The majority of such updraft cores (5 of 7) exhibited positive buoyancy ($\overline{B} \sim 0.2$-$0.6$ K), and the lone downdraft was negatively buoyant. Note, however, that the 2 updraft cores and 3 downdraft cores located north of the storm center (along leg 53 in Fig. 4.9) were encountered in clear air. The radial spacing of the cores comprise an oscillatory pattern in $w_c$ which is 90° out-of-phase with a spatially similar (although less coherent) oscillatory pattern in $B$ (that is dominated by temperature perturbations). Such radial structure is consistent with the structure of an inward propagating internal-gravity wave within a stably stratified environment (e.g., Holton 1992), not deep convection.

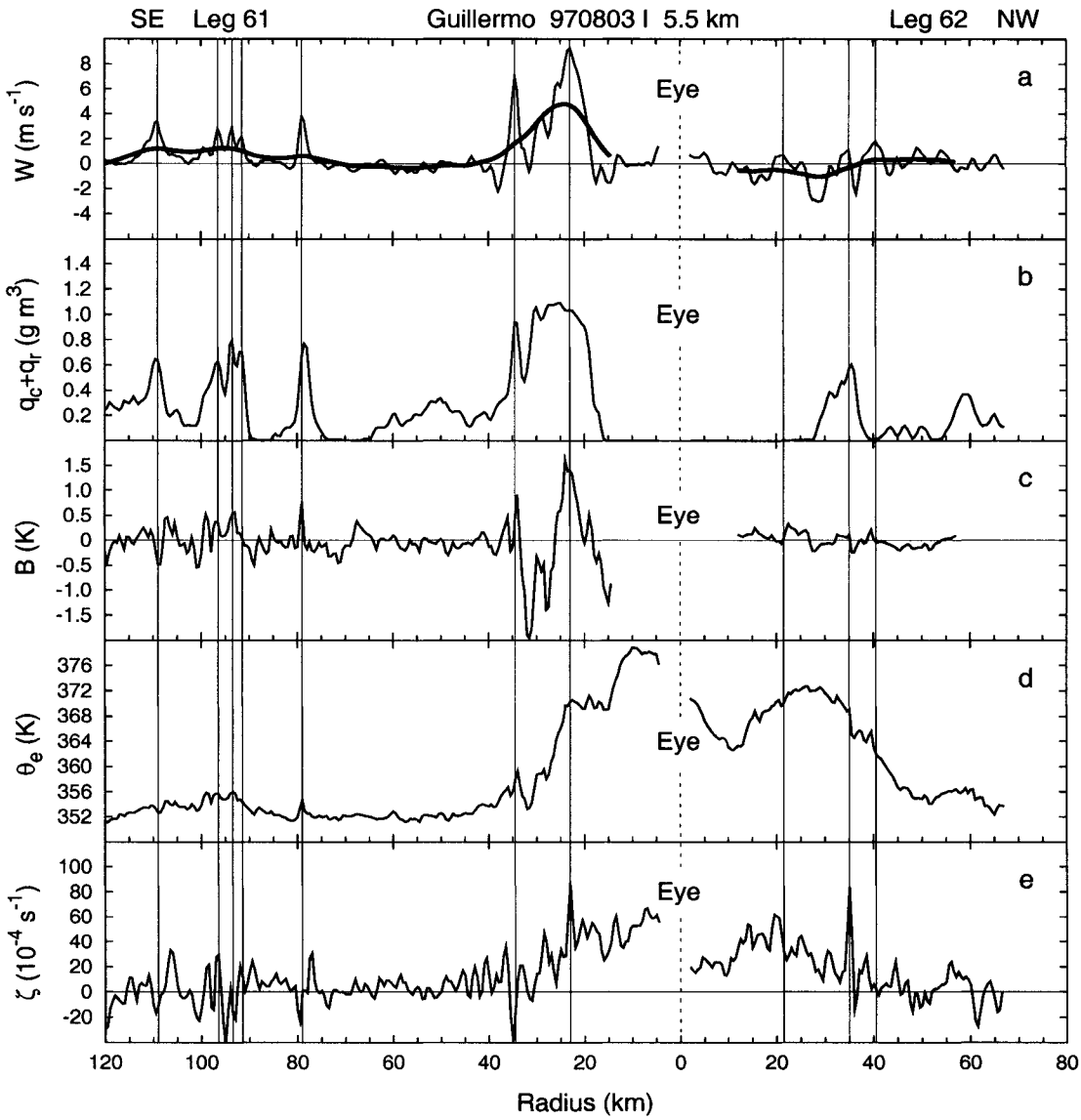


Figure 4.10: As in Fig. 4.4 but during the fifth eye penetration between 2333 and 2359 UTC on 3 August.

Figure 4.11 summarizes the vertical velocity and core buoyancy characteristics for all 12 radial legs at 5.5 km. Many characteristics evident on 3 August are strikingly similar to those observed on 2 August. Mesoscale updrafts (Fig. 4.11a) in excess of 3 m $s^{-1}$ dominated the eyewall's southern quadrant, while mesoscale downdrafts (of which a few exceeded $-1$ m $s^{-1}$) were typically found in the northern quadrant. Again, the strong mesoscale updrafts were located ~90° upwind of the reflectivity maximum (in the eastern quadrant), which was upwind of the mesoscale downdrafts. No appreciable mesoscale downdrafts were encountered during rainband penetrations, but several mesoscale updrafts were.

A total of 71 updraft cores (Fig. 4.11b) were encountered within 120 km of the storm center. The 41 eyewall updraft cores (located within the 14-45 km radius annular ring) were again evenly distributed about the center with 2-5 cores found along each leg. Updraft cores with $\overline{B} > 0.25$ K were found in all quadrants, but the 10 stronger and more buoyant updraft cores were limited to the southern and eastern quadrants. These few cores occupied ~6% of the total eyewall area but accomplished ~35% of the total upward mass transport (see Table 4.1). As before, the majority of rainband updraft cores (16 of 24) exhibited $\overline{B} > 0.25$ K. These cores were typically encountered within more cellular rainband segments and accomplished a considerable fraction (~35%) of the total upward mass transport (see Table 4.2), despite covering < 2% of the total rainband area (46-105 km radius annular ring).

A total of 33 downdraft cores with $\overline{w} < -1$ m $s^{-1}$ were encountered (Fig. 4.11c). Of the 20 cores with negative total buoyancy, over 70% exhibited $\overline{TB} < -0.25$ K and $\overline{WL} > -0.10$ K in the presence of liquid water. In the eyewall region, the majority of downdraft cores (18 of 26) were located in the northern semicircle, downwind of the reflectivity maxima.

## 4.3 Hurricane Edouard on 27 August 1996

The inner core of Hurricane Edouard was observed by the two NOAA WP-3D aircraft between 1800 and 2400 UTC on 27 August 1996. Details concerning the history of Edouard

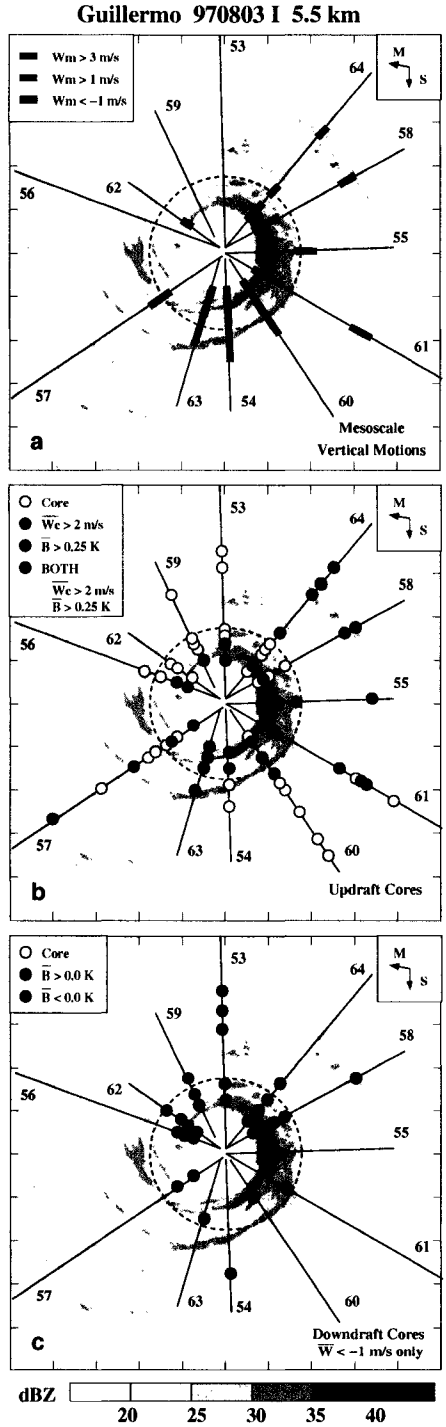


Figure 4.11: As in Fig. 4.5 but between 1900 UTC on 3 August and 0100 UTC on 4 August. The representative storm-relative radar reflectivity field was observed at 2204 UTC during the fourth eye penetration.

are given by Pasch and Avila (1999). During this period, Edouard was located 450 km northeast of the island of St. Martin and was moving at 5.8 m $s^{-1}$ toward the west-northwest over 27°-28°C SSTs. The storm was under the influence of moderate west-southwesterly vertical shear. Maximum observed flight-level winds were 65 m $s^{-1}$ at 3.0 km altitude, and the MSLP was 941 mb. Edouard's intensity remained relatively steady while the aircraft observed the inner core. Both aircraft made 7 eye penetrations as all quadrants were well sampled. The lower aircraft (I) flew penetrations at 3.0 km altitude, and the upper aircraft (H) flew at 4.2 km. Radiometric temperature data was only available from the lower aircraft, and thus analysis of convective core buoyancy characteristics was limited to the 14 radial legs at 3.0 km.

Edouard's inner-core reflectivity structure and evolution exhibited many of the same general characteristics that were observed each day in Guillermo. The single-scan LF reflectivity fields from each eye penetration at 3.0 km altitude (Fig. 4.12) depict an asymmetric eyewall at ~30 km radius with enhanced convection (> 30 dBZ) in the northern and western quadrants. This semicircular high-reflectivity structure persisted and remained relatively fixed throughout the flight. Convective-scale reflectivity structures, however, evolved (i.e., developed and dissipated) and moved cyclonically around the eyewall. Several inward spiraling rainbands surrounded the eyewall at radii beyond ~45 km. Rainbands to the south and east tended to be more cellular, while bands to the west were more stratiform. Convective cells were not tracked in animated radar imagery for this case.

The vertical velocity and core buoyancy characteristics at 3.0 km altitude in Edouard (Fig. 4.13) were also qualitatively similar to those at 5.5 km altitude in Guillermo. Mesoscale updrafts in excess of 1 m $s^{-1}$ were observed in all quadrants of the eyewall except the southern (Fig. 4.13a), where weak mesoscale descent dominated. The strongest mesoscale updrafts (> 3 m $s^{-1}$) were located in the northern quadrant, or in the upwind portion of the semicircular high-reflectivity structure. Appreciable mesoscale updrafts were also encountered during several rainband penetrations.

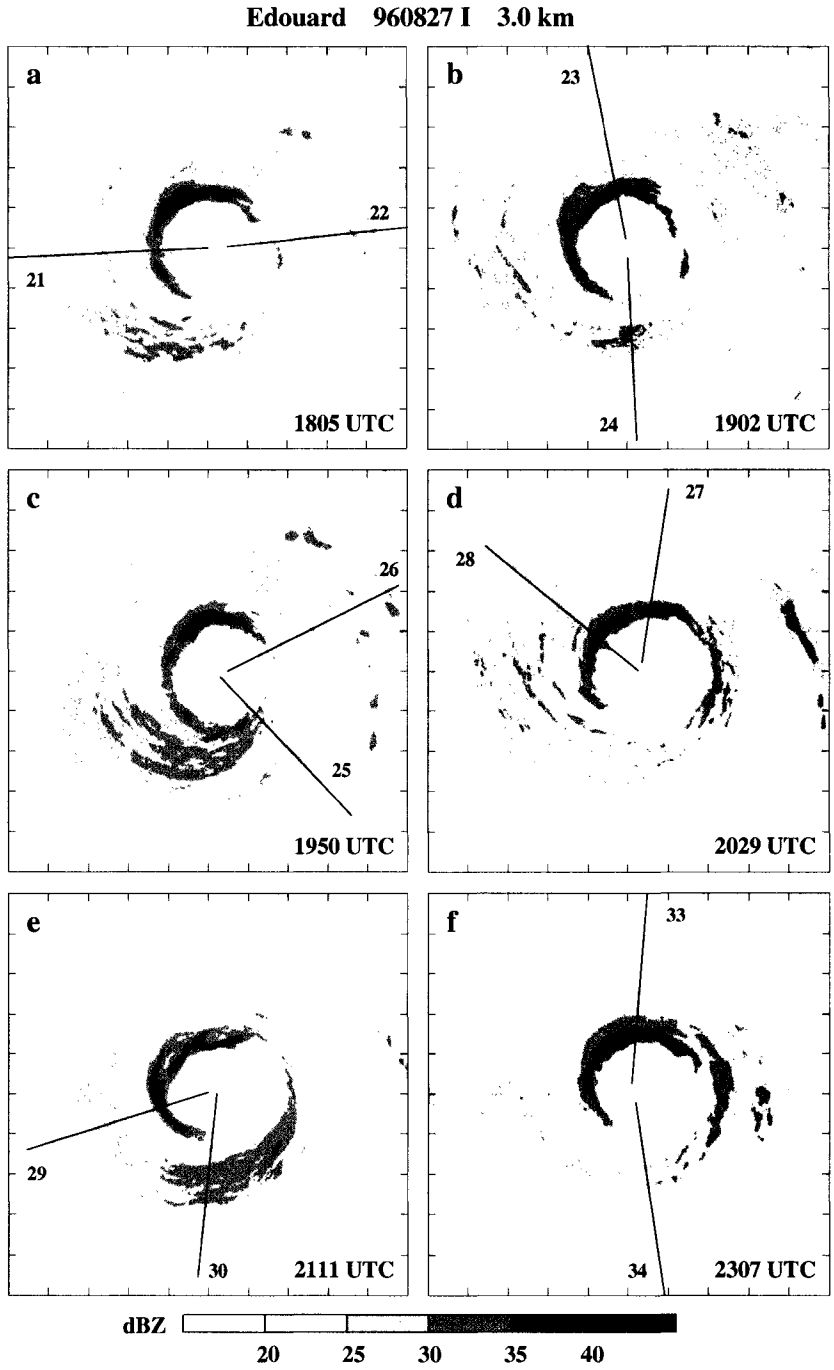


Figure 4.12: As in Fig. 4.1 but for Hurricane Edouard on 27 August 1996 at (a) 1805 UTC, (b) 1902 UTC, (c) 1950 UTC, (d) 2029 UTC, (e) 2111 UTC, and (f) 2307 UTC.

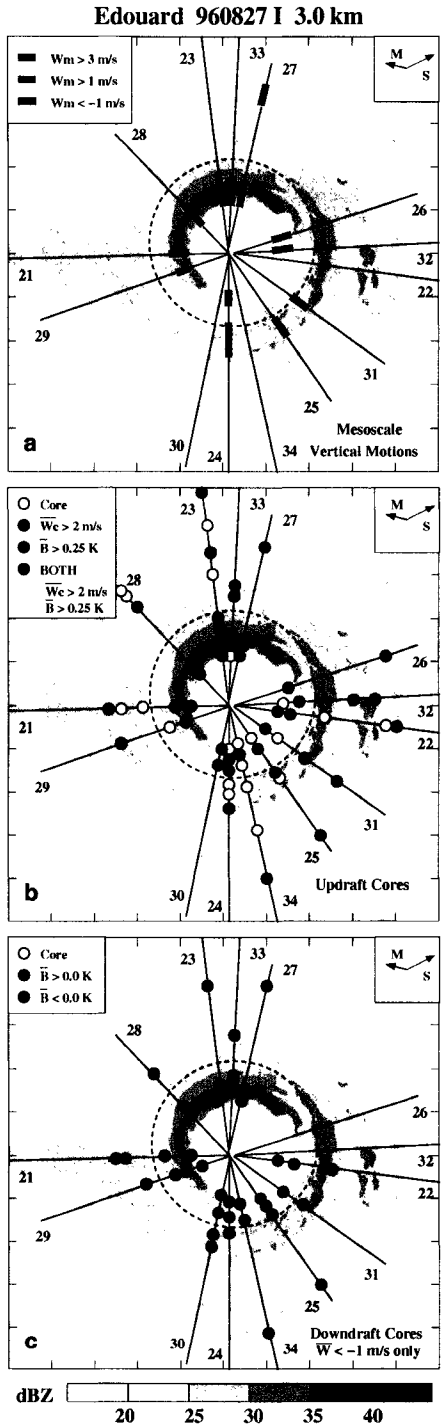


Figure 4.13: As in Fig. 4.5 but for Hurricane Edouard between 1800 and 2400 UTC on 27 August 1996 at ~3.0 km altitude. The representative storm-relative radar reflectivity field was observed at 2307 UTC during the seventh eye penetration.

A total of 64 updraft cores (Fig. 4.13b) were encountered within 120 km of Edouard's circulation center (which was closer to the southwest portion of the eyewall). The 33 updraft cores in the eyewall region (~13-45 km radius annular ring) were evenly distributed about the center, but the stronger and more buoyant updraft cores were found only in the eastern and northern quadrants. These few cores occupied < 3% of the total eyewall area, but accomplished ~20% of the total upward mass transport (Table 4.1). Several strong updraft cores were located in the western and southern portions of the eyewall, but all of these cores were either near neutral or negatively buoyant (i.e., $\overline{B} < 0.1$ K). Interestingly, the southern portion of the eyewall contained a few updraft cores with $\overline{B} > 0.25$ K that were superimposed upon weak mesoscale descent. The majority of rainband updraft cores (17 of 31) exhibited $\overline{B} > 0.25$ K, and these cores tended to reside within more cellular rainband segments.

A total of 36 downdraft cores with $\overline{w} < -1$ m s$^{-1}$ were encountered within the inner core (Fig. 4.13c). The majority of the eyewall downdraft cores (15 of 22) were located in the eastern and southern portions of the eyewall, downwind of the reflectivity maximum. Cores in the northern (southern) portions of the eyewall tended to exhibit (negative) positive buoyancy. The majority of rainband downdraft cores (9 of 14) were negatively buoyant.

### 4.4 Hurricane Georges on 19 September 1998

The inner core of Hurricane Georges was observed by the two NOAA WP-3D aircraft between 1900 UTC on 19 September and 0100 UTC on 20 September 1998. Pasch et al. (2001) provides a detailed account of the history of Georges. During this period, Georges was located 1000 km east-northeast of St. Martin and was moving westward at 7.0 m s$^{-1}$ over 28°-29°C SSTs. The large-scale vertical shear was from the west-northwest. Maximum observed flight-level winds were 69 m s$^{-1}$ at 4.2 km altitude, and the MSLP was 939 mb. Over the course of the 12 hr period encompassing the inner-core observation period, Georges was intensifying with an average drop in MSLP of 1.2 mb hr$^{-1}$. Both aircraft made eye penetrations at ~4.2 km altitude. The first aircraft (I)

made 3 penetrations between 1900 and 2100 UTC, while the second aircraft (H) made 2 penetrations between 2300 and 0100 UTC. All quadrants were sampled at least once by each aircraft. Analysis of convective core buoyancy characteristics was limited to the 4 radial legs flown by the second aircraft.

In contrast to the asymmetric eyewalls observed in both Guillermo and Edouard, the single-scan LF reflectivity fields from the 5 eye penetrations at 4.2 km altitude in Georges (Fig. 4.14) exhibited a closed and nearly symmetric eyewall (i.e., a continuous ring of reflectivity > 30 dBZ) at ~25 km radius. Isolated convective cells with maximum reflectivities > 40 dBZ, however, were embedded within the eyewall, and these cells evolved as they moved cyclonically. Convective cells were not tracked in animated radar imagery for this case.

Although Georges' eyewall appeared nearly symmetric in radar reflectivity, the vertical velocity and core buoyancy characteristics (Fig. 4.15) were much more asymmetric. Mesoscale updrafts > 1 m $s^{-1}$ dominated the eastern and northern portions of the eyewall, while weaker mesoscale ascent (and descent) was found in the western and southern sections. A total of 6 updrafts cores (Fig. 4.15b) and 5 downdraft cores with $\overline{w} < -1$ m $s^{-1}$ (Fig. 4.15c) were encountered in the eyewall region (~13-45 km radius annular ring) along the four radial legs flown by the second aircraft. While azimuthal relationships are difficult to ascertain from such little data, two noteworthy characteristics are evident. First, only two of the five stronger updraft cores were positively buoyant. However, both cores exhibited $\overline{B} > 0.25$ K and were located along the inner edge of the eyewall. Furthermore, both cores were collocated with the maximum $\theta_e$ and $\zeta$ observed along each respective leg (i.e., the $\theta_e$ and $\zeta$ profiles exhibited maxima in the eyewall region with depressed values within the eye, similar to Guillermo on 2 August at 5.5 km altitude). Second, the four downdraft cores located just outside the the eyewall reflectivity maximum exhibited negative $\overline{B}$ with significant contributions from both $\overline{TB}$ and $\overline{WL}$.

Multiple inward spiraling convective and stratiform rainbands surrounded the eyewall at radii beyond ~45 km. As in Guillermo and Edouard, isolated convective cells tended

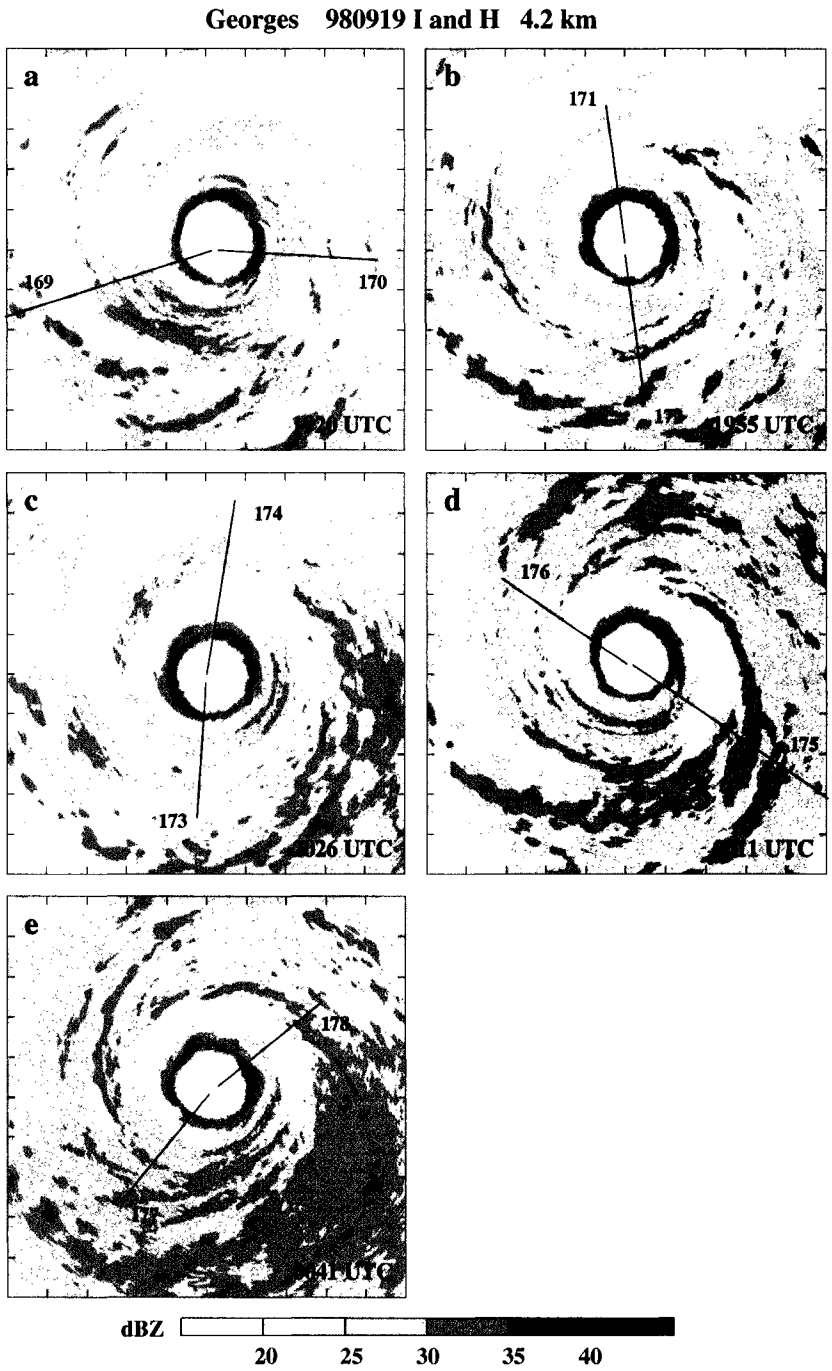


Figure 4.14: As in Fig. 4.1 but for Hurricane Georges on 19 September at (a) 1920 UTC, (b) 1955 UTC, (c) 2026 UTC, and (d) 0011 UTC and (e) 0041 UTC on 20 September 1998. The first three eye penetrations were flown by the first aircraft (I), and the final two penetrations were flown by the second aircraft (H).

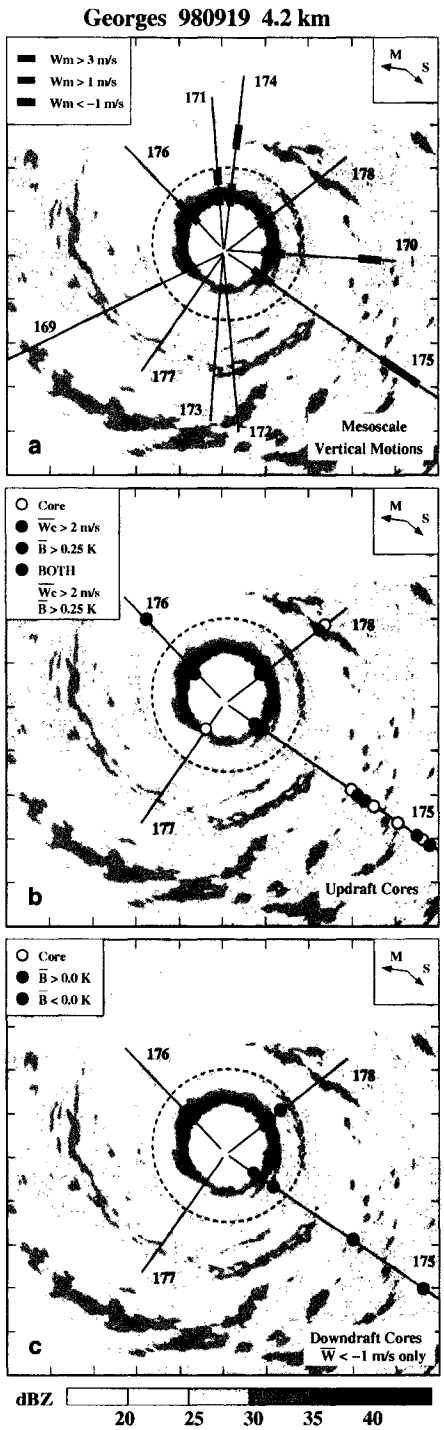


Figure 4.15: As in Fig. 4.5 but for Hurricane Georges between 1900 UTC on 19 September and 0100 UTC on 20 September 1998 at ~4.2 km altitude. The representative storm-relative radar reflectivity field was observed at 1955 UTC during the second eye penetration by the first aircraft. Note that core buoyancy characteristics could only be determined along the four radial legs flown by the second aircraft between 2300 and 0100 UTC.

to dominate the upwind portion of each rainband with stratiform precipitation dominant in the downwind portions. No appreciable mesoscale downdrafts were encountered during rainband penetrations (Fig. 4.15a), but several mesoscale updrafts were. A total of 11 updrafts cores (Fig. 4.15b) and 2 downdraft cores with $\overline{w} < -1$ m s$^{-1}$ (Fig. 4.15c) were encountered by the second aircraft. Roughly half of the updraft cores (6 of 11) exhibited $\overline{B} > 0.25$ K. Both downdraft cores were negatively buoyant.

## 4.5 Discussion

### 4.5.1 Azimuthal distribution of buoyant convection

The four case studies exhibited several striking similarities in azimuthal convective organization and composition. First, a pronounced wavenumber-one asymmetry in mesoscale vertical motion was observed in each eyewall. In three cases, the gross radar reflectivity also exhibited a persistent wavenumber-one asymmetry with its maximum located ~30°-90° downwind (upwind) of the mesoscale ascent (descent) maximum. Second, convective-scale updraft cores with appreciable positive total buoyancy ($\overline{B} > 0.25$ K) were also observed in each eyewall. Such cores tended to be found upwind of and collocated with the wavenumber-one mesoscale ascent maximum. More importantly, these cores were frequently located in regions where isolated convective-scale reflectivity cells (> 30 dBZ) were observed to develop, advect cyclonically with speeds slightly slower than the azimuthal mean-layer wind, and dissipate over the course of 10-20 min. Furthermore, these buoyant updraft cores accomplished a considerable fraction (~30-40%) of the total upward mass transport despite occupying < 10% of the total eyewall area. Third, several inward spiraling rainbands were observed outside each eyewall. The upwind segments of these rainbands tended to contain more positively buoyant updraft cores and isolated reflectivity cells than the more stratiform downwind segments. Fourth, numerous convective-scale downdraft cores with both positive and negative buoyancy were observed in the eyewall and rainbands of each case.

Investigations into causal mechanisms of azimuthal wavenumber-one convective structures in hurricanes have demonstrated dynamical relationships with motion-induced asym-

metric frictional convergence (e.g., Shapiro 1983) and vertical wind shear (e.g., Jones 1995; DeMaria 1996; Frank and Ritchie 1999). In regard to storm motion, Shapiro (1983) showed, using a slab boundary-layer model, that hurricane translation induces a frictional convergence maximum (and thus vertical motion maximum at the top of the boundary layer) ahead of the storm center. For slow-moving ($\sim$5 m s$^{-1}$) storms, this maximum comprised a broad arc across both forward quadrants. When storm motion was increased to $\sim$10 m s$^{-1}$, the convergence maximum become more concentrated in the right-front quadrant. The model results were supported by observations from two hurricanes. In regard to vertical shear, Jones (1995) and DeMaria (1996) showed, within the context of dry-adiabatic balanced dynamics, that the tilting of a vortex by vertical shear will induce a compensating secondary vertical circulation in an attempt to bring the vortex back toward a vertical orientation and maintain balanced flow. This circulation, which is comprised of downshear upward motion and upshear downward motion, creates a cold (warm) potential temperature anomaly downshear (upshear) of the storm center within the vortex. Subsequent flow along the distorted vortex isentropes will induced enhanced upward motion in the downshear-right quadrant. In a "full-physics" numerical simulation, however, Frank and Ritchie (1999) showed that condensational heating effectively removes the downshear cold anomaly, and the updraft maximum shifts to the downshear-left quadrant. Observational evidence of enhanced downshear convection has been provided by Reasor et al. (2000), Corbosiero and Molinari (2002), and Black et al. (2002).

Comparison of the wavenumber-one mesoscale vertical motion and reflectivity fields in the eyewall region (Figs. 4.5a, 4.11a, 4.13a, and 4.15a) with the orientation of the storm motion and vertical wind shear vectors reveals a consistent relationship with only vertical shear. For each case, the mesoscale ascent and reflectivity maxima were located either directly downshear or downshear left, in agreement with the aforementioned modeling and observational studies. No clear relationship with storm motion is apparent. Only Edouard and Georges exhibited any appreciable mesoscale ascent in their right-front quadrant. However, for these two cases the right-front and downshear-left quadrants overlap,

preventing a clear distinction between the relative roles of vertical shear and storm motion. Corbosiero and Molinari (2003) recently analyzed over 100 independent cases and showed that the influence of vertical shear on the azimuthal distribution of convection (inferred from observed lightning frequency) tends to dominate the effects from storm motion. The four cases presented here support such a tendency.

Inspection of Figs. 4.5, 4.11, 4.13, and 4.15 reveals that eyewall updraft cores with appreciable positive buoyancy and downdrafts cores with $\overline{w} < -1$ m s$^{-1}$ also exhibit consistent asymmetric relationships with the vertical shear vector orientation. In order to quantify these relationships, the radial legs in each case were rotated around the storm center so that the shear vector for the case was pointing due north. The eyewall area was divided into four regions with respect to the vertical shear vector: downshear right and left, and upshear right and left. The number of updraft and downdraft cores per 100 km of total eyewall region leg length was then determined for each quadrant. The normalization by total leg length was employed to account for small inequalities in leg numbers per shear-rotated quadrant.

Figure 4.16 shows the resulting normalized number of eyewall updraft cores encountered in each quadrant as well as the normalized numbers for when the cores are stratified by their $\overline{B}$ and $\overline{w}_c$ characteristics. Clearly, the more buoyant (and stronger) eyewall updraft cores were most often encountered in the downshear-left quadrant, but were rarely encountered in the upshear-right quadrant despite a nearly equal number of total updraft cores. Over 75% of downshear-left updrafts contained $\overline{B} > 0.25$ K and ~60% exhibited $\overline{w}_c > 2$ m s$^{-1}$. In contrast, less than 20% of upshear-right updrafts exhibited either $\overline{B} > 0.25$ K or $\overline{w}_c > 2$ m s$^{-1}$. Also note that the majority of more buoyant updraft cores (~70%) were located in the downshear quadrants, while the majority of stronger updrafts (~75%) were encountered in the two left quadrants. This cyclonic shift in the preferred quadrants may be indicative of typical updraft core evolution: buoyant updraft cores originate (or are generated) at low levels in the two downshear quadrants and begin to accelerate upward while being advected cyclonically around to the two left quadrants by the primary

circulation. The convective cell activity observed in Guillermo supports this notion, as well as the common observation of helical updraft trajectories and azimuthal separation between updraft initiation and reflectivity maximum (e.g., Marks and and Houze 1987; Marks et al. 1992).

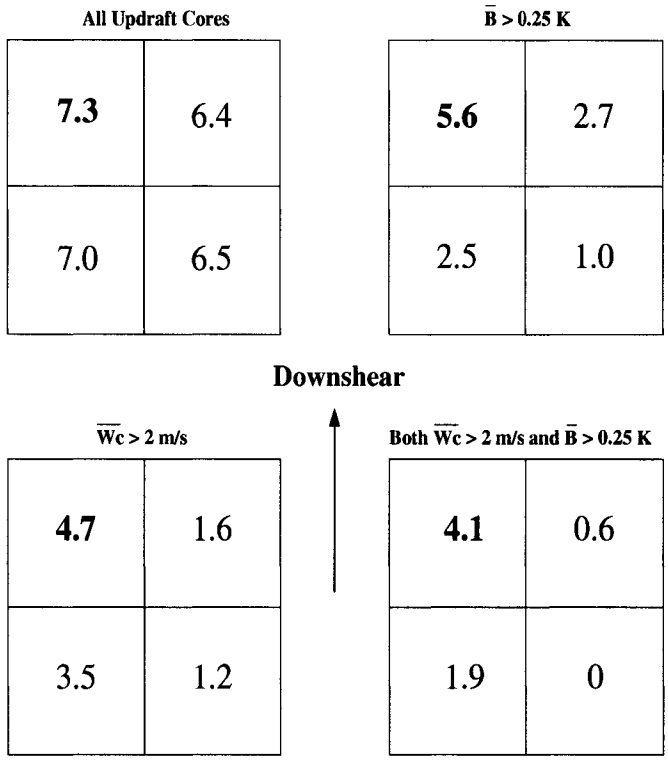


Figure 4.16: Shear-rotated quadrant plots showing the number of updraft cores encountered per 100 km of flight through the eyewall regions of the four case studies. Cores are stratified by their average convective vertical vertical velocity $\overline{w}_c$ and average total buoyancy $\overline{B}$ characteristics. The center of each box represents the storm center, and the upper two quadrants of each box represent the downshear direction.

Figure 4.17 shows the normalized number of downdraft cores with $\overline{w} < -1$ m s$^{-1}$ encountered in each quadrant. Over 60% of all such downdrafts were located in the two upshear quadrants, with a slight preference for the upshear-right quadrant. This asymmetric distribution is consistent with previous observations (e.g., Reasor et al. 2000; Black et al. 2002) and expectations (e.g., Jones 1995; DeMaria 1996; Frank and Ritchie 1999) of enhanced upshear descent. When the cores are stratified by $\overline{B}$, over 60% (70%) of negatively (postively) buoyant downdrafts were found in the two left (upshear) quadrants. Again, the cyclonic shift in preferred quadrants may be indicative of typical downdraft core

evolution. Consider a negatively buoyant downdraft core (resulting from perhaps localized evaporative cooling and or water loading) that originates at upper levels left of the shear vector. As the core accelerates downward and is advected cyclonically around to the upshear quadrants by the primary circulation, adiabatic warming will begin to overcome evaporational cooling (as the liquid water content decreases), and the downdraft core will become positively buoyant. The observed decreases in gross radar reflectivity as one moves cyclonically around the eyewall from the left quadrants to the upshear quadrants (see Figs. 4.5, 4.11 and 4.13) support this notion.

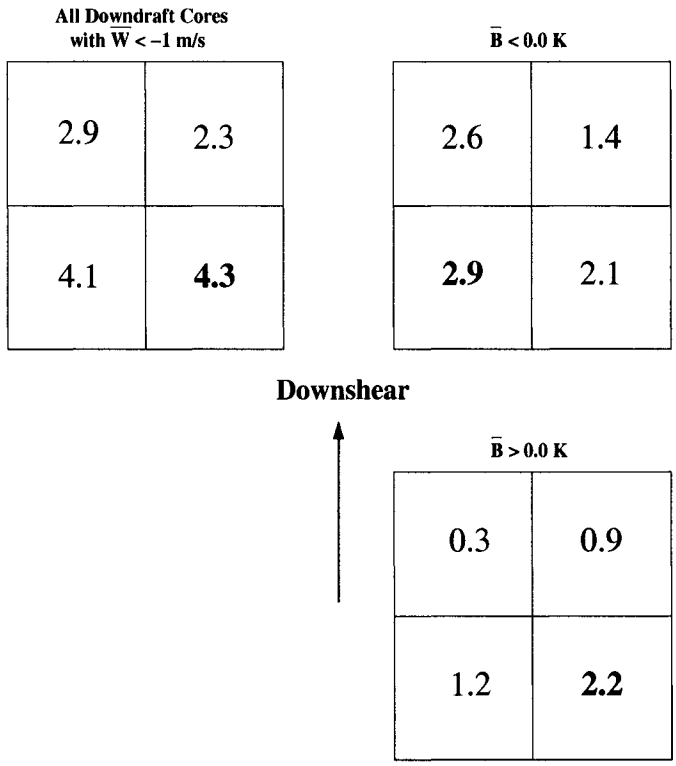


Figure 4.17: Shear-rotated quadrant plots showing the number of downdraft cores with average total vertical velocity $\overline{w} < -1$ m s$^{-1}$ encountered per 100 km of flight through the eyewall regions of the four case studies. Cores are stratified by their average total buoyancy $\overline{B}$ characteristics. The center of each box represents the storm center, and the upper two quadrants of each box represent the downshear direction.

Numerous studies have documented the mesoscale and convective structure of hurricane rainbands (Wexler 1947; Gentry 1964; Barnes et al. 1983; Willoughby et al. 1984; Barnes and Stossmeister 1986; Powell 1990; Barnes et al. 1991; Ryan et al. 1992; Barnes and Powell 1995). The consensus suggests that the upwind (or upband) segments tend

to be more cellular in radar structure with many strong convective updrafts, while the downwind (or downband) segments are more stratiform in structure with relatively few strong updrafts. Barnes et al. (1991) attributed these asymmetries to downband sounding stabilization (i.e., a reduction in CAPE) induced by the melting and evaporation of hydrometeors transported from upband regions. The case study results qualitatively support this conceptual picture. Updraft cores were more frequently encountered and tended to be more buoyant during upband penetrations (e.g., legs 48 and 49 in Fig 4.5; legs 61, 55, 58, and 64 in Fig. 4.11) than during downband penetrations (e.g., legs 46, 52, and 41 in Fig. 4.5; legs 53, 59, and 62 in Fig. 4.11).

Several studies (e.g., Barnes et al. 1983; Powell 1990; Cione et al. 2000) have also argued that cool, dry (i.e., negatively buoyant) convective downdrafts within rainbands were responsible for the thermodynamic modification of the boundary layer and the subsequent suppression of deep convection at inner radii, including eyewall convection. Of the 32 downdraft cores with $\overline{w} < -1$ m s$^{-1}$ encountered in rainbands (at altitudes above 3.0 km), 18 exhibited $\overline{TB} < -0.25$ K in the presence of liquid water. Assuming these downdrafts can maintain their negative $\overline{TB}$ through hydrometeor evaporation and penetrate into the boundary layer (below ~0.5 km altitude), our results support the notion that rainband downdraft cores can cool the low-level inflow. Such locally cool downdrafts were encountered equally in both upband and downband segments.

On a final note concerning the azimuthal distribution of convection, the consistent organization and composition observed in each case suggests that the vertical motion field of the hurricane inner core is much more complex than a simple symmetric or low-wavenumber mesoscale representation. Rather, the actual vertical motion field contains both a mesoscale component as well as numerous convective-scale updraft and downdraft cores with appreciable buoyancy that significantly contribute to the vertical transport of mass. While symmetric (or azimuthally averaged) mesoscale representations may be convenient for theoretical purposes, they can be quite unrepresentative of actual convective structure and processes. The extent to which such misrepresentation can occur is illus-

trated in Fig. 4.18. Shown are the radial profiles of $w_m$, $w_c$, and $B$ for all 12 legs flown at 5.5 km altitude in Guillermo on 2 August and their respective azimuthal averages. Several aspects are noteworthy. First, the mesoscale descent observed in the northern eyewall quadrant (Fig. 4.5a) is not evident in the azimuthally averaged $w_m$ profile (Fig. 4.18c). Second, the apparent symmetric ascent depicted at ~110 km radius in the azimuthally averaged $w_m$ profile was only observed during two rainband penetrations in the southeast quadrant. Third, the highly asymmetric distribution of updraft and downdraft cores resulted in an azimuthally averaged $w_c$ profile (Fig. 4.18c) that never exceeds $\pm 1$ m s$^{-1}$ (i.e., never satisfies the convective core criteria used here). Fourth, the azimuthally averaged $B$ profile (Fig. 4.18e) never exceeds $\pm 0.1$ K and exhibits little correlation with either the azimuthally averaged $w_m$ or $w_c$ profile. Therefore, given only the azimuthally averaged structure, one may erroneously conclude that Guillermo's vertical motion field at 5.5 km on 2 August consisted primarily of two mesoscale updraft rings with negligible forcing from buoyancy. Clearly, any evidence of convective updraft or downdraft cores with appreciable buoyancy was removed by the azimuthal averaging, and the actual asymmetric $w_m$, $w_c$, and $B$ structure was grossly misrepresented.

### 4.5.2 An unconventional source region for buoyant eyewall updrafts

The conventional wisdom states that the vast majority of air ascending in the eyewall originates in the large-scale environment and is driven inward by frictional dissipation in the boundary layer (e.g., Anthes 1982). As the air flows inward, surface heat and moisture fluxes increase the mean $\theta_e$ to values well above the large-scale environment (e.g., $\theta_e$ increases from 345 to 365 K). Upon approaching the eyewall, the air converges and is lifted. If, at some point during this forced ascent, an air parcel's $\theta_e$ exceeds the local environmental $\theta_e$, then the parcel will become locally buoyant and accelerate upward until the two $\theta_e$ values re-equilibrate (i.e., the parcel consumes the local positive CAPE). Numerous observations, however, indicate that appreciable positive CAPE is rarely observed in and near the eyewall (e.g., Sheets 1969; Frank 1977; Bogner et al. 2000). Furthermore, as discussed previously, convective downdrafts within rainbands can inject low $\theta_e$ air into the

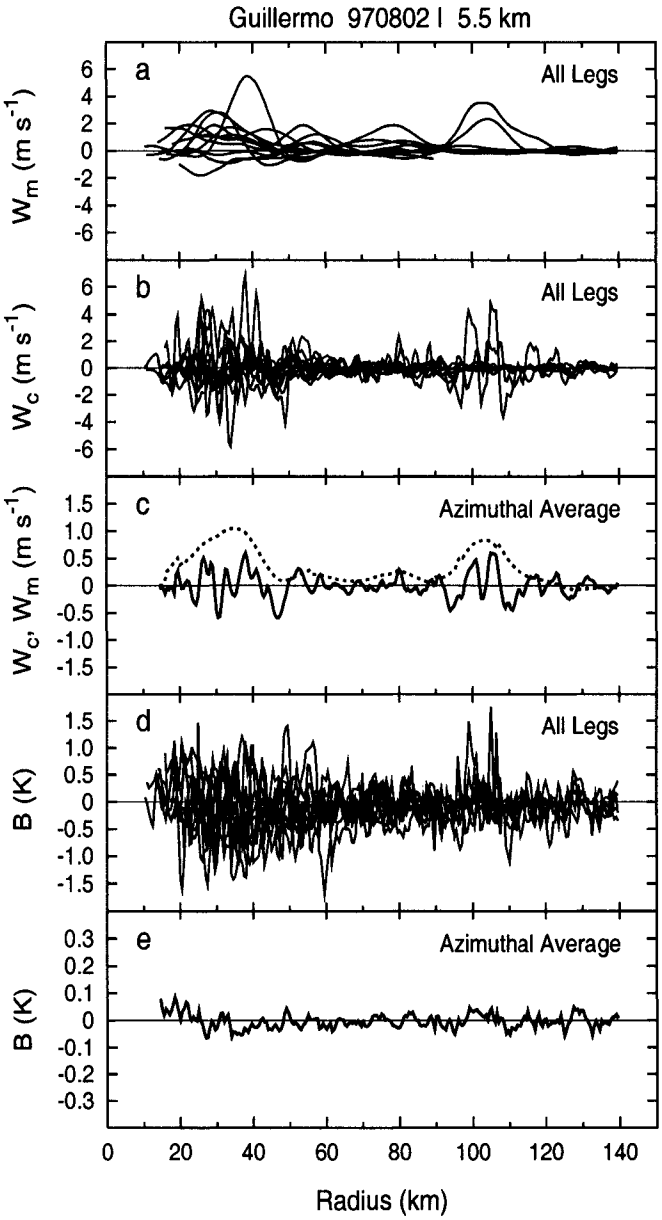


Figure 4.18: Radial profiles of (a) mesoscale vertical velocity $w_m$, (b) convective vertical velocity $w_c$, and (d) total buoyancy $B$ for all 12 radial legs flown at ~5.5 km altitude in Hurricane Guillermo between 1800 UTC on 2 August and 0100 UTC on 3 August 1997. Also shown are azimuthal averages of (c) $w_m$, $w_c$, and (e) $B$ computed for each 0.5 km radial bin in which data was available from at least 6 of the legs.

boundary layer and significantly lower the mean $\theta_e$ of the inflowing air (e.g., Barnes et al. 1983; Cione et al. 2000; Barnes and Bogner 2001). If adequate thermodynamic recovery of the inflow is not achieved prior to reaching the eyewall, subsequent eyewall convection may be suppressed (Powell 1990). In light of such obstacles, one might expect an eyewall updraft with appreciable buoyancy (e.g., $\overline{B} > 0.25$ K) to constitute a rare event. However, the results presented for each case and in Chapter 3 indicate that such buoyant updrafts are not so rare (~33% of all eyewall updraft cores exhibited $\overline{B} > 0.25$ K). How then do so many eyewall updraft cores acquire appreciable buoyancy?

Numerous observations (Hawkins and Imbembo 1976; Jorgensen 1984b; Willoughby 1998; LeeJoice 2000; Heymsfield et al. 2001; Kossin and Eastin 2001) and numerical simulations (Liu et al. 1997; Frank and Ritchie 2001; Braun 2002; Persing and Montgomery 2003) indicate that $\theta_e$ in the low-level eye can, at times, exceed $\theta_e$ in the eyewall by 5-10 K. Recent numerical hurricane simulations (Braun 2002; Persing and Montgomery 2003) have suggested that the outward advection of this high-$\theta_e$ eye air into the eyewall can generate locally buoyant updrafts. Here, we present observational evidence that several buoyant eyewall updraft cores in Guillermo and Georges originated in the low-level eye and were generated by asymmetric outflow associated with low-wavenumber mesovortices embedded within the eye and eyewall.

In order to diagnose the source region of buoyant eyewall updraft cores observed at flight-level, core average $\theta_e$ values were compared to vertical profiles of $\theta_e$ obtained below flight-level in both the eye and eyewall from GPS dropwindsondes. Hurricane Guillermo on 3 August 1997 was the first case in which GPS sondes were deployed in both the eye and eyewall. The upper aircraft (I at 5.5 km altitude) dropped 2 sondes in the eye, while the lower aircraft (H at 3.0 km) dropped one sonde in the eye and 6 in the eyewall. Multiple GPS sondes were also deployed in the eye (4 sondes) and eyewall (14 sondes) of Georges on 19 September 1998 from both aircraft at 4.2 km altitude. The sonde data for each case were obtained from the NOAA HRD quality-controlled data archive and further scrutinized following the methods of Bogner et al. (2000) to correct for any mixed-layer

humidity sensor wetting errors. Vertical profiles of $\theta_e$ were then computed using the Bolton (1980) formulation.

Figure 4.19a shows the drop locations and descent trajectories for the 9 sondes deployed in Guillermo on 3 August. Each of the 3 eye sondes were dropped well away from the eyewall in close proximity to the circulation center. Four of the eyewall sondes were deployed along the inner eyewall edge, while the other two were dropped within the high radar reflectivity region. Figure 4.19b shows the sonde-derived $\theta_e$ profiles. Eyewall $\theta_e$ ranged from 358 to 368 K but never exceeded 370 K, and the individual profiles exhibited little altitude dependence. In the eye, however, two profiles exhibited a rapid decrease in $\theta_e$ from ~375 K (below 2 km) to ~360 K (above 2 km). Therefore, below 5.5 km, air parcels with $\theta_e > 370$ K were only observed in the low-level eye. Comparison of the $\theta_e$ profiles with the $\theta_e$ observed in the eyewall updraft cores at 5.5 km altitude (Fig. 4.19b) reveals that 6 cores contained average $\theta_e > 370$ K, of which 3 exhibited $\overline{B} > 0.25$ K. Assuming the eyewall updrafts originated below 2 km, the low-level eye was the apparent source region for these 6 cores, not the boundary-layer inflow below the eyewall.

It is interesting to note that the eyewall updraft cores could be roughly divided into two groups: cores with $\theta_e > 365$ K and cores with $\theta_e < 365$ K. Given that lower $\theta_e$ air (~360 K) was located both inside and outside the eyewall above 2 km altitude (see Figs. 4.9, 4.10, 4.19b), one might expect entrainment mixing to have slightly reduced the updraft core average $\theta_e$ values during their ascent from 2 to 5.5 km. Thus, it seems plausible that several of the cores with $\theta_e > 365$ K may have also originated in the low-level eye. Further note that the majority of cores with $\overline{B} > 0.25$ K (12 of 17) and $\overline{w}_c > 2$ m s$^{-1}$ (10 of 15) contained $\theta_e > 365$ K. Therefore, the low-level eye may have been the *primary* source region for the stronger and more buoyant eyewall updrafts in Guillermo on 3 August.

Figure 4.20a shows the drop locations and descent trajectories for the 18 sondes deployed in Georges on 19 September. As in Guillermo, the eye sondes were dropped away from the eyewall in close proximity to the circulation center, and the eyewall sondes were dropped both within and along the inner edge of the eyewall with excellent azimuthal cov-

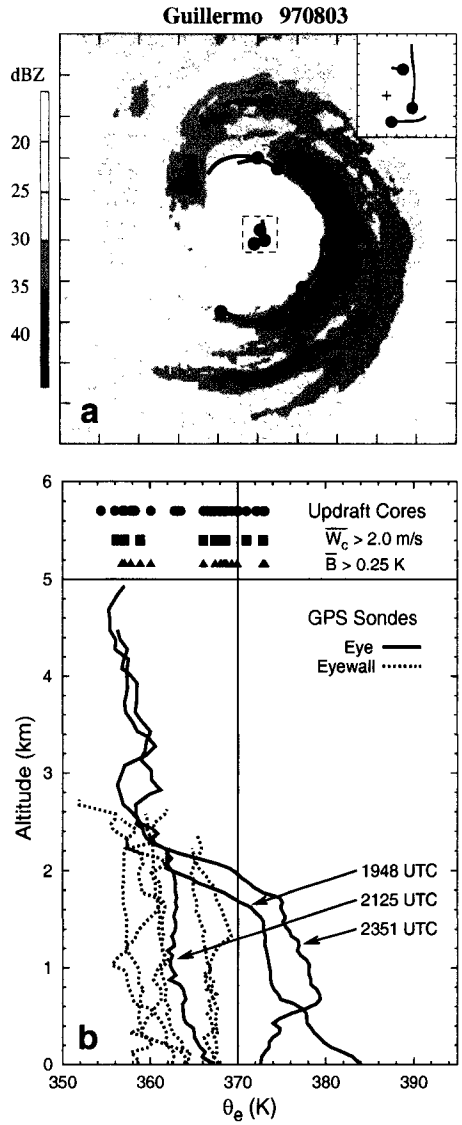


Figure 4.19: (a) Storm-relative radar reflectivity observed at ~3.0 km in Hurricane Guillermo at 2054 UTC on 3 August 1997. The domain is 120 km × 120 km and tic marks are shown every 12 km. Superimposed are GPS dropwindsonde launch locations (large solid circles) and their storm-relative trajectories (solid lines). The dashed inner box, enlarged in the upper right-hand corner, shows the trajectories for the GPS sondes launch in the eye. The enlarged inner box domain is 10×10 km with tic marks every 1 km, and the small cross indicates the circulation center. (b) Vertical profiles of equivalent potential temperature $\theta_e$ obtained by the GPS sondes deployed in the eye (solid) and eyewall (dashed) of Hurricane Guillermo between 1900 UTC on 3 August and 0100 UTC on 4 August. Also shown are core average $\theta_e$ values for all eyewall updraft cores (filled circles) observed at ~5.5 km altitude during the same period, as well as the subset of updraft cores with average convective vertical velocity $\overline{w}_c > 2$ m s$^{-1}$ (filled squares) and the subset of updraft cores with average total buoyancy $\overline{B} > 0.25$ K (filled triangles).

erage. The majority of eyewall $\theta_e$ profiles (Fig. 4.20b) exhibited little altitude dependence as typical $\theta_e$ values ranged between 355 and 365 K. A few eyewall profiles decreased from ~360 K near the surface to ~350 K at 4 km altitude, indicative of appreciable positive CAPE. Each eye sonde exhibited a pronounced decrease in $\theta_e$ from ~370 K (below 1 km) to ~360 K (above 1 km). Therefore, below 4.2 km, air parcels with $\theta_e > 365$ K were only observed in the low-level eye. Comparison with $\theta_e$ observed in the eyewall updraft cores at 4.2 km altitude (Fig. 4.20b) reveals that 2 cores contained average $\theta_e > 365$ K, and both exhibited $\overline{B} > 0.25$ K and $\overline{w}_c > 2$ m s$^{-1}$. Again, assuming the updrafts originated below ~1 km, the low-level eye was the apparent source region for both cores.

It is important to note that humidity sensor wetting errors may still exist above the mixed layer. Any such errors will result in an over-estimate of RH, and thus an over-estimate of $\theta_e$ in each profile. Figures 4.21 shows the RH, specific humidity ($q$), and potential temperature ($\theta$) profiles for the eye and eyewall sondes deployed in Guillermo on 3 August and in Georges on 19 September. In Guillermo (Figs. 4.21a, 4.21c, and 4.21e), two eye profiles exhibit saturation in the ~0.5 to ~1.5 km altitude layer and four eyewall profiles exhibit saturation above ~0.5 km. Given that the eyewall sondes descended primarily in cloud, and the eye sondes penetrated a statocumulus deck below ~2 km (observed in aircraft video imagery), near-saturated conditions at these altitudes in each region is not unrealistic. However, if the saturated conditions resulted from sensor wetting errors that over-estimated RH by 5-10% (i.e., actual RH values are 90-95% as observed by the other sondes), then the $\theta_e$ profiles are erroneously too high by 3-5 K at these altitudes. Fortunately, application of such corrections to the saturated segments of both eye and eyewall $\theta_e$ profiles does not alter (but rather strengthens) our conclusion. Similar arguments can be applied to the sondes deployed in Georges (Figs. 4.21b, 4.21d, and 4.21f).

The results from Guillermo and Georges clearly suggest that the high-$\theta_e$ low-level eye was an important source region for the buoyant eyewall updrafts. An important remaining question is, what dynamical mechanism(s) transported the high-$\theta_e$ eye air out-

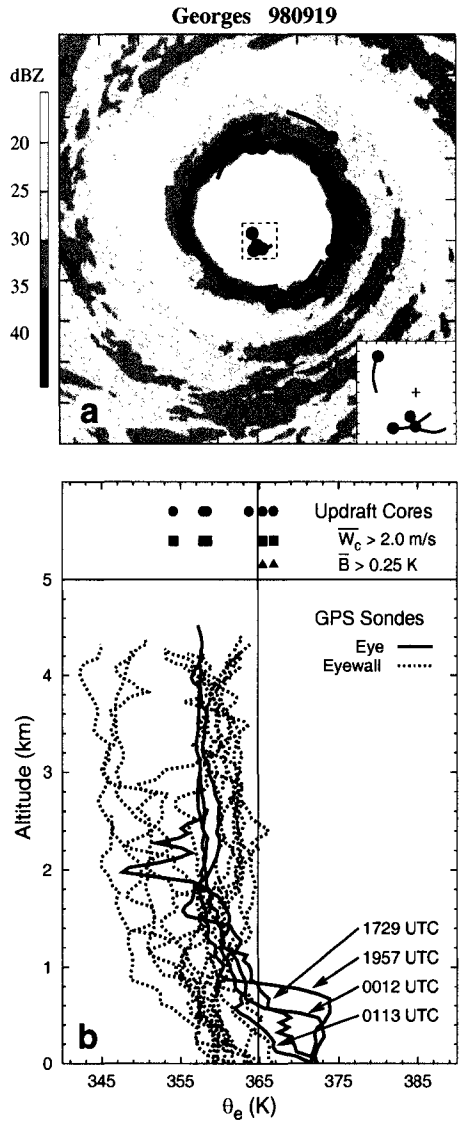


Figure 4.20: As in Fig. 4.19 but (a) at ~4.2 km in Hurricane Georges at 0041 UTC on 20 September 1998, and (b) for GPS sondes deployed in Hurricane Georges between 1900 UTC on 19 September and 0100 UTC on 20 September. Core average equivalent potential temperature $\theta_e$ values are only shown for eyewall updraft cores encountered at ~4.2 km altitude by the second aircraft between 2300 and 0100 UTC.

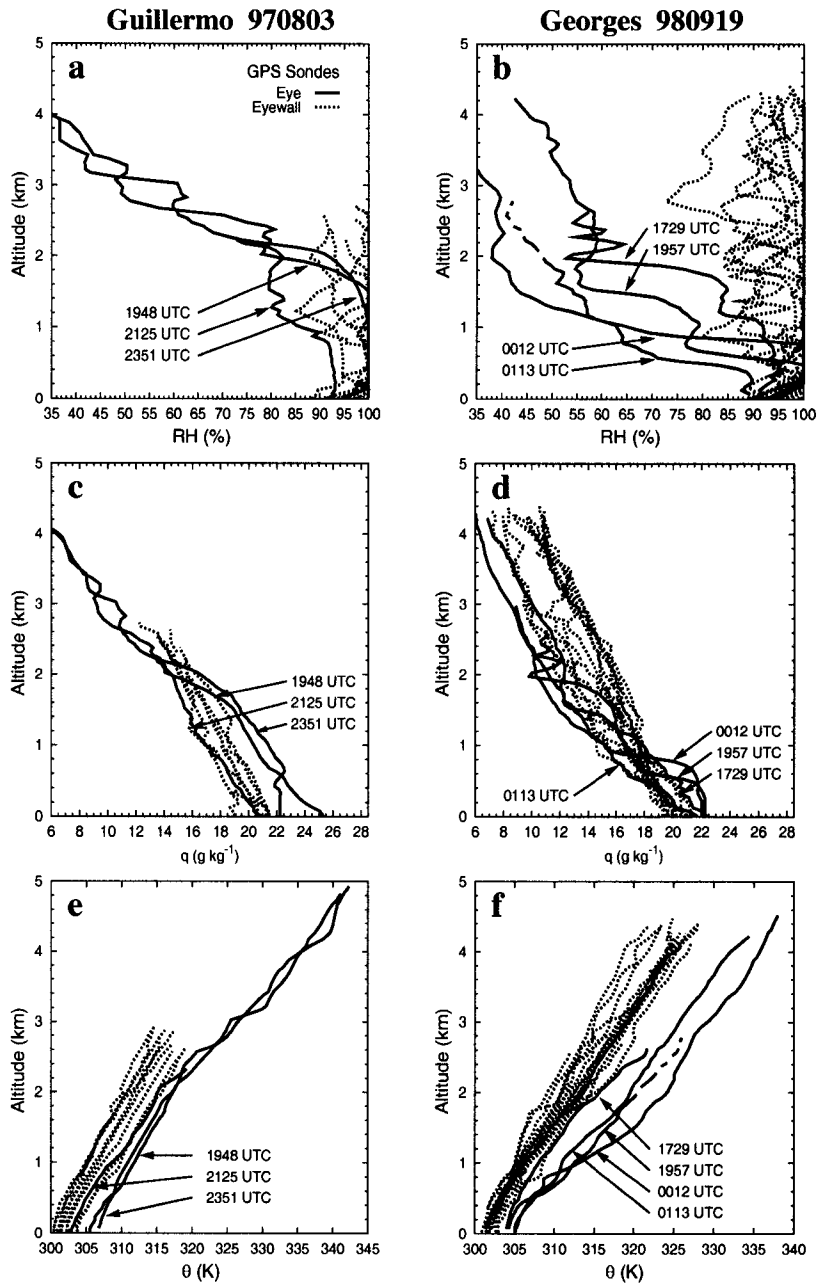


Figure 4.21: Vertical profiles of (a)-(b) relative humidity $RH$, (c)-(d) specific humidity $q$, and (e)-(f) potential temperature $\theta$ obtained by the GPS sondes deployed in the eye (solid) and eyewall (dashed) of Hurricane Guillermo between 1900 UTC on 3 August and 0100 UTC on 4 August and Hurricane Georges between between 1900 UTC on 19 September and 0100 UTC on 20 September. The three left-hand (right-hand) panels are for Hurricane Guillermo (Georges).

ward into the eyewall? Potential mechanisms include: thermally and dynamically driven secondary circulations (e.g., Shapiro and Willoughby 1982; Jorgensen 1984b); local supergradient accelerations (e.g., Malkus 1958; Gray and Shea 1973); "through flows" induced by storm translation (e.g., Weatherford 1989; Peng and Williams 1990); and asymmetric low-wavenumber circulations (e.g., Marks et al. 1992; Reasor et al. 2000; Montgomery et al. 2002). Here, we focus on the latter. Schubert et al. (1999) recently demonstrated that a vertical vorticity structure comprised of an annular ring of enhanced vorticity in the eyewall with relatively weak vorticity in the eye and outside the eyewall can support the growth of barotropic instabilities (i.e., vortex-Rossby waves), which lead to vigorous asymmetric mixing between the eye and eyewall. During the mixing process, the enhanced annular ring of vorticity breaks down into low-wavenumber mesovortices that initially distort the local flow into polygonal patterns (Kossin and Schubert 2001) and then actively exchange mass between the eye and eyewall (Kossin and Eastin 2001). A number of observational studies have documented mesovortices in the eye and eyewall of intense hurricanes (Fletcher et al. 1961; Bluestein and Marks 1987; Black and Marks 1990; Willoughby and Black 1996; Hasler et al. 1997; Kossin et al. 2002).

Several observations from Guillermo and Georges suggest that such asymmetric low-wavenumber circulations (or mesovortices) may have been responsible for the outward advection of high-$\theta_e$ air into the eyewall. First, the flight-level vertical vorticity profiles in Guillermo (Figs. 4.9 and 4.10) and Georges (not shown) satisfy the criteria for barotropic instability (Schubert et al. 1999). Second, the evolution of Guillermo's vorticity profiles is consistent with expectations for vigorous asymmetric mixing between the eye and eyewall (Kossin and Eastin 2001). Third, the polygonal (or wave-like) pattern in radar reflectivity along the inner edge of Guillermo's eyewall at 3.0 km altitude (Fig. 4.19a) may be indicative of asymmetric hydrometeor advection induced by mesovortical flow (Kossin and Schubert 2001; Montgomery et al. 2002). Fourth, the $\theta_e$ evolution in the low-level eyes of Guillermo and Georges is suggestive of substantial rapid mixing between the high-$\theta_e$ eye and relatively low-$\theta_e$ eyewall. In Guillermo (Fig. 4.19b), for example, the average $\theta_e$

observed near the circulation center below 2 km changed from ~375 K at 1948 UTC to a typical eyewall value of ~365 K at 2125 UTC, and then returned to ~375 K at 2351 UTC. Similar, but less dramatic, evolutions occurred in Georges (Fig. 4.20b).

Finally, inspection of video imagery obtained from the aircraft's nose, right, and left video cameras revealed striking visual evidence of mesovortices within the low-level eye clouds of both Georges and Guillermo. Figure 4.22 shows imagery obtained from the nose camera video during two passes through Georges' eye by the first aircraft.[2] During each pass the eye was clear except for a shallow layer of stratocumulus near the sea surface. Embedded within these clouds were three coherent swirling structures, or mesovortices, located just inside the eyewall along the southern (Figs. 4.22a and 4.22b), northeastern, and northwestern (Fig. 4.22c) edges of the eye. Adjacent to these apparent mesovortices, the eyewall exhibited a complex structure in which cumulus cloud striations tilted outward and upwind with height. Similar eyewall striations have been documented in intense hurricanes (e.g., Bluestein and Marks 1987; Hasler et al. 1997; Kossin et al. 2002), and Bluestein and Marks (1987) speculated that such striations may be individual buoyant convective elements. It is interesting to note that both of Georges' eyewall updraft cores with $\overline{B} > 0.25$ K were located along the inner eyewall edge (Fig. 4.15b). Video imagery from Guillermo on 3 August also showed cyclonically banded structures in the low-level eye clouds (and cumulus striations in the eyewall). However, broken and scattered cloud decks at flight-level prevented documentation of their coherency and number.

### 4.5.3 Buoyant updraft cores and hurricane evolution

Two contrasting conceptual theories concerning the role of buoyancy in inner-core convection and hurricane evolution have been put forth. First, Malkus and Riehl (1960) and Riehl and Malkus (1961) speculated that a large fraction of the mass lifted from the

---

[2]Unfortunately, the second aircraft's observation period occurred after sunset during a new moon, so video concurrent with the convective core analysis was unavailable. However, the persistence of the observed low-level cloud features during the first aircraft's observation period, just 4 hrs prior, suggest these features were still present during the second observation period.

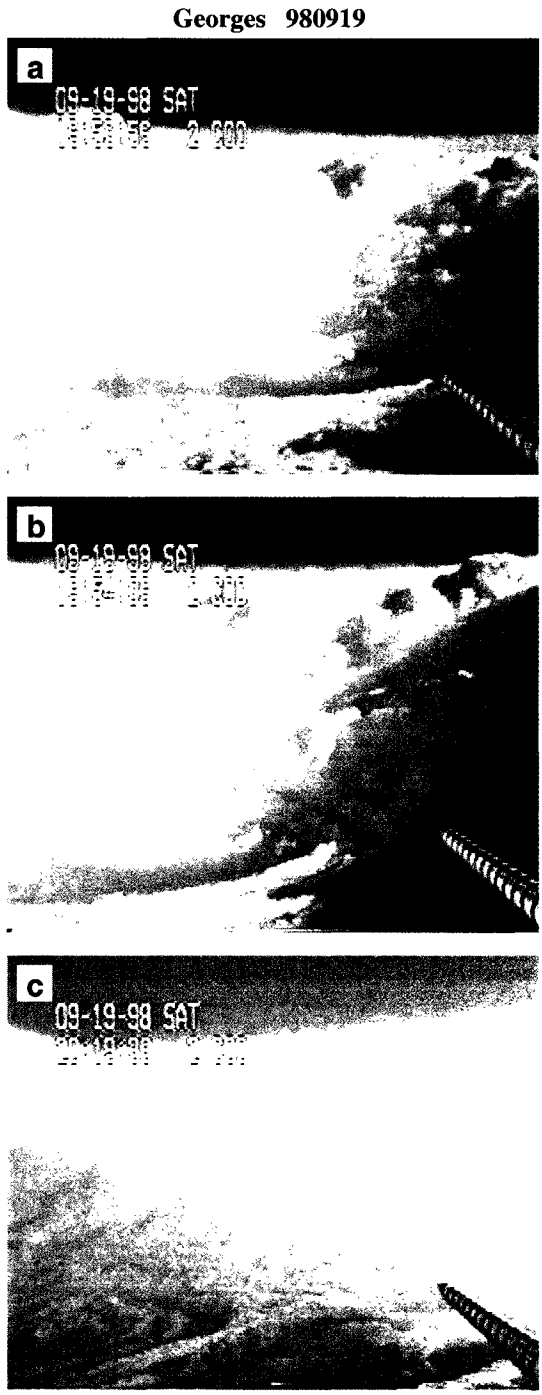


Figure 4.22: Video imagery of clouds in the low-level eye and along the inner edge of Georges' eyewall during the first flight between 1900 and 2100 UTC on 19 September 1998. Images were obtained by the aircraft's nose video camera (the gust probe arm that extends from the aircraft nose is visible in the lower right-hand corner of each panel). Views are toward (a) the south at 1954 UTC, (b) the south at 1955 UTC, and (c) the north at 2019 UTC. Note the cyclonic swirls in the low-level eye clouds and the cumuliform towers in the eyewall adjacent to the cyclonic swirls.

surface to upper levels ascends rapidly in a few isolated undilute buoyant updrafts, or "hot towers", rather than in a symmetric and gradual mesoscale updraft. Their hypothesis was based upon closure requirements for symmetric mass and heat budgets of the inner core of Hurricane Daisy (1958) and was supported by photographic cloud analyses (Malkus et al. 1961). The hot-tower theory links the essential physics of hurricane maintenance and evolution to asymmetric convective-scale buoyant updrafts. In contrast, Emanuel (1986) and Rotunno and Emanuel (1987) argued that the hurricane inner core is often close to a state of moist symmetric neutrality such that the majority of vertical mass transport is accomplished by uniform rings of mesoscale ascent forced entirely by boundary-layer convergence. The assumption of moist neutrality was based upon the observed decrease in CAPE as one moves from the large-scale environment inward to the inner core (e.g., Bogner et al. 2002). Hurricane maintenance and evolution was argued to depend exclusively upon self-induced anomalous enthalpy fluxes from the ocean with virtually no contribution from buoyancy. Thus, the moist symmetric neutrality theory suggests that asymmetric buoyant updrafts play a negligible role in both vertical mass transport and the essential physics.

The differences between the two theories naturally raises the question of whether the essential physics of hurricane maintenance and evolution are captured by the symmetric circulation, or are hot towers integral components? Are hot towers just anomalies superimposed upon the symmetric vortex, or do they play a significant role? In essence, these questions are analogous to whether the essential physics of the general global circulation are captured by the zonally symmetric circulation, or are mesoscale convective systems integral and significant components? The primary energy source that drives both hurricanes and the general circulation is latent heat release. Globally, most latent heat release occurs in association with deep convective and mesoscale cloud systems (e.g., Houze 1993; Emanuel 1994). While these zonally asymmetric cloud systems collectively comprise a zonally symmetric heat source that drives the zonally symmetric circulation (e.g., Lindzen and Hou 1988), the cloud systems also induce local circulations that influence subsequent convection (e.g., Zipser 1977; Mapes 1993), drive large-scale longitudinal circulations that

influence the zonal distribution of convection (e.g., Hartmann et al. 1984), and excite synoptic-scale longitudinal waves that significantly contribute to the net meridional transport of heat and momentum (e.g., Gill 1982; Masuda 1988). Clearly, mesoscale convective systems are essential components of the general global circulation. What do the case study results suggest for hot towers in hurricanes?

The finding, in each case study, of a few updraft cores with appreciable buoyancy that occupy only a small fraction of the total area but accomplish a considerable fraction of the total upward mass transport supports the notion that transient asymmetric hot towers are integral components of inner-core convective organization. To the extent that latent heat release and upward vertical mass transport correspond, the results further imply that a significant fraction of total inner-core latent heat release occurs in association with asymmetric hot towers. While the hot towers collectively comprise a symmetric heat source that drives the symmetric circulation (e.g., Shapiro and Willoughby 1982), the hot towers also excite local circulations and azimuthal waves that can significantly influence both subsequent convection (e.g., Powell 1990) and hurricane evolution (e.g., Ooyama 1982; Heymsfield et al. 2001; Enagonio and Montgomery 2001). Therefore, the case study results suggest that symmetric (or azimuthally averaged) representations of the inner-core, while convenient for theoretical purposes, are incomplete and in some cases (see Fig. 4.18) quite unrepresentative of actual physical processes.

The question remains as to what role hot towers (or asymmetric buoyant convective updrafts) play in hurricane evolution. Three specific roles (or mechanisms) are discussed here. For each mechanism, circumstantial support is provided by the case studies, as well as previous observational and numerical studies. The discussions focus on how buoyant convection can contribute to the maintenance of a steady-state hurricane by inducing a net spin-up of the mean vortex equal to the net spin-down experienced by the storm. Extension to intensification (weakening) simply requires the buoyant convection to induce a net spin-up greater than (less than) the net spin-down.

The first mechanism through which buoyant inner-core convection can significantly contribute to hurricane evolution is by driving a net deep-layer radial inflow above the frictional boundary layer that, through absolute angular momentum conservation, can spin-up and maintain the mean vortex against frictional dissipation. Since the upward acceleration of an air parcel will induce lateral entrainment and a local mass convergence, it seems plausible that an ensemble of buoyant updraft cores can drive such a net radial inflow. Recall that each the four cases contained numerous buoyant updraft cores in both the eyewall and rainband regions (Figs. 4.5, 4.11, 4.13, and 4.15). Figure 4.23 shows that each case also exhibited significant radial inflow outside the eyewall above the frictional boundary layer. Such inflow is not unique to these cases. Numerous observational analyses of the secondary circulations in intense hurricanes also depict significant deep-layer radial inflow above the boundary layer (Riehl and Malkus 1961; Gray and Shea 1973; Jorgensen 1984b; Marks and Houze 1987; Roux and Viltard 1995; Dodge et al. 1999). This mechanism is consistent with Ooyama's (1982) conceptual model of hurricane evolution.

It is interesting to note that the steady-state fields predicted by the nonhydrostatic model of Rotunno and Emanuel (1987) also show a deep-layer radial inflow and an accelerating updraft in the lowest 10 km of the eyewall (see their Fig. 5). Such structure is not consistent with strictly moist-neutral ascent above the frictional boundary layer, as contended by Emanuel (1986). Rather, the accelerating eyewall updraft and mid-level inflow suggests that some buoyancy is present in the steady-state, and thus required for hurricane maintenance.

The second mechanism by which buoyant convection can contribute to hurricane evolution is through the generation of adiabatic heating from mass-compensating subsidence. Since the upward acceleration of an air parcel will induce a local over-turning circulation, it seems plausible that an ensemble of buoyant convection will drive an ensemble of convective downdrafts. In a nearly moist-neutral environment (i.e., the inner core), any given downdraft will become a adiabatic heat source (and positively buoyant) once the cooling induced by hydrometeor evaporation is overcome. Recall that the eyewall and

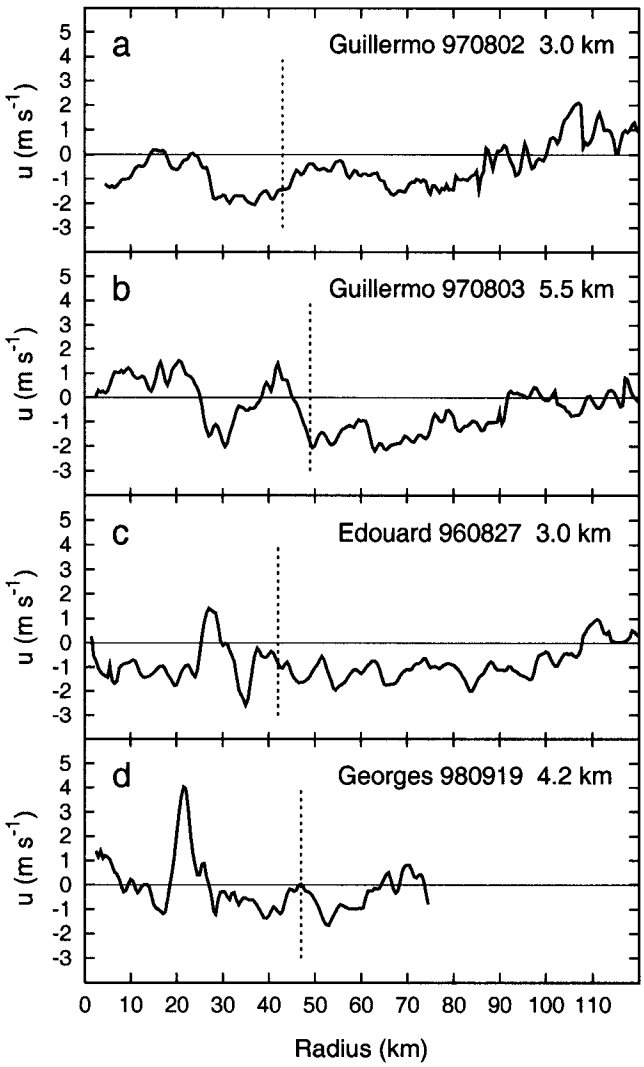


Figure 4.23: Azimuthal mean radial velocity $u$ at (a) ~3.0 km altitude in Hurricane Guillermo between 1800 UTC on 2 August and 0100 UTC on 3 August 1997, (b) ~5.5 km altitude in Hurricane Guillermo between 1900 UTC on 3 August and 0100 UTC on 4 August 1997, (c) ~3.0 km altitude in Hurricane Edouard between 1800 and 2400 UTC on 27 August 1996, (d) ~4.2 km altitude in Hurricane Georges between 1900 UTC on 19 September and 0100 UTC on 20 September 1998. Azimuthal means were computed for each 0.5 km radial bin in which data was available from at least half of the radial legs flown. Vertical dashed lines denote the approximate separation radius between the eyewall and rainband regions. Note that each profile is dominated by radial inflow outside ~30 km radius.

rainbands of each case contained numerous positively buoyant downdraft cores in close proximity to buoyant updraft cores (Figs. 4.5, 4.11, 4.13, and 4.15). Several studies of intense hurricanes have also documented locally warm convective downdrafts adjacent to deep convection (Jorgensen 1984a; Black et al. 1986; Black et al. 1994; Barnes and Powell 1995; Heymsfield et al. 2001). Such a heat source will induce a localized warming in the vertical temperature profile which, through hydrostatics, will enhance the local pressure gradient and lower the surface pressure. Therefore, hurricane maintenance can be achieved if an ensemble of buoyant convection can generate an enhancement of the mean radial pressure gradient and a spin-up of the mean vortex equal to the spin-down induced by friction. This mechanism is consistent with the Heymsfield et al. (2001) conceptual model of how hot towers influence hurricane evolution.

The third mechanism through which buoyant convection can contribute to hurricane evolution is by the generation of localized vertical vorticity anomalies and subsequent up-scale dynamical interactions. Recent studies (Montgomery and Enagonio 1998; Enagonio and Montgomery 2001) have demonstrated that localized positive vertical vorticity (or potential vorticity) anomalies superimposed upon a strong cyclonic vortex will become axisymmetrized and spin-up the vortex mean flow. Since the upward acceleration of an air parcel will converge and stretch the background vertical vorticity, creating a local vorticity anomaly, it seems plausible that locally buoyant updraft cores act to generate such vertical vorticity anomalies. Recall that several of the more buoyant updraft cores in Guillermo were collocated with localized positive vertical vorticity anomalies (Figs. 4.4 and 4.10). Such collocations were also observed in Edouard and Georges. Enagonio and Montgomery (2001) further showed that the axisymmetrization of a single vorticity anomaly produced only a small intensification of the mean vortex ($\sim$0.5 m s$^{-1}$ over $\sim$3 days), but the combined effects of several "pulsed" anomalies produced a more appreciable intensification ($\sim$10 m s$^{-1}$ over $\sim$3 days). Again, recall that the buoyant updraft cores in Guillermo were frequently located in regions where many isolated convective-scale reflectivity cells were repeatedly observed to develop, mature, and dissipate over the course of 10-20 min

(i.e., pulse). Evidence of the axisymmetrization process, as described in Kossin and Eastin (2001), was observed in the flight-level profiles of Guillermo (Figs. 4.9 and 4.10) and the video imagery of Georges (Fig. 4.22). Numerous studies of intense hurricanes have also documented pulsating convection (Malkus et al. 1961; Gentry et al. 1970; Black et al. 1986; Heymfield et al. 2001; Black et al. 2002) and evidence of the axisymmetrization process (Reasor et al. 2000; Kossin and Eastin 2001; Kossin et al. 2002). Clearly, hurricane maintenance can be achieved if an ensemble of buoyant convection can generate, through such up-scale dynamical interactions, a spin-up of the mean vortex equal to the frictional dissipation. This mechanism is consistent with Braun's (2002) envisionment of how hot towers influence hurricane evolution.

On a final note, it should be emphasized that the case study results do not imply that the hot-tower theory is the dominant conceptual model of hurricane physics. Rather, the results suggest that *hot towers are not a negligible component of hurricane physics*, as the symmetric neutrality theory contends. Inner-core vertical transports are accomplished through a collaborative effort between hot towers and the quasi-symmetric moist-neutral ascent. Likewise, hurricane evolution is envisioned to occur through a combination of each hot tower mechanism as well as a contribution from the symmetric dynamics.

# Chapter 5

# CONCLUSIONS

## 5.1 Summary

Aircraft data from 25 flights into 14 intense hurricanes have been used to derive both kinematic and buoyancy statistics for significant convective-scale vertical velocity events, called cores, superimposed upon the mesoscale transverse circulation. Initially, a 20 km running Bartlett filter was applied to all data to effectively separate the balanced mesoscale structure from the potentially unbalanced convective-scale structure in a manner consistent with both observations and current theory. Cores were defined as flight-leg sections in which the convective-scale vertical velocity exceeded an absolute value of 1 m $s^{-1}$ for at least 0.5 km; criteria analogous to those used by Jorgensen et al. (1985). The total buoyancy force (which includes water loading) was defined from convective-scale virtual potential temperature, pressure, and cloud and precipitation water content, in a similar manner to Braun (2002), assuming the respective mesoscale fields represent the appropriate reference state. Statistics of core kinematic and buoyancy properties have been summarized for both the eyewall and inner rainband regions at four altitude levels from 1.5 to 5.5 km. Our findings reveal that:

1. Distributions of core DIAM, $w_{c\ max}$, and $\overline{w}_c$ were approximately log-normal. Over 90% of cores were $< 4$ km in diameter and $< 4$ m $s^{-1}$ in average magnitude. The upper 10% of eyewall cores were both larger (by $\sim$1 km) and stronger (by 1-2 m $s^{-1}$ for $\overline{w}_c$) than corresponding rainband cores. These results are consistent with the analogous JZL core distributions despite slightly different core criteria.

2. Distributions of core $\overline{w}_m$ were approximately normal with median values of ~0.5 m $s^{-1}$ for both updraft and downdraft cores. The majority of all cores (~70%) were superimposed upon mesoscale ascent. In the eyewall, ~35% of all cores were superimposed upon mesoscale downdrafts, which suggests that hurricane eyewalls are not quasi-symmetric rings of ascent but contain regions of organized mesoscale descent.

3. Distributions of core $\overline{TB}$, $\overline{DB}$, $\overline{WL}$, and $\overline{B}$ were approximately normal. Median $\overline{TB}$ and $\overline{B}$ were slightly positive (negative) for updraft (downdraft) cores. The $\overline{WL}$ distributions were skewed toward negative values. Variability in $\overline{B}$ was dominated by the $\overline{TB}$ component with minimal contributions from either $\overline{DB}$ or $\overline{WL}$.

4. For both eyewall and rainband updraft cores, the median (and mean) $\overline{w}_c$ exhibited a statistically significant ~0.5 m $s^{-1}$ increase between 1.5 and 5.5 km altitude, which implies that "typical" updraft cores experience a modest upward acceleration above the boundary layer. The strongest 10% of eyewall updraft cores exhibited a ~1 m $s^{-1}$ increase in $\overline{w}_c$ over the same depth. Downdraft cores in both regions tended to be stronger at midlevels than at lower levels, but differences in median (or mean) $\overline{w}_c$ with altitude were not statistically significant.

5. The majority of updraft cores in the eyewall (~54%) and rainband (~63%) regions exhibited positive total buoyancy. The median (and mean) $\overline{B}$ for eyewall updraft cores were slightly positive (~0.1 K), but statistically significant, at altitudes below 4.0 km with near neutral values above. Corresponding $\overline{B}$ statistics for rainband updraft cores were larger in magnitude and positive at all altitudes with statistically significant values of ~0.25 K at 3.0 and 4.2 km. Regional differences in updraft core $\overline{B}$ are consistent with the reduction in background CAPE upon approach to the eyewall (Sheets 1969; Bogner et al. 2000).

6. Downdraft cores above 1.5 km in eyewalls and rainbands tended to exhibit negative total buoyancy. However, downdraft cores not superimposed upon stronger

mesoscale updrafts (i.e., cores that transport mass downward) tended to exhibit positive $\overline{B}$ at all altitudes, particularly the subsaturated cores with minimal liquid water content. These results imply that downdraft cores are more transient than updraft cores.

7. For each region, application of the median $\overline{B}$ statistics to a one-dimensional updraft model indicated that typical updraft core $\overline{B}$ were more than adequate to explain the observed increases in typical updraft core strength (median $\overline{w}_c$) with altitude. The results suggest that the typical vertical perturbation pressure gradient force is directed downward and largely opposes the positive buoyancy force. Entrainment and water-loading were also found to significantly reduce typical updraft core magnitudes.

8. Updraft cores occupied ~4% of the total area within 115 km of the storm center. Downdraft cores covered ~3% of the same area. In the eyewall region (between 15 and 45 km on average), updraft cores occupied ~10% of the area with another ~9% occupied by downdraft cores. Buoyant updraft cores occupied only ~5% of the eyewall area.

9. Updraft cores accomplished ~65% of the total upward mass, heat, and moisture transports in the eyewall, and ~50% in rainbands. The percentage tended to increase with height in the eyewall. Buoyant updraft cores accomplished ~40% of the total upward transport in both regions, despite occupying only a small percentage of the total area.

Extensive aircraft data collected in Hurricane Guillermo on 2 and 3 August 1997, Hurricane Edouard on 27 August 1996, and Hurricane Georges on 19 September 1998 were used to document several additional aspects of buoyant inner-core convection. For each case, airborne radar and in situ flight-level data were combined to elucidate gross azimuthal relationships between the precipitation and vertical velocity structure, with particular emphasis on convective-scale vertical velocity cores. For Guillermo and Georges,

additional observations from GPS dropwindsondes and aircraft video cameras were used to investigate the source of buoyant updraft cores in the eyewall. Despite considerable differences in large-scale environmental characteristics and intensity changes between cases, the analyses revealed multiple striking similarities in convective structure and organization. Our significant findings from these cases are as follows:

1. Each hurricane's eyewall exhibited a quasi-stationary wavenumber-one asymmetry in mid-level mesoscale vertical velocity. Mesoscale reflectivity maxima were located just downwind of the mesoscale ascent maxima. The orientation of these asymmetries with the large-scale vertical shear vector was consistent with theoretical expectations (Jones 1995; DeMaria 1996) and numerical simulations (Frank and Ritchie 2001). Maximum mesoscale ascent and precipitation was located in the downshear left quadrant with a relatively weaker mesoscale descent maximum located upshear.

2. Convective updraft cores, superimposed upon the mesoscale vertical motions, were evenly distributed around the eyewalls at midlevels. However, updraft cores with either appreciable local total buoyancy ($\overline{B} > 0.25$ K) or greater convective vertical velocity ($\overline{w}_c > 2$ m s$^{-1}$) exhibited consistent asymmetric relationships with the vertical shear vector orientation. Over 70% of the more buoyant updrafts were located in the two downshear quadrants, while ~75% of the stronger updrafts were found in the two left-of-shear quadrants. Over 60% of stronger and more buoyant updrafts were located in the downshear-left quadrant. These results suggest that most buoyant eyewall updraft cores originate at low levels downshear and accelerate upward while being cyclonically advected. In each case, the updraft cores with appreciable buoyancy occupied < 10% of the total eyewall area but accomplished ~30-40% of the total upward mass transport.

3. Numerous isolated convective precipitation cells (> 30 dBZ with diameters < 10 km) formed in the downshear portion of Guillermo's eyewall and moved at ~80-85% of the azimuthal mean tangential wind around the eyewall to the left-of-shear

quadrants before dissipation. Cells lifetimes were typically 10-20 min. The spatial similarity and azimuthal collocation of the convective cells and the more buoyant and stronger updrafts cores suggests that the transient cells may be manifestations of these updraft cores.

4. Convective downdraft cores that transport significant mass downward ($\overline{w} < -1$ m s$^{-1}$) were asymmetrically distributed in the mid-level eyewall. Over 60% were located in the upshear quadrants, with negative buoyancy dominant in upshear-left cores and positive buoyancy dominant in upshear-right cores. These results, coupled with the orientation of the mesoscale reflectivity maxima, imply that most eyewall downdraft cores are initially driven downward by evaporative cooling and water-loading until liquid water reduction permits adiabatic warming to dominate.

5. Many inward spiraling rainbands exhibited an upband/downband asymmetry at midlevels. Upband segments tended to contain more isolated convective cells and buoyant ($\overline{B} > 0.25$ K) updraft cores, while downband segments were more stratiform in nature with fewer buoyant updraft cores. No pronounced asymmetry was evident for downdraft cores with $\overline{w} < -1$ m s$^{-1}$, but ~55% exhibited appreciable negative buoyancy ($\overline{B} < -0.25$ K). These results are consistent with previous studies of hurricane rainbands (e.g., Barnes et al. 1983; Powell 1990a,b; Barnes et al. 1991; Ryan et al. 1992).

6. The low-level eye was an important source region for buoyant eyewall convection. In both Guillermo and Georges, multiple GPS dropwindsonde profiles revealed that $\theta_e$ in the low-level eye (below 1-2 km) exceeded eyewall $\theta_e$ by 5-10 K, and comparisons with $\theta_e$ in eyewall updraft cores encountered at midlevels indicated that several of the more buoyant cores likely originated in the low-level eye. Extensive circumstantial evidence, including video imagery of mesovortical cloud structures along the eye/eyewall interface, suggest that asymmetric low-wavenumber circulations (i.e., mesovortices) generated the buoyant updrafts by exporting high-$\theta_e$ air from the low-level eye into the relatively low-$\theta_e$ eyewall.

The results from this study clearly demonstrate that the hurricane transverse circulation is typically comprised of low-wavenumber mesoscale vertical motions as well as many convective-scale buoyant vertical motions that significantly contribute to the vertical transport of mass, heat, and moisture. These results support the notion that "hot towers" play an integral role in hurricane structure, dynamics, and evolution. As a result, three physical mechanisms were discussed whereby asymmetric buoyant convection could significantly contribute to hurricane maintenance and evolution. Circumstantial observational evidence was found to support each mechanism. The results further imply that idealized models which assume a neutral symmetric representation of the hurricane inner core (e.g., Emanuel 1986) are incomplete and may significantly misrepresent actual convective and dynamic processes that are crucial to storm maintenance and evolution. Clearly, future studies should account for both symmetric and asymmetric mesoscale processes, as well as asymmetric convective-scale processes, when addressing hurricane structure and evolution. Substantial improvements in hurricane intensity forecasting may only occur when all such processes are adequately addressed.

## 5.2 Future work

The datasets explored in this study have provided a unique perspective on the nature and organization of buoyant convection in intense hurricanes. If buoyant convective-scale vertical motions are an essential component of hurricane maintenance and evolution, as the results of this study suggest, then many questions regarding their origin, organization, and interaction with the mean vortex remain to be answered. The applicability of the results to minimal, weakening, or highly symmetric hurricanes needs to be addressed. Questions regarding the frequency and distribution of eyewall convection originating in the low-level eye, as well as the frequency, three-dimensional structure, and temporal evolution of the low-wavenumber mesovortices also need to be addressed. Furthermore, the ability of oceanic heat and moisture fluxes to effectively maintain the low-level eye as a continuous high-$\theta_e$ reservoir during periods of enhanced asymmetric mixing is unknown. If the mesovortices are transient but highly effective at removing the "buoyancy

reservoir", the mixing process could be linked to the episodic convective bursts that are frequently observed (Heymsfield et al. 2001). However, if the the mesovortices are persistent and surface fluxes are adequate to maintain the buoyancy reservoir, then asymmetric mixing between the eye and eyewall may be a continuous process. Further analysis of current datasets and future field experiments should supply crucial evidence addressing these questions. Cloud-resolving full-physics numerical models, as well as simple idealized models, should also be employed.

## REFERENCES

Ackerman, B., 1963: The distribution of liquid water in hurricanes. National Hurricane Research Project Report No. 62, U.S. Weather Bureau, 41 pp.

Anthes, R. A. 1982: *Tropical Cyclones: Their Evolution, Structure and Effects. Meteor. Monogr.*, No. 41, Amer Meteor. Soc., 208 pp.

Ayotte, B. A., and H. J. S. Fernando, 1994: The motion of a turbulent thermal in the presence of background rotation. *J. Atmos. Sci.*, 51, 1989-1994.

Barnes, G. M., and G. J. Stossmeister, 1986: The structure and decay of a rainband in Hurricane Irene (1981). *Mon. Wea. Rev.*, 114, 2590-2601.

Barnes, G. M., and M. D. Powell, 1995: Evolution of the inflow boundary layer of Hurricane Gilbert (1988). *Mon. Wea. Rev.*, 123, 2348-2368.

Barnes, G. M., and P. B. Bogner, 2001: Comments on "Surface observations in the hurricane environment". *Mon. Wea. Rev.*, 129, 1267-1269.

Barnes, G. M., E. J. Zipser, D. Jorgensen, and F. Marks, Jr., 1983: Mesoscale and convective structure of a hurricane rainband. *J. Atmos. Sci.*, 40, 2127-2137.

Barnes, G. M., J. F. Gamache, M. A. LeMone, and G. J. Stossmeister, 1991: A convective cell in a hurricane rainband. *Mon. Wea. Rev.*, 119, 776-794.

Baumgardner, D., 1983: An analysis and comparison of five water droplet measuring devices. *J. Climate Appl. Meteor.*, 22, 891-910.

Black M. L., R. W. Burpee, and F. D. Marks, Jr., 1996: Vertical motion characteristics of tropical cyclones determined with airborne Doppler radial velocities. *J. Atmos. Sci.*, 53, 1887-1909.

Black, M. L., J. F. Gamache, F. D. Marks Jr., C. E. Samsury, and H. E. Willoughby, 2002: Eastern Pacific Hurricanes Jimena of 1991 and Olivia of 1994: The effect of vertical shear on structure and intensity. *Mon. Wea. Rev.*, 130, 2291-2312.

Black, P. G., and F. D. Marks, 1991: The structure of an eyewall meso-vortex in Hurricane Hugo (1989). Preprints, *19th Conf. on Hurricanes and Tropical Meteorology*, Miami, FL, Amer. Meteor. Soc., 579-582.

Black P. G., F. D. Marks, Jr., and R. A. Black, 1986: Supercell structure in tropical cyclones. *Proc. 23rd Conf. on Radar Meteor.*, Snowmass, CO, Amer. Meteor. Soc., 255-259.

Black, R. A., 1990: Radar reflectivity-ice water content relationships for use above the melting level in hurricanes. *J. Appl. Meteor.*, 29, 955-961.

Black, R. A., H. B. Bluestein, and M. L. Black, 1994: Unusually strong vertical motions in a Caribbean hurricane. *Mon. Wea. Rev.*, 122, 2722-2739.

Black, R. A., and J. Hallett, 1986: Observations of the distribution of ice in hurricanes. *J. Atmos. Sci.*, 43, 802-822.

Bluestein, H. B.. and F. D. Marks, 1987: On the structure of the eyewall of Hurricane Diana (1984): Comparison of radar and visual characteristics. *Mon. Wea. Rev.*, 115, 2542-2552.

Bogner, P. B., G. M. Barnes, and J. L. Franklin, 2000: Conditional instability and shear for six hurricanes over the Atlantic ocean. *Wea. Forecasting*, 15, 192-207.

Bolton, D., 1980: The computation of equivalent potential temperature. *Mon. Wea. Rev.*, 108, 1046-1053.

Braham, R. R., Jr., and D. A. R. Kristovich, 1996: On calculating the buoyancy of cores in a convective boundary layer. *J. Atmos. Sci.*, 53, 654-658.

Braun, S. A., 2002: A cloud-resolving simulation of Hurricane Bob (1991): Storm structure and eyewall buoyancy. *Mon. Wea. Rev.*, 130, 1573-1592.

Byers, H. R., and R. R. Braham, 1949: The Thunderstorm Project. U.S. Weather Bureau, U.S. Dept. of Commerce Tech. Rep., 287 pp. [NTIS PB234515.]

Cecil, D. J., E. J. Zipser, and S. W. Nesbitt, 2002: Reflectivity, ice scattering, and lightning characteristics of hurricane eyewalls and rainbands. Part I: Quantitative description. *Mon. Wea. Rev.*, 130, 769-784.

Cione, J. J., P. G. Black, and S. H. Houston 2000: Surface observations within the hurricane environment. *Mon. Wea. Rev.*, 128, 1550-1561.

Corbosiero, K. L., and J. Molinari, 2002: The effects of vertical wind shear on the distribution of convection in tropical cyclones. *Mon. Wea. Rev.*, 130, 2110-2123.

Corbosiero, K. L., and J. Molinari, 2003: The relationship between storm motion, vertical shear, and convective asymmetries in tropical cyclones. *J. Atmos. Sci.*, 60, 366-376.

DeMaria, M., 1996: The effect of vertical shear on tropical cyclone intensity change. *J. Atmos. Sci.*, 53, 2076-2087.

DeMaria, M., and J. Kaplan, 1994a: Sea surface temperature and the maximum intensity of Atlantic tropical cyclones. *J. Climate*, 7, 1324-1334.

DeMaria, M., and J. Kaplan, 1994b: A statistical hurricane intensity prediction scheme (SHIPS) for the Atlantic basin. *Wea. Forecasting*, 10, 433-446.

DeMaria, M., and J. Kaplan, 1999: An updated statistical hurricane intensity prediction scheme (SHIPS) for the Atlantic and eastern North Pacific basins. *Wea. Forecasting*, 14, 326-337.

Dodge, P., R. W. Burpee, and F. D. Marks, Jr., 1999: The kinematic structure of a hurricane with sea level pressure less than 900 mb. *Mon. Wea. Rev.*, 127, 987-1004.

Doster, K. and P. T. Willis, 1976: Water content and entrainment of selected convective clouds. *Preprints Int. Conf. Cloud Physics*, Boston, MA, Amer. Meteor. Soc., 338-342.

Eastin, M. D., P. G. Black, and W. M. Gray, 2002a: Flight-level instrument wetting errors in hurricanes. Part I: Observations. *Mon. Wea. Rev.*, 130, 825-841.

Eastin, M. D., P. G. Black, and W. M. Gray, 2002b: Flight-level instrument wetting errors in hurricanes. Part II: Implications. *Mon. Wea. Rev.*, 130, 842-851.

Ebert, E. E., and G. J. Holland, 1992: Observations of record deep convection in Tropical Cyclone Hilda. *Mon. Wea. Rev.*, 120, 2240-2251.

Elsberry, R. L., G. J. Holland, H. Garrish, M. DeMaria, and C. P. Gaurd, 1992: Is there any hope for tropical cyclone intensity change prediction?–A panel discussion. *Bull. Amer. Meteor. Soc.*, 73, 264-275.

Emanuel, K. A., 1986: An air-sea interaction theory for tropical cyclones. Part I: Steady-state maintenance. *J. Atmos. Sci.*, 43, 585-604.

Emanuel, K. A., 1994: *Atmospheric Convection*, Oxford Press, 580 pp.

Enagonio, J., and M. T. Montgomery, 2001: Tropical cyclogenesis via convectively forced vortex Rossby waves in a shallow water primitive equation model. *J. Atmos. Sci.*, 58, 685-705.

Feind, R. E., A. G. Detweiler, and P. L. Smith, 2000: Cloud liquid water measurements on the Armored T-28: Intercomparisons between Johnson-Williams cloud water meter and CSIRO (king) liquid water probe. *J. Atmos. Oceanic Technol.*, 17, 1630-1638.

Fletcher, R. D., J. R. Smith, and R. C. Bundgaard, 1961: Superior photographic reconnaissance of tropical cyclones. *Weatherwise*, 14, 102-109.

Frank, W. M., 1977: The storm structure and energetics of the tropical cyclone: I. Storm Structure. *Mon. Wea. Rev.*, 105, 1119-1135.

Frank, W. M., and E. A. Ritchie, 1999: Effects of environmental flow upon tropical cyclone structure. *Mon. Wea. Rev.*, 127, 2044-2061.

Frank, W. M., and E. A. Ritchie, 2001: Effects of vertical shear on the intensity and structure of numerically simulated hurricanes. *Mon. Wea. Rev.*, 129, 2249-2269.

Franklin, J. L., S. J. Lord, S. E. Feuer, and F. D. Marks, 1993: The kinematic structure of Hurricane Gloria (1985) determined from nested analyses of dropwindsonde and Doppler radar data. *Mon. Wea. Rev.*, 121, 2433-2451.

Gamache, J. F., R. A. Houze, and F. D. Marks, Jr., 1993: Dual-aircraft investigation of Hurricane Norbert Part III: Water Budget. *J. Atmos. Sci.*, 50, 3221-3243.

Gentry, R. C., 1964: A study of hurricane rainbands. National Hurricane Research Project Report No. 69, U.S. Weather Bureau, 85 pp.

Gentry, R. C., T. T. Fujita, and R. C. Sheets, 1970: Aircraft, spacecraft, satellite, and radar observations of Hurricane Gladys, 1968. *J. Appl. Meteor.*, 9, 837-850.

Gill, A. E., 1982: *Atmosphere-Ocean Dynamics*, Academic Press, 662 pp.

Gray, W. M., 1965: Calculations of cumulus draft velocities in hurricanes from aircraft data. *J. Appl. Meteor.*, 4, 463-474.

Gray, W. M., and D. J. Shea, 1973: The hurricane's inner core region: II. Thermal stability and dynamic characteristics. *J. Atmos. Sci.*, 30, 1565-1576.

Hartmann, D. L., H. H. Hendon, and R. A. Houze Jr., 1984: Some implications of the mesoscale circulations in cloud clusters for large-scale dynamics and climate. *J. Atmos. Sci.*, 41, 113-121.

Hasler, A. F., P. G. Black, V. M. Karyampudi, M. Jentoft-Nilsen, K. Palaniappan, and D. Chesters, 1997: Synthesis of eyewall mesovortex and supercell convective structures in Hurricane Luis with *GOES-8/9* stereo, concurrent 1-min *GOES-9* and NOAA airborne radar observations. Preprints, *22nd Conf. on Hurricanes and Tropical Meteorology*, Fort Collins, CO, Amer. Meteor. Soc., 201-202.

Hawkins, H. F., and S. M. Imbembo, 1976: The structure of a small, intense hurricane - Inez, 1966. *Mon. Wea. Rev.*, 104, 418-442.

Helfrich, K. R., 1994: Thermals with background rotation and stratification. *J. Fluid Mech.*, 259, 265-280.

Heymsfield, G. M., J. B. Halverson, J. Simpson, L. Tian, and T. P. Bui, 2001: ER-2 Doppler radar investigations of the eyewall of Hurricane Bonnie during the Convection and Moisture Experiment-3. *J. Appl. Meteor.*, 40, 1310-1330.

Hock, T. F., and J. L. Franklin, 1999: The NCAR GPS dropwindsonde. *Bull. Amer. Meteor. Soc.*, 80, 407-420.

Holliday, C. R., and A. H. Thompson, 1979: Climatological characteristics of rapidly intensifying typhoons. *Mon. Wea. Rev.*, 107, 1022-1034.

Holton, J. R., 1992: *An Introduction to Dynamic Meteorology*, Academic Press, 511 pp.

Igau, R. C., M. A. LeMone, and D. Wei, 1999: Updraft and downdraft cores in TOGA COARE: Why so many buoyant downdraft cores? *J. Atmos. Sci.*, 56, 2232-2245.

Jenkins, G. M., and D. G. Watts, 1968: *Spectral Analysis and its Applications.* Holden-Day, 525 pp.

Jones, S. C., 1995: The evolution of vortices in vertical shear. Part II: Initially barotropic vortices. *Quart. J. Roy. Meteor. Soc.*, 121, 821-851.

Jorgensen, D. P., 1984a: Mesoscale and convective-scale characteristics of mature hurricanes. Part I: General observations by aircraft. *J. Atmos. Sci.*, 41, 1268-1285.

Jorgensen, D. P., 1984b: Mesoscale and convective-scale characteristics of mature hurricanes. Part II: Inner core structure of Hurricane Allen (1980). *J. Atmos. Sci.*, 41, 1287-1311.

Jorgensen, D. P., and M. A. LeMone, 1989: Vertical velocity characteristics of oceanic convection. *J. Atmos. Sci.*, 46, 621-640.

Jorgensen, D. P., E. J. Zipser, and M. A. LeMone, 1985: Vertical motions in intense hurricanes. *J. Atmos. Sci.*, 42, 839-856.

Kossin, J. P., and M. D. Eastin, 2001: Two distinct regimes in the kinematic and thermodynamic structure of the hurricane eye and eyewall. *J. Atmos. Sci.*, 58, 1079-1090.

Kossin, J. P., and W. H. Schubert, 2001: Mesovortices, polygonal flow patterns, and rapid pressure falls in hurricane-like vortices. *J. Atmos. Sci.*, 58, 2196-2209.

Kossin, J. P., B. D. McNoldy, and W. H. Schubert, 2002: Vortical swirls in hurricane eye clouds. *Mon. Wea. Rev.*, 130, 3144-3149.

Kraft, R. H., 1961: The hurricane's central pressure and highest wind. *Mar. Wea. Log*, 5, 155.

Lawrence, M. B., 1999: Eastern North Pacific hurricane season of 1997. *Mon. Wea. Rev.*, 127, 2440-2454.

Lawson, R. P., and W. A. Cooper, 1990: Performance of some airborne thermometers in clouds. *J. Atmos. Oceanic Technol.*, 7, 480-494.

LeeJoice, R. N., 2000: Hurricane inner core structure as revealed by GPS dropwindsondes. M. S. thesis, Dept. of Atmospheric Science, Colorado State University, 56 pp. [Available from Dept. Atmospheric Science, Colorado State University, Fort Collins, CO 80523.]

LeMone, M. A., 1980: On the difficulty of measuring temperature and humidity in clouds: Comments on "Shallow convection on Day 261 of GATE: Mesoscale arcs." *Mon. Wea. Rev.*, 108, 1702-1707.

LeMone, M. A., T. Y. Chang, and C. Lucas, 1994: On the effects of filtering on convective-core statistics. *J. Atmos. Sci.*, 51, 3344-3350.

LeMone, M. A., and E. J. Zipser, 1980: Cumulonimbus vertical velocity events in GATE. Part I: Diameter, intensity, and mass flux. *J. Atmos. Sci.*, 37, 2444-2457.

Lenschow, D. H., and W. T. Pennell, 1974: On the measurement of in-cloud and wet-bulb temperatures from an aircraft. *Mon. Wea. Rev.*, 102, 447-454.

Lindzen, R. S., A. Y. Hou, 1988: Hadley circulations for zonally averaged heating centered off the equator. *J. Atmos. Sci.*, 45, 2416-2427.

Liu, Y., D.-L. Zhang, and M. K. Yau, 1997: A multiscale numerical study of Hurricane Andrew (1992). Part I: An explicit simulation. *Mon. Wea. Rev.*, 125, 2597-2616.

Liu, Y., D.-L. Zhang, and M. K. Yau, 1999: A multiscale numerical study of Hurricane Andrew (1992). Part II: Kinematics and inner core structure. *Mon. Wea. Rev.*, 127, 2597-2616.

Lopez, R. E., 1977: The lognormal distribution of cumulus cloud properties. *Mon. Wea. Rev.*, 105, 865-872.

Lord, S. J., H. E. Willoughby, and J. M. Piotrowicz, 1984: Role of parameterized ice-phase microphysics in an axisymmetric non-hydrostatic tropical cyclone model. *J. Atmos. Sci.*, 41, 2836-2848.

Lucas, C., E. J. Zipser, and M. A. LeMone, 1994: Vertical velocity in oceanic convection off tropical Australia. *J. Atmos. Sci.*, 51, 3183-3193.

Malkus, J. S., 1958: On the the structure and maintenance of the mature hurricane eye. *J. Meteor.*, 15, 337-349.

Malkus, J., and H. Riehl, 1960: On the dynamics and energy transformations in steady-state hurricanes. *Tellus*, 12, 1-20.

Malkus, J., C. Ronne, and M. Chaffee, 1961: Cloud patterns in Hurricane Daisy, 1958. *Tellus*, 13, 8-30.

Mapes, B. E., 1993: Gregarious tropical convection. *J. Atmos. Sci.*, 50, 2026-2037.

Marks, F. D., Jr., and R. A. Houze Jr., 1987: Inner core structure of Hurricane Alicia from airborne Doppler radar observations. *J. Atmos. Sci.*, 44, 1296-1317.

Marks, F. D., Jr., R. A. Houze, Jr., and J. F. Gamache, 1992: Dual-aircraft investigation of the inner core of Hurricane Norbert (1984). Part I: Kinematic structure. *J. Atmos. Sci.*, 49, 919-942.

Masuda, K., 1988: Meridional heat transport by the atmosphere and ocean: Analysis of the FGGE data. *Tellus.*, 40A, 285-302.

Merceret, F. J., and T. L. Schricker, 1975: A new hot-wire liquid cloud water meter. *J. Appl. Meteor.*, 14, 319-326.

Montgomery, M. T., and J. Enagonio, 1998: Tropical cyclogenesis via convectively forced vortex Rossby waves in a three-dimensional quasigeostrophic model. *J. Atmos. Sci.*, 55, 3176-3207.

Montgomery, M. T., and J. L. Franklin, 1998: An assessment of the balance approximation in hurricanes. *J. Atmos. Sci.*, 55, 2193-2200.

Montgomery, M. T., and R. J. Kallenbach, 1997: A theory for vortex Rossby waves and its application to spiral bands and intensity changes in hurricanes. *Quart. J. Roy. Meteor. Soc.*, 123, 435-465.

Montgomery, M. T., V. A. Vladimirov, and P. V. Denissenko, 2002: An experimental study on hurricane mesovortices. *J. Fluid. Mech.*, 471, 1-32.

Neumann, C. J., B. J. Jarvinen, C. J. McAdie, and G. R. Hammer, 1999: Tropical Cyclones of the North Atlantic Ocean, 1871-1998. National Climatic Data Center in Cooperation with the National Hurricane Center, 206 pp.

Neumann, C. J., M. B. Lawrence, and E. L. Caso, 1977: Monte Carlo significance testing as applied to statistical tropical cyclone prediction models. *J. Appl. Meteor.*, 16, 1165-1174.

Ooyama, K., 1969: Numerical simulation of the life cycle of tropical cyclones. *J. Atmos. Sci.*, 26, 3-39.

Ooyama, K. V., 1982: Conceptual evolution of the theory and modeling of the tropical cyclone. *J. Meteor. Soc. Japan*, **60**, 369-380.

Panofsky, H. A., and G. W. Brier, 1968: *Some Applications of Statistics to Meteorology.* The Pennsylvania State University Press, 224 pp.

Parrish, J. R., R. W. Burpee, F. D. Marks, and C. W. Landsea, 1984: Mesoscale and convective-scale characteristics of Hurricane Frederic during landfall. Preprints, *15th Conf. on Hurricanes and Tropical Meteorology*, Miami, FL, Amer. Meteor. Soc., 415-420.

Pasch, R. J., and L. A. Avila, 1999: Atlantic hurricane season of 1996. *Mon. Wea. Rev.*, 127, 581-610.

Pasch, R. J., L. A. Avila, and J. L. Guiney, 2001: Atlantic hurricane season of 1998. *Mon. Wea. Rev.*, 129, 3086-3123.

Peng, M. S., and R. T. Williams, 1990: Dynamics of vortex asymmetries and their influence on vortex motion on a $\beta$-plane. *J. Atmos. Sci.*, 47, 1987-2003.

Persing, J., and M. T. Montgomery, 2003: Hurricane superintensity. *J. Atmos. Sci.* (accepted).

Powell, M. D., 1990: Boundary layer structure and dynamics in outer hurricane rainbands. Part II. Downdraft modification and mixed layer recovery. *Mon. Wea. Rev.*, 118, 918-938.

Pruppacher, H. R., and J. D. Klett, 1997: *Microphysics of Clouds and Precipitation.* Kluwer Academic Publishers, 954 pp.

Reasor, P. D., M. T. Montgomery, F. D. Marks Jr., and J. F. Gamache, 2000: Low-wavenumber structure and evolution of the hurricane inner core observed by airborne dual-Doppler radar. *Mon. Wea. Rev.*, 128, 1653-1680.

Reynolds, R. W., and T. M. Smith, 1993: An improved real-time global sea surface temperature analysis. *J. Climate*, 6, 114-119.

Riehl, H., 1979: *Climate and weather in the tropics.* Academic Press, Inc., New York, 611 pp.

Riehl, H., and J. Malkus, 1961: Some aspects of Hurricane Daisy (1958). *Tellus*, 13, 181-213.

Rotunno, R., and K. A. Emanuel, 1987: An air-sea interaction theory for tropical cyclones. Part II: Evolutionary study using a nonhydrostatic numerical model. *J. Atmos. Sci.*, 44, 542-561.

Rotunno, R., and J. B. Klemp, 1982: The influence of the shear induced pressure gradient on thunderstorm motion. *Mon. Wea. Rev.*, 110, 136-151.

Roux, F., and N. Viltard, 1995: Structure and evolution of Hurricane Claudette on 7 September 1991 from airborne Doppler radar observations. Part I: Kinematics. *Mon. Wea. Rev.*, 123, 2611-2639.

Ryan, B. F., G. M. Barnes, and E. J. Zipser, 1992: A wide rainband in a developing tropical cyclone. *Mon. Wea. Rev.*, 120, 431-447.

Samsury, C. E., and E. J. Zipser, 1995: Secondary wind maxima in hurricanes: Airflow and relationship to rainbands. *Mon. Wea. Rev.*, 123, 3502-3517.

Schubert, W. H., M. T. Montgomery, R. K. Taft, T. A. Guinn, S. R. Fulton, J. P. Kossin, and J. P. Edwards, 1999: Polygonal eyewalls, asymmetric eyewall contraction and potential vorticity mixing in hurricanes. *J. Atmos. Sci.*, 56, 1197-1223.

Shapiro, L. J., 1983: The asymmetric boundary layer flow under a translating hurricane. *J. Atmos. Sci.*, 40, 1984-1998.

Shapiro, L. J., and M. T. Montgomery, 1993: A three-dimensional balance theory for rapidly rotating vortices. *J. Atmos. Sci.*, 50, 3322-3335.

Shapiro, L. J., and H. E. Willoughby, 1982: The response of balanced hurricanes to local sources of heat and momentum. *J. Atmos. Sci.*, 39, 378-394.

Shea, D. J., and W. M. Gray, 1973: The hurricane's inner core region: I. Symmetric and asymmetric structure. *J. Atmos. Sci.*, 30, 1544-1564.

Sheets, R. C., 1969: Some mean hurricane soundings. *J. Appl. Meteor.*, 8, 134-146.

Smith, R. K., M. T. Montgomery, and H. Zhu, 2003: Buoyancy and the baroclinicity vector in tropical cyclones. *J. Atmos. Sci.* (submitted).

Spyers-Duran, P. A., 1968: Comparative measurements of cloud liquid water using heated wire and cloud replicating devices. *J. Appl. Meteor.*, 7, 674-678.

Srivastava, R. C., 1987: A model of intense downdrafts driven by the melting and evaporation of precipitation. *J. Atmos. Sci.*, 44, 1752-1773.

Wallace, J. M., G.-H. Lim, and M. L. Blackmon, 1988: Relationships between cyclone tracks, anticyclone tracks, and baroclinic waveguides. *J. Atmos. Sci.*, 45, 439-462.

Wang, Y., 2002: Vortex Rossby waves in a numerically simulated tropical cyclone. Part I: Overall structure, potential vorticity, and kinetic energy budgets. *J. Atmos. Sci.*, 59, 1213-1238.

Weatherford, C. L., 1989: The structural evolution of typhoons. Atmos Sci. Paper No. 446. Dept. Atmospheric Science, Colorado State University, 198 pp. [Available from Dept. Atmospheric Science, Colorado State University, Fort Collins, CO 80523.]

Wei, D., A. M. Blyth, and D. J. Raymond, 1998: Buoyancy of convective clouds in TOGA COARE. *J. Atmos. Sci.*, 55, 3381-3391.

Wexler, H., 1947: Structure of hurricanes as determined by radar. *Ann. N. Y. Acad. Sci.* , 48, 821-844.

Williams, E., and N. Renno, 1993: An analysis of the conditional instability of the tropical atmosphere. *Mon. Wea. Rev.*, 121, 21-36.

Willoughby, H. E., 1979: Forced secondary circulations in hurricanes. *J. Geophys. Res.*, 84, 3173-3183.

Willoughby, H. E., 1990a: Temporal changes of the primary circulation in tropical cyclones. *J. Atmos. Sci.*, 47, 242-264.

Willoughby, H. E., 1990b: Gradient balance in tropical cyclones. *J. Atmos. Sci.*, 47, 265-274.

Willoughby, H. E., 1998: Tropical cyclone eye thermodynamics. *Mon. Wea. Rev.*, 126, 3053-3067.

Willoughby, H. E., and P. G. Black, 1996: Hurricane Andrew in Florida: Dynamics of a disaster. *Bull. Amer. Meteor. Soc.*, 77, 543-549.

Willoughby, H. E., and M. B. Chelmow, 1982: Objective determination of hurricane tracks from aircraft observations. *Mon. Wea. Rev.*, 110, 1298-1305.

Willoughby, H. E., J. A. Clos, and M. G. Shoreibah, 1982: Concentric eyewalls, secondary wind maxima, and the evolution of the hurricane vortex. *J. Atmos. Sci.*, 39, 395-411.

Willoughby, H. E., F. D. Marks Jr., and R. J. Feinberg, 1984: Stationary and moving convective bands in hurricanes. *J. Atmos. Sci.*, 41, 3189-3211.

Zhang, D.-L., Y. Liu, and M. K. Yau, 2000: A multiscale numerical study of Hurricane Andrew (1992). Part III: Dynamically induced vertical motion. *Mon. Wea. Rev.*, 128, 3772-3788.

Zipser, E. J., 1977: Mesoscale and convective-scale downdrafts as distinct components of squall-line circulation. *Mon. Wea. Rev.*, 105, 1568-1589.

Zipser, E. J., 2003: Some views on "hot towers after 50 years of tropical field work and two years of TRMM data. *Meteorological Monographs* (accepted).

Zipser, E. J., R. J. Meitin, and M. A. LeMone, 1981: Mesoscale motion fields associated with a slowly moving GATE convective band. *J. Atmos. Sci.*, 38, 1725-1750.

# Appendix A

## SUMMARY FIGURES FOR ALL CASES

Summary figures of inner-core vertical velocity and convective core buoyancy characteristics were presented in Chapter 4 for only 4 of the 25 cases (or flights) examined in this study. Presented here for completeness are similar summary figures for all cases. The figures are organized into three panels. In each panel, radial leg data were superimposed upon a single-scan horizontal reflectivity field from a representative eye penetration. The upper panel highlights portions of each radial leg in which the mesoscale vertical velocity ($w_m$) exceeded certain appreciable magnitudes ($> 3$ m s$^{-1}$, $> 1$ m s$^{-1}$, and $< -1$ m s$^{-1}$). The middle panel depicts the locations of all identified updraft cores stratified by their average convective vertical velocity ($\overline{w}_c$) and average total buoyancy ($\overline{B}$) characteristics. The stratification criteria ($\overline{w}_c > 2$ m s$^{-1}$ and $\overline{B} > 0.25$ K) were designed to isolate updraft cores with appreciable vertical motion or positive buoyancy. Within the context of the statistical distributions presented in Chapter 3, the criteria isolate cores from the upper ~33% of each distribution. The lower panel denotes the locations of downdraft cores with average total vertical velocity ($\overline{w}$) $< -1$ m s$^{-1}$ stratified by their $\overline{B}$ characteristics (either positive or negative). Downdraft cores with $\overline{w} > -1$ m s$^{-1}$ were excluded since they do not contribute significantly to downward mass transport (see Chapter 3.3 for further discussion of such cores). The storm motion and 200-850 mb vertical wind shear vectors (see Table 2.2) are also shown in each panel of the summary figures when available.

The summary figures (Figs. A.1-A.24) are utilized to depict *gross* azimuthal relationships between vertical velocity, buoyancy, and radar reflectivity. Core characteristics and

convective-scale features in the single-scan radar reflectivity field are not directly comparable since the radial leg data was collected over the course of several hours. However, the quasi-steadiness of the mesoscale convective structure during most inner-core observation periods should permit comparison of gross azimuthal relationships using these figures. The few cases in which low-wavenumber mesoscale reflectivity features exhibited considerable azimuthal propagation include Gilbert 880911I (eyewall), Gilbert 880914H (outer eyewall), Gilbert 880915I1 (outer eyewall), and Joan 881021I (eyewall). For these cases, azimuthal relationships between core characteristics and the radar reflectivity field should be viewed with caution.

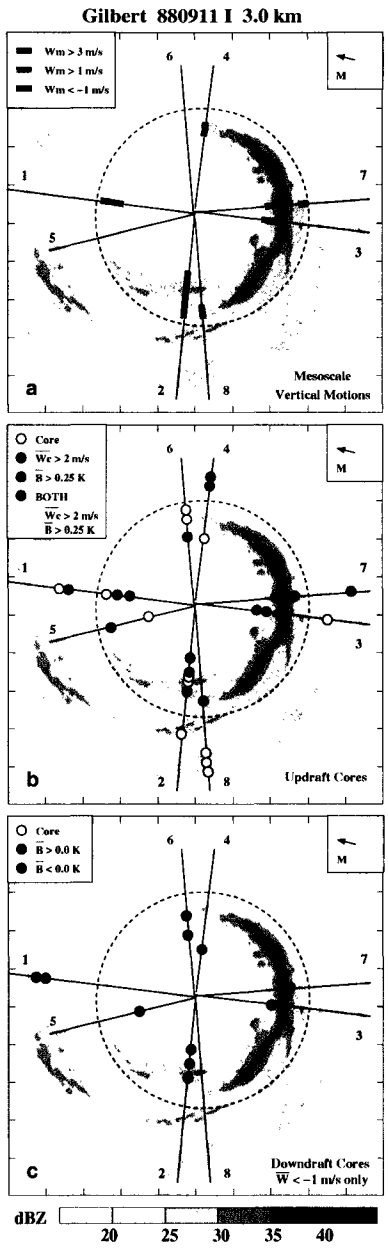


Figure A.1: Summary of flight-level vertical velocity and core buoyancy for Hurricane Gilbert between 1600 and 2100 UTC on 11 September 1988 at ~3.0 km altitude. (a) Sections of each radial leg in which the mesoscale vertical velocity $w_m$ exceeded certain magnitudes. (b) Locations of convective updraft cores stratified by their average convective vertical vertical velocity $\overline{w}_c$ and average total buoyancy $\overline{B}$ characteristics. (c) Locations of convective downdraft cores with average total vertical velocity $\overline{w} < -1$ m s$^{-1}$ stratified by their $\overline{B}$ characteristics. The radial leg data in each panel is superimposed upon a representative storm-relative radar reflectivity field observed at 1836 UTC during the third of four eye penetrations. The domain of each panel is 240 km × 240 km and tic marks are shown every 24 km. The storm motion (M, blue) and vertical wind shear (S, red) vectors are shown in the upper right corner. Dashed circles denote the approximate separation radius between the eyewall and rainband regions.

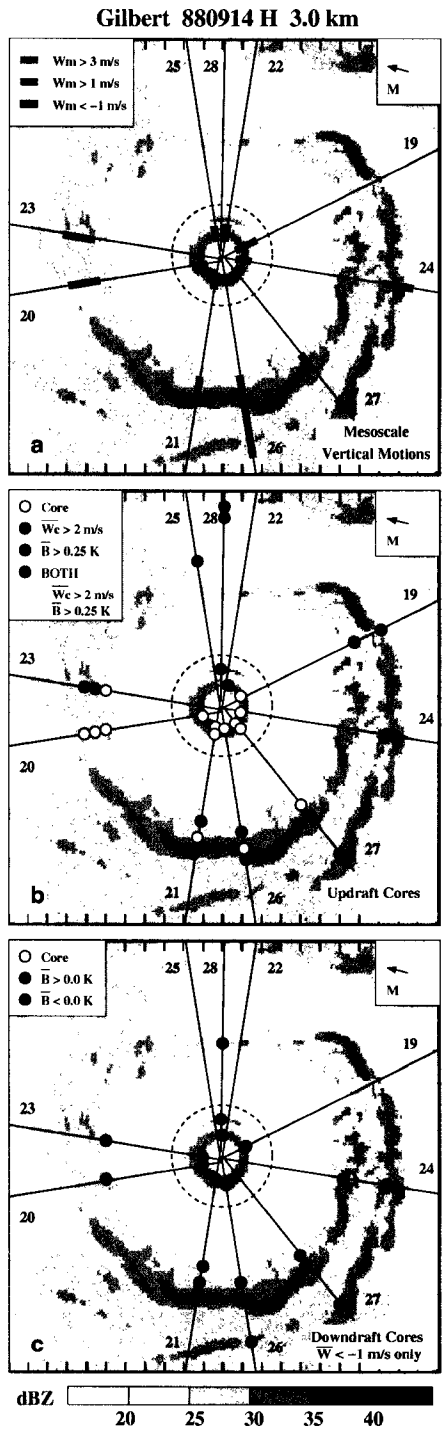


Figure A.2: As in Fig. A.1 but for Hurricane Gilbert between 0500 and 1200 UTC on 14 September 1988 at ~3.0 km altitude. The representative storm-relative radar reflectivity field was observed at 0910 UTC during the third of five eye penetrations.

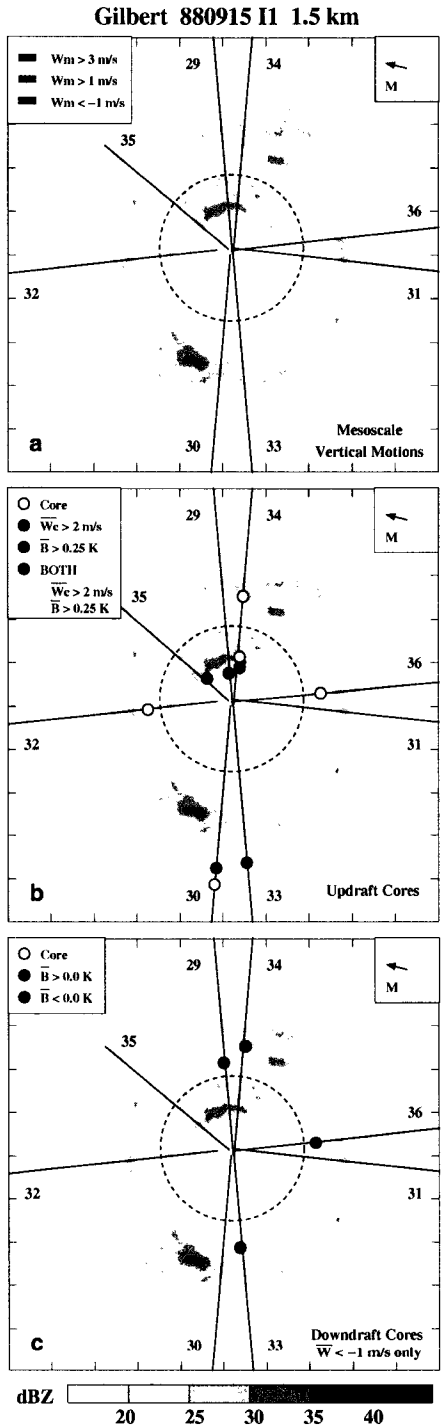


Figure A.3: As in Fig. A.1 but for Hurricane Gilbert between 1200 and 1700 UTC on 15 September 1988 at ~1.5 km altitude. The representative storm-relative radar reflectivity field was observed at 1607 UTC during the fourth of four eye penetrations.

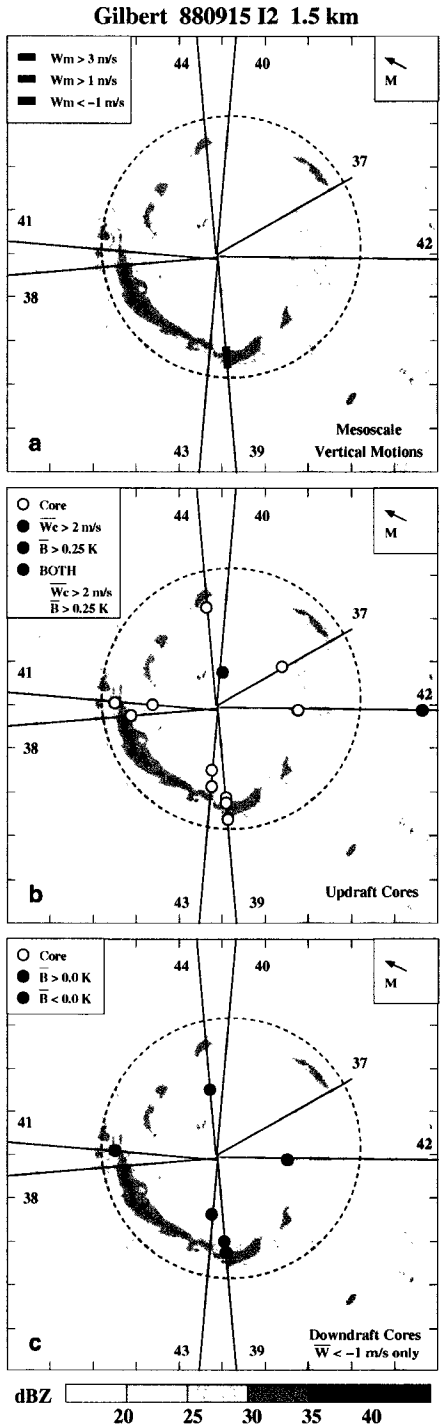


Figure A.4: As in Fig. A.1 but for Hurricane Gilbert between 0000 and 0600 UTC on 16 September 1988 at ~1.5 km altitude. The representative storm-relative radar reflectivity field was observed at 0156 UTC during the second of four eye penetrations.

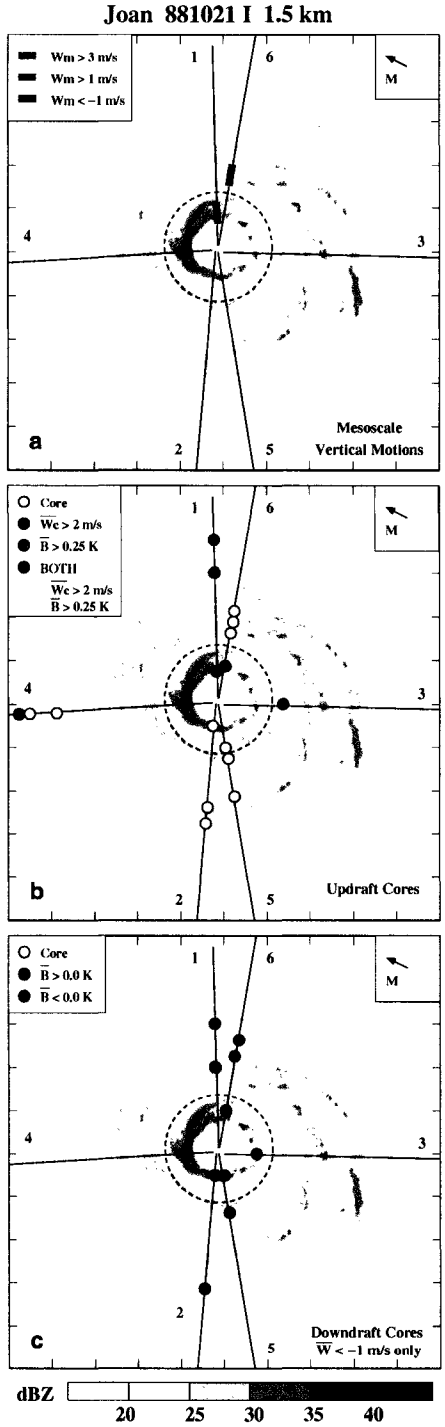


Figure A.5: As in Fig. A.1 but for Hurricane Joan between 1700 and 2000 UTC on 21 October 1988 at ~1.5 km altitude. The representative storm-relative radar reflectivity field was observed at 1724 UTC during the first of three eye penetrations.

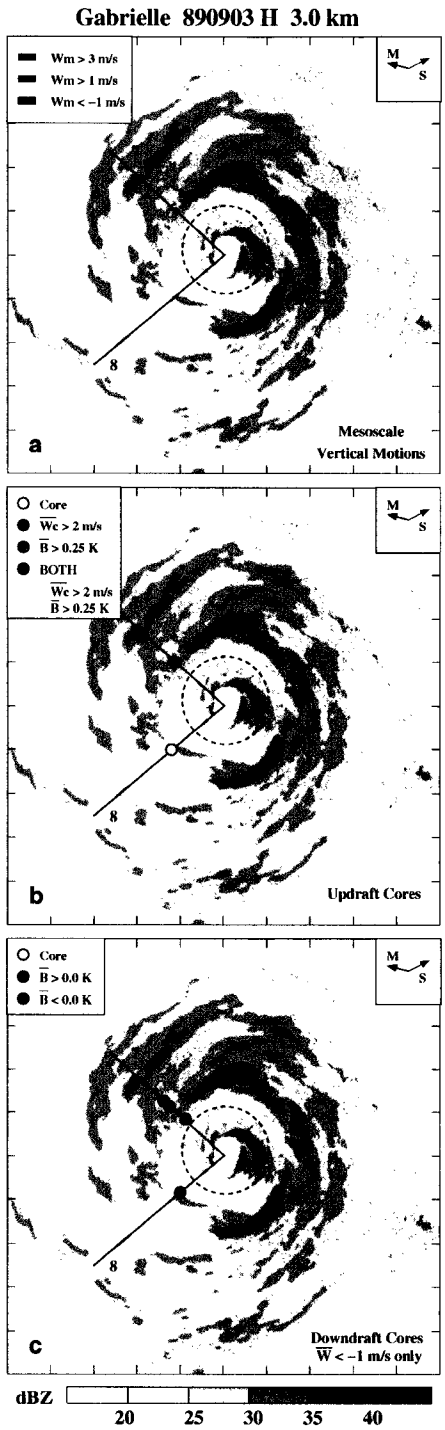


Figure A.6: As in Fig. A.1 but for Hurricane Gabrielle between 1800 and 2400 UTC on 3 September 1989 at ~3.0 km altitude. The representative storm-relative radar reflectivity field was observed at 2048 UTC during the fourth of six eye penetrations. Note that only rainband cores were analyzed because the eyewall convection was not adequately resolved once the 20 km Bartlett filter was applied to the flight-level data.

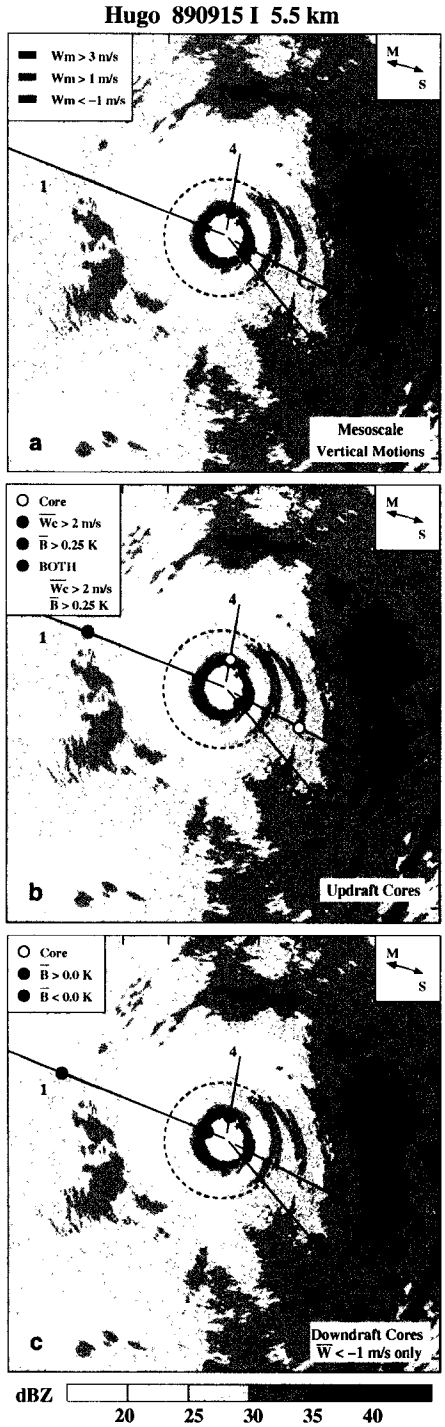


Figure A.7: As in Fig. A.1 but for Hurricane Hugo between 1700 and 1900 UTC on 15 September 1989 at ~5.5 km altitude. The representative storm-relative radar reflectivity field was observed at 1840 UTC during the second of two eye penetrations. Note that the elevated radar reflectivities in the rainband region are dominated by the brightband signature.

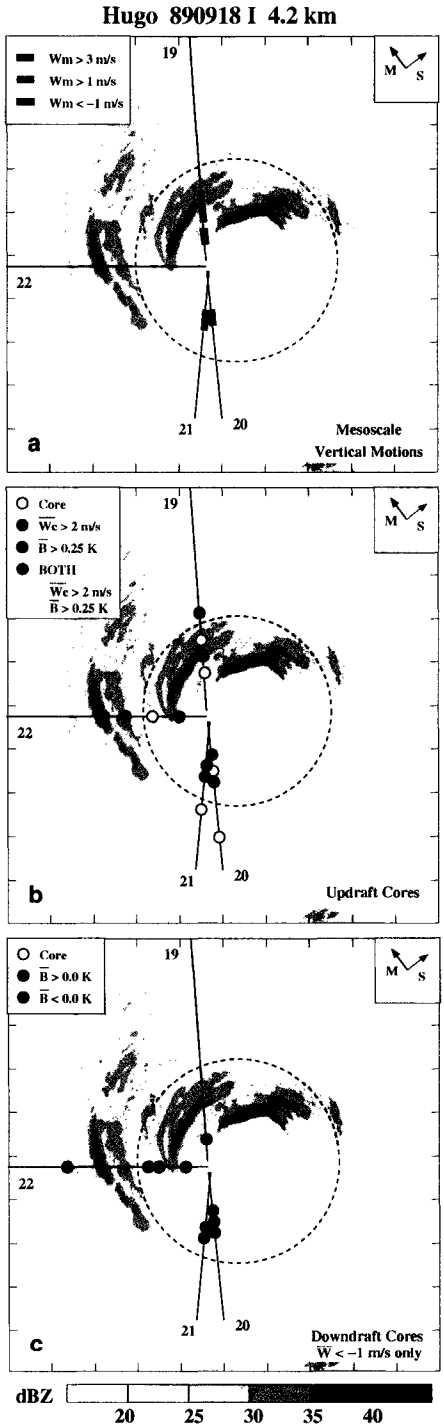


Figure A.8: As in Fig. A.1 but for Hurricane Hugo between 1900 and 2200 UTC on 18 September 1989 at ~4.2 km altitude. The representative storm-relative radar reflectivity field was observed at 2054 UTC during the second of three eye penetrations.

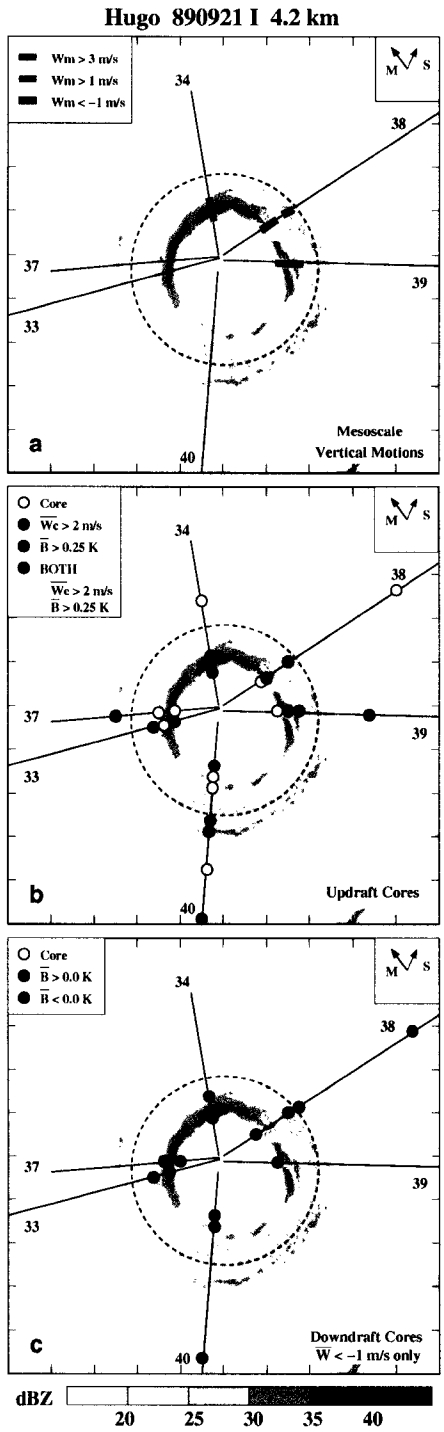


Figure A.9: As in Fig. A.1 but for Hurricane Hugo between 2300 UTC on 21 September and 0400 UTC on 22 September 1989 at ~4.2 km altitude. The representative storm-relative radar reflectivity field was observed at 0218 UTC during the third of four eye penetrations.

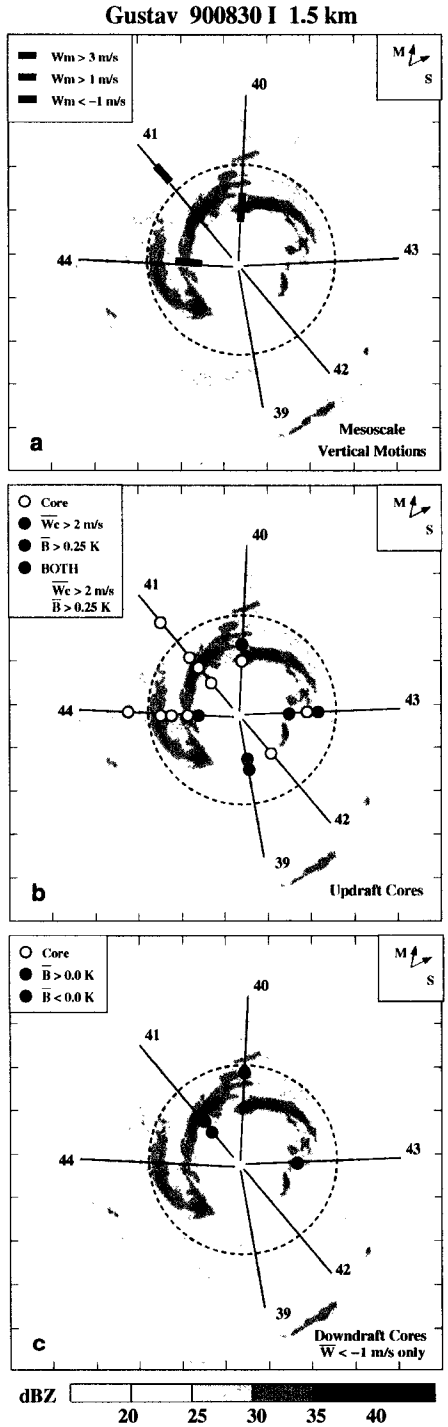


Figure A.10: As in Fig. A.1 but for Hurricane Gustav between 1900 and 2200 UTC on 30 August 1990 at ~1.5 km altitude. The representative storm-relative radar reflectivity field was observed at 2036 UTC during the second of three eye penetrations.

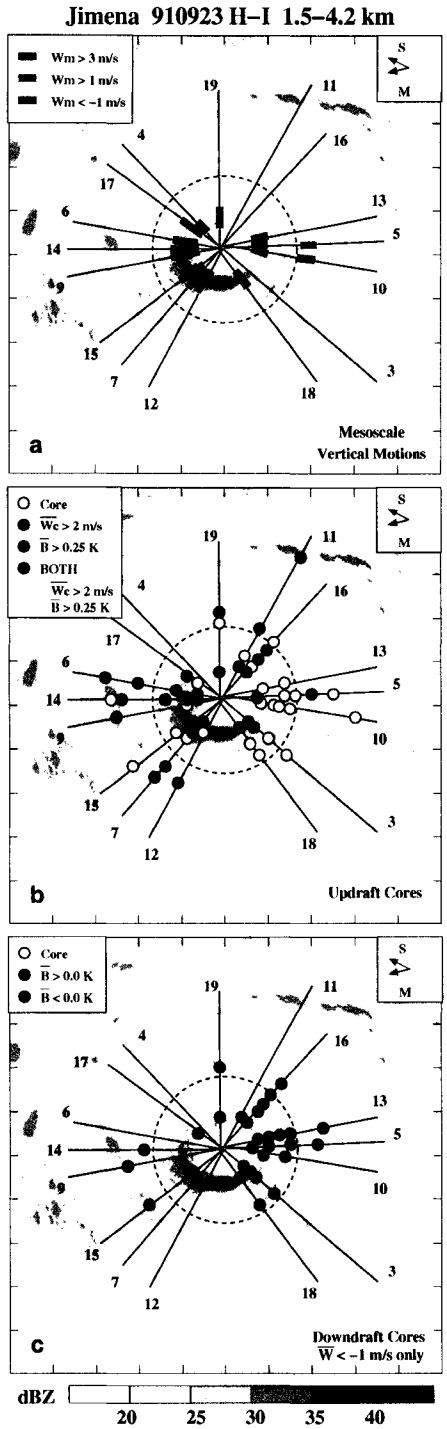


Figure A.11: As in Fig. A.1 but for Hurricane Jimena between 1900 UTC on 23 September and 0100 UTC on 24 September 1991 at ~3.0 km altitude. The representative storm-relative radar reflectivity field was observed at 2058 UTC during the second of seven eye penetrations at ~3.0 km altitude. Note that Legs 3 and 4 were flown at ~1.5 km altitude and Leg 19 was flown at ~4.2 km altitude.

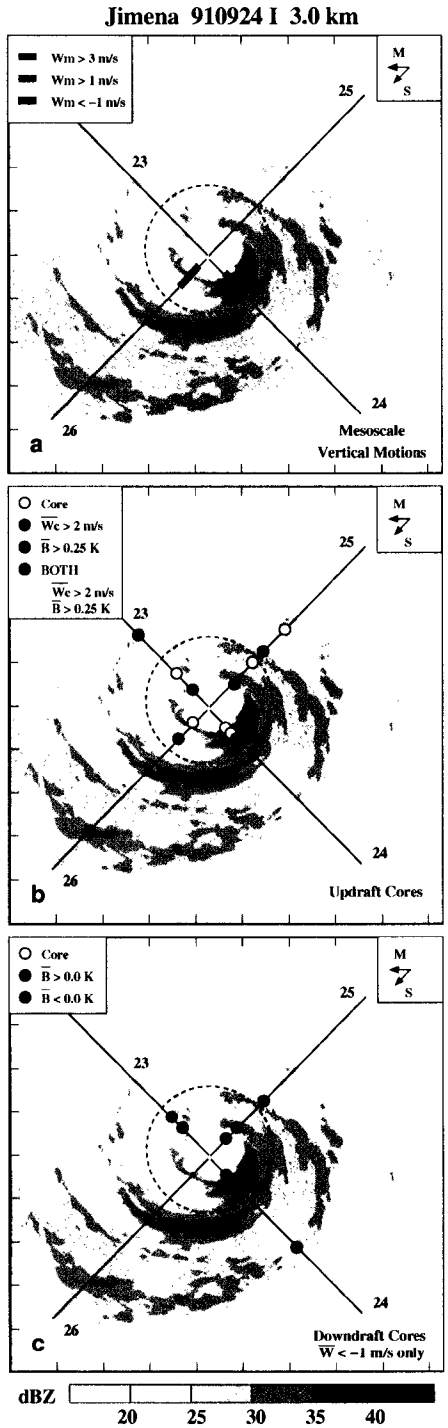


Figure A.12: As in Fig. A.1 but for Hurricane Jimena between 2100 and 2400 UTC on 24 September 1991 at ~3.0 km altitude. The representative storm-relative radar reflectivity field was observed at 2213 UTC during the first of two eye penetrations.

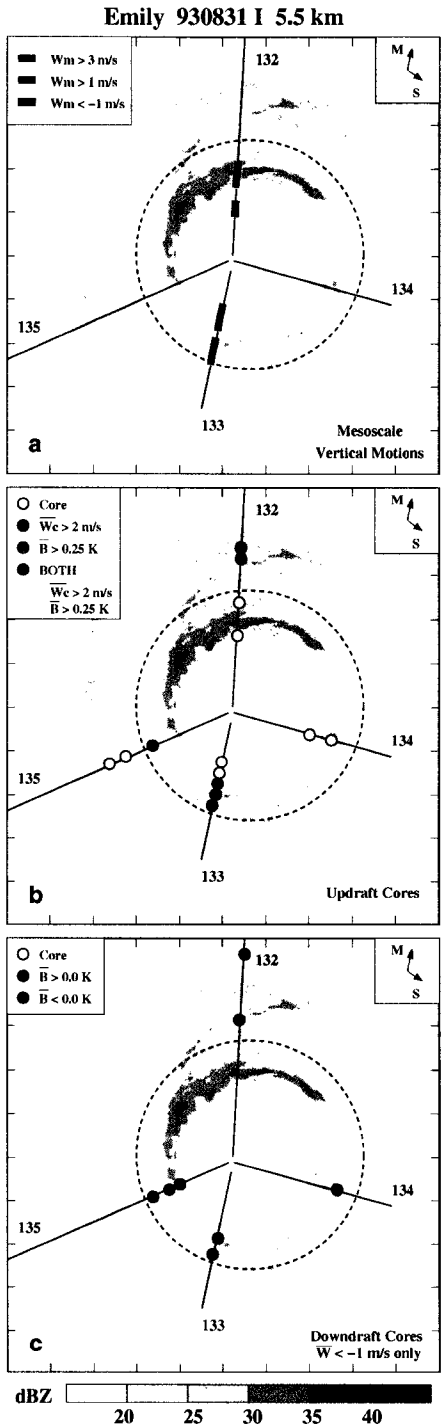


Figure A.13: As in Fig. A.1 but for Hurricane Emily between 2100 and 2300 UTC on 31 August 1993 at ~5.5 km altitude. The representative storm-relative radar reflectivity field was observed at 2224 UTC during the second of two eye penetrations.

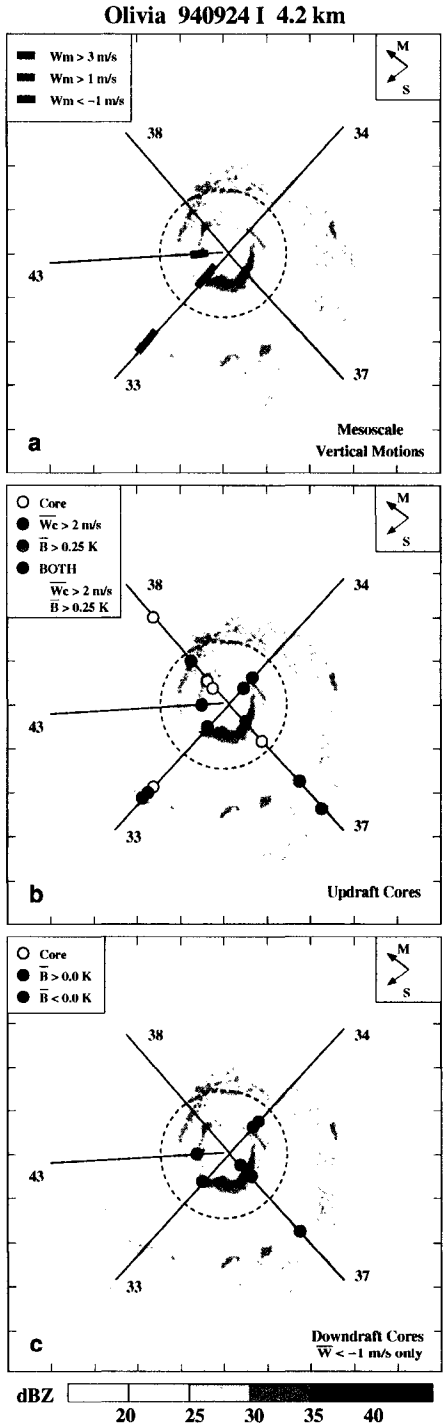


Figure A.14: As in Fig. A.1 but for Hurricane Olivia between 1900 and 2400 UTC on 24 September 1994 at ~4.2 km altitude. The representative storm-relative radar reflectivity field was observed at 2020 UTC during the second of seven eye penetrations.

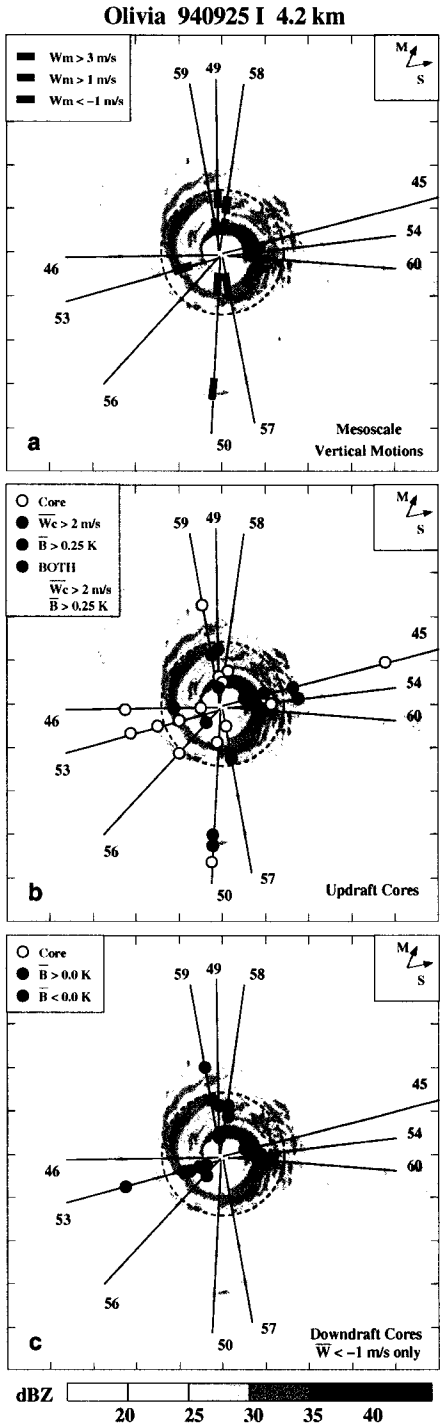


Figure A.15: As in Fig. A.1 but for Hurricane Olivia between 2000 UTC on 25 September and 0100 UTC on 26 September 1994 at ~4.2 km altitude. The representative storm-relative radar reflectivity field was observed at 2138 UTC during the third of eight eye penetrations.

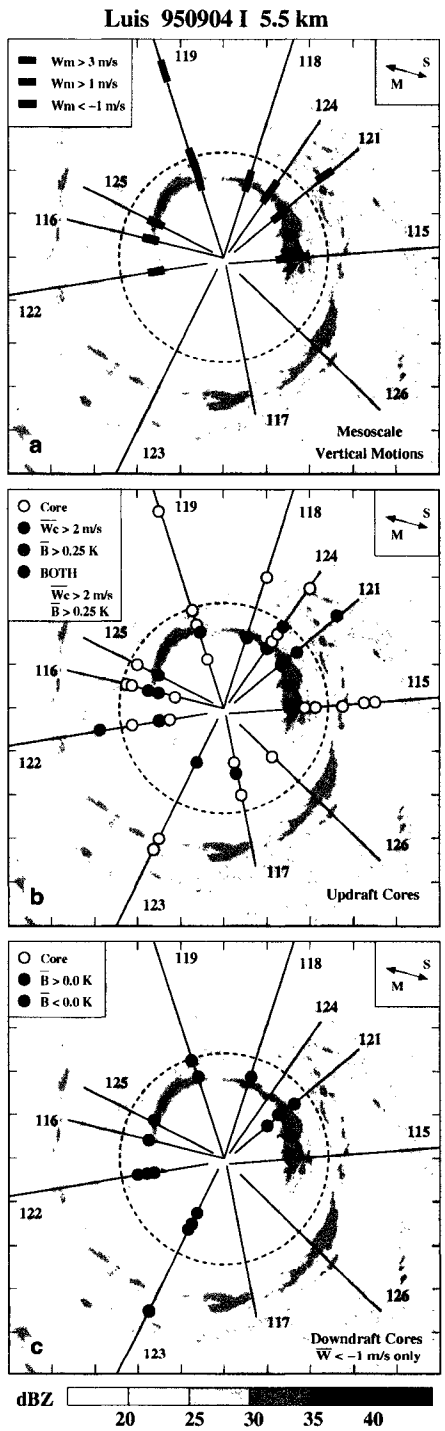


Figure A.16: As in Fig. A.1 but for Hurricane Luis between 2200 UTC on 4 September and 0400 UTC on 5 September 1995 at ~5.5 km altitude. The representative storm-relative radar reflectivity field was observed at 2312 UTC during the second of six eye penetrations.

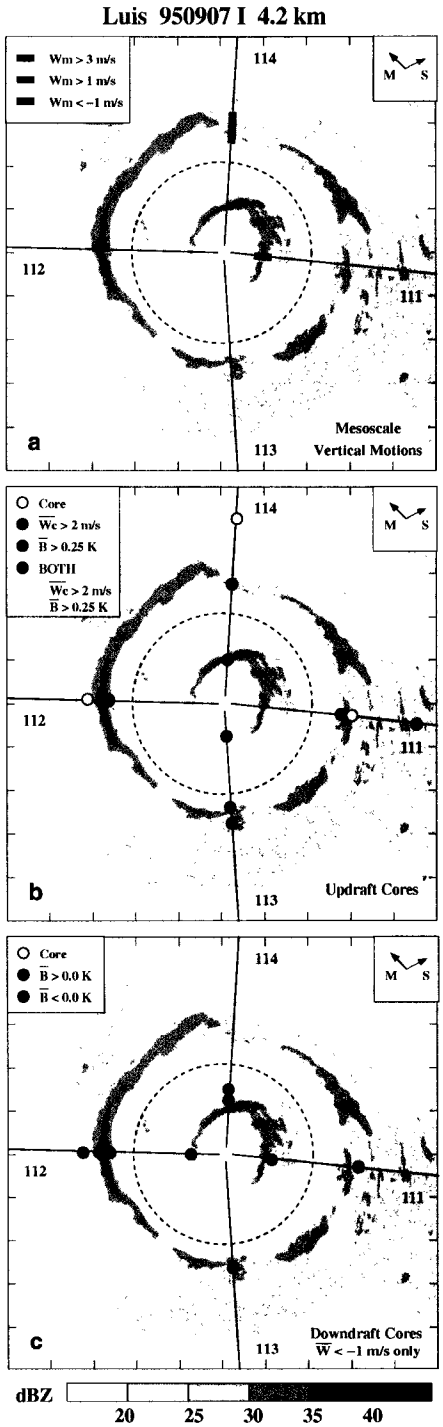


Figure A.17: As in Fig. A.1 but for Hurricane Luis between 1600 and 2000 UTC on 7 September 1995 at ~4.2 km altitude. The representative storm-relative radar reflectivity field was observed at 1915 UTC during the second of two eye penetrations.

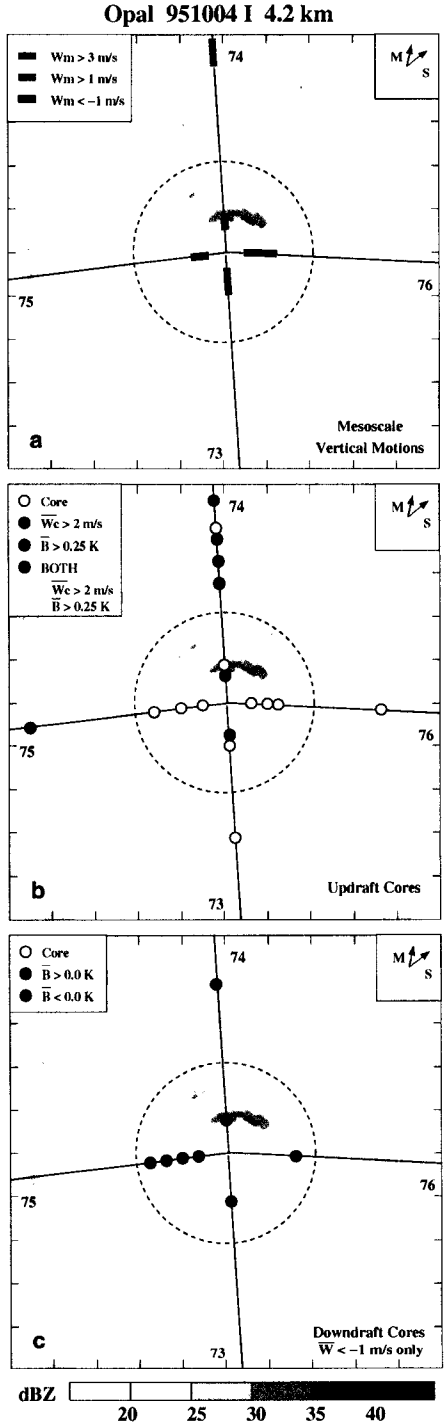


Figure A.18: As in Fig. A.1 but for Hurricane Opal between 1600 and 1900 UTC on 4 October 1995 at ~4.2 km altitude. The representative storm-relative radar reflectivity field was observed at 1811 UTC during the second of two eye penetrations.

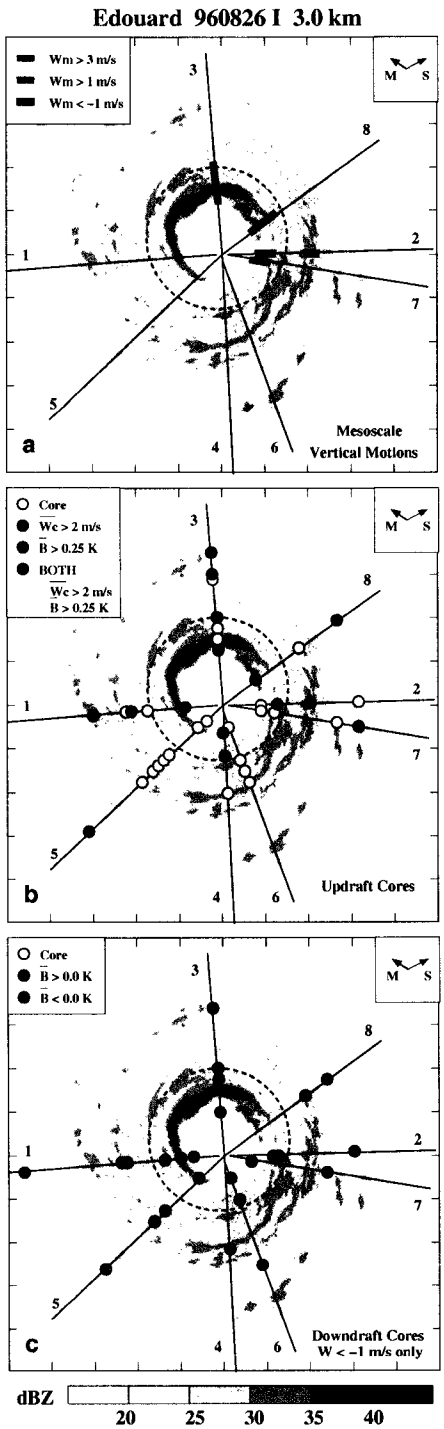


Figure A.19: As in Fig. A.1 but for Hurricane Edouard between 1800 and 2200 UTC on 26 August 1996 at ~3.0 km altitude. The representative storm-relative radar reflectivity field was observed at 2144 UTC during the fourth of four eye penetrations.

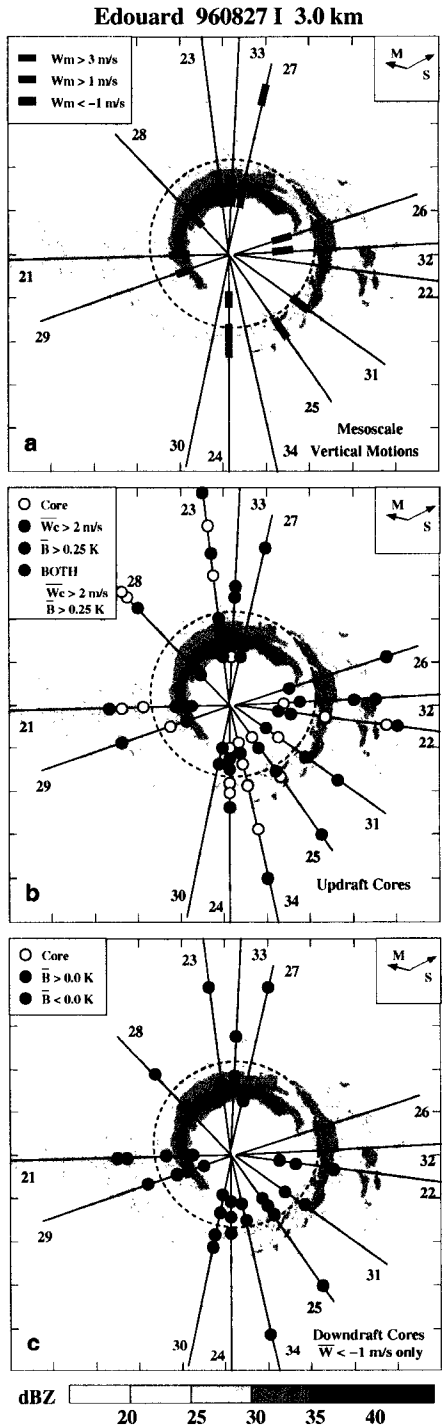


Figure A.20: As in Fig. A.1 but for Hurricane Edouard between 1800 and 2400 UTC on 27 August 1996 at ~3.0 km altitude. The representative storm-relative radar reflectivity field was observed at 2307 UTC during the seventh of seven eye penetrations.

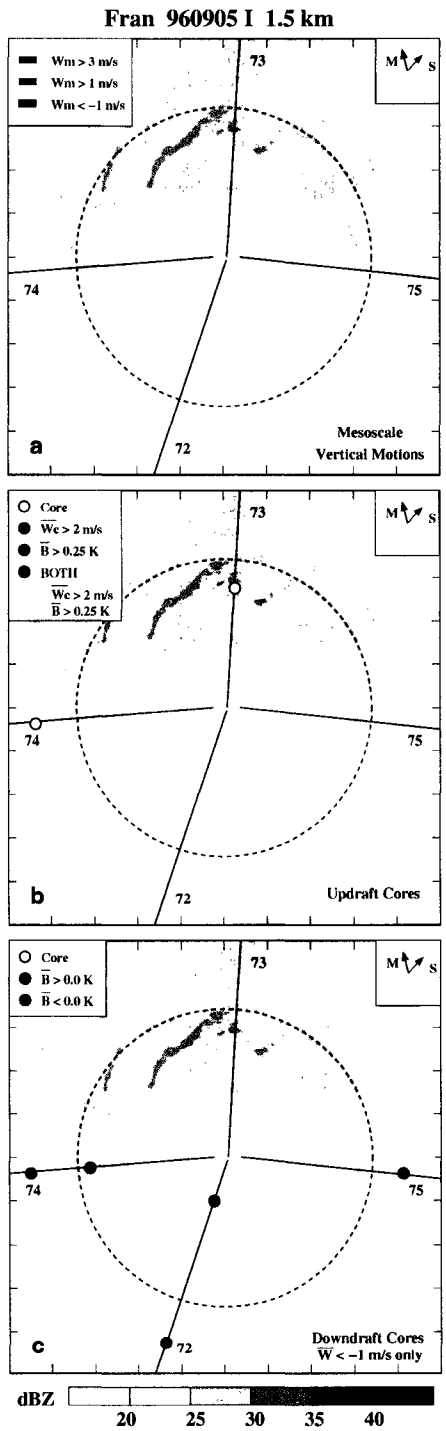


Figure A.21: As in Fig. A.1 but for Hurricane Fran between 1800 and 2400 UTC on 5 September 1996 at ~1.5 km altitude. The representative storm-relative radar reflectivity field was observed at 2240 UTC during the third of four eye penetrations.

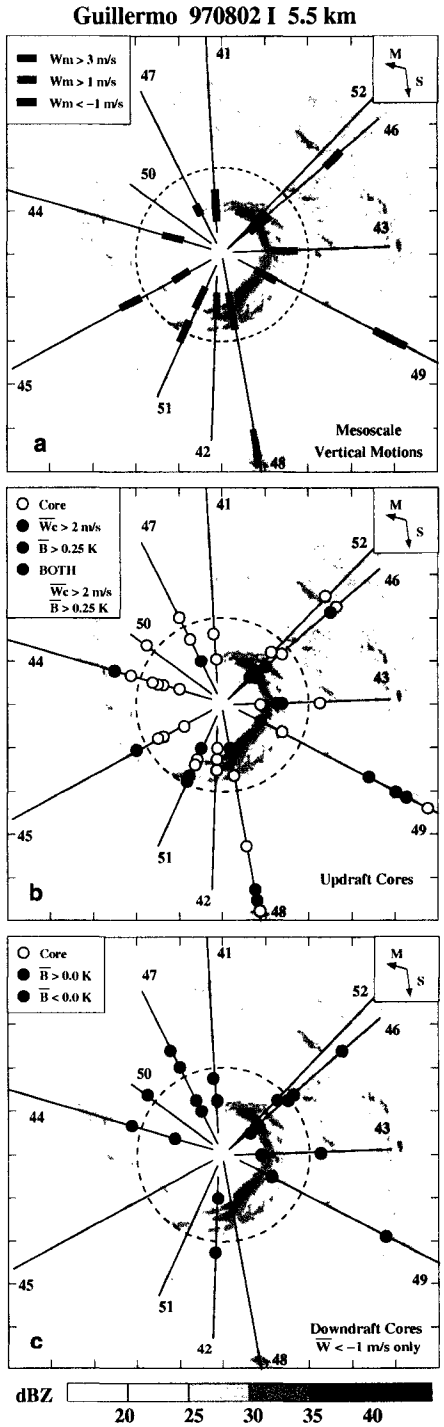


Figure A.22: As in Fig. A.1 but for Hurricane Guillermo between 1800 UTC on 2 August and 0100 UTC on 3 August 1997 at ~5.5 km altitude. The representative storm-relative radar reflectivity field was observed at 0910 UTC during the fifth of six eye penetrations.

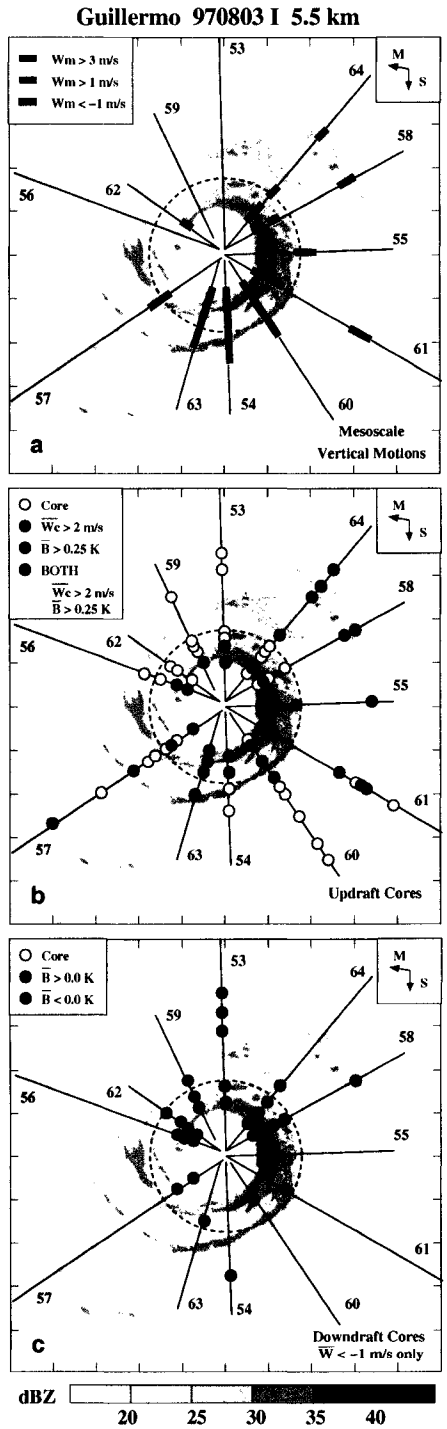


Figure A.23: As in Fig. A.1 but for Hurricane Guillermo between 1900 UTC on 3 August and 0100 UTC on 4 August 1997 at ~5.5 km altitude. The representative storm-relative radar reflectivity field was observed at 2204 UTC during the fourth of six eye penetrations.

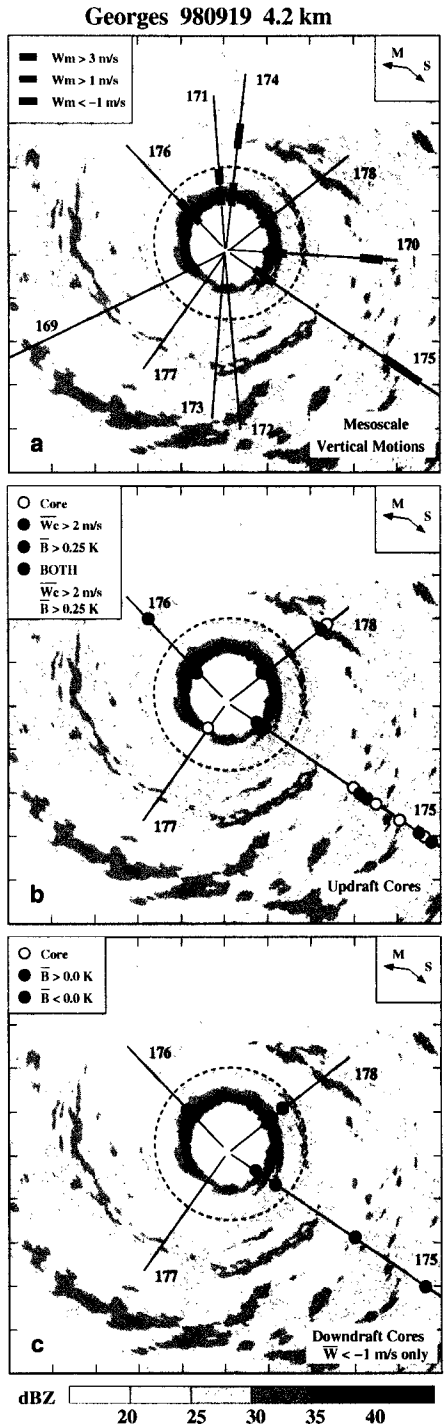


Figure A.24: As in Fig. A.1 but for Hurricane Georges between 1900 UTC on 19 September and 0100 UTC on 20 September 1998 at ~4.2 km altitude. The representative storm-relative radar reflectivity field was observed at 1955 UTC during the second eye penetration by the first aircraft. Note that core buoyancy characteristics could only be determined along the four radial legs flown by the second aircraft between 2300 and 0100 UTC.